2015

Effect of particles on evaporation of droplet containing particles

Yan Wei
University of Central Florida

EFFECT OF PARTICLES ON EVAPORATION OF DROPLET CONTAINING PARTICLES

by

YAN WEI
B.S. Wuhan University, Wuhan, China 2007
M.S. University of Central Florida, 2013

A dissertation submitted in partial fulfillment of the requirements
for the degree of Doctor of Philosophy
in the Department of Mechanical and Aerospace Engineering
in the College of Engineering and Computer Science
at the University of Central Florida
Orlando, Florida

Summer Term
2015

Major Professors: Ruey-Hung Chen, Weiwei Deng

ABSTRACT

The evaporation of droplet containing insoluble particles has grown into an active area of research due to the needs for nanofluids for applications in heat transfer, combustion, and manufacturing desired micro/nano particles in the pharmaceutical industry. The evaporation of droplets containing particles involves complicated multiphase heat and mass transport. The evaporation process consists of two stages: the first stage consists of evaporation until a shell of particle forms or when the solid to liquid ratio is sufficiently large and the second stage, where the droplet size is commonly assumed to be unchanged. The dissertation investigates the evaporation kinetics in the first stage.

An experimental setup based on electrodynamic balance (EDB) is built to allow the observation of evaporation of a free standing micro size droplet. Besides experimental design, a novel theoretical model is developed to first describe the morphological evolution process in the absence of internal convection. The model accounts for the effect of particles at the droplet surface on the diffusion of liquid vapor. The gradually increasing particle number at the droplet surface reduces the area for evaporation, leading to reduction in evaporation rate in the first drying stage, contrary to previous assumptions. The evaporation in the first stage is controlled by *Pe* (defined as the ratio of droplet evaporation rate to the particle diffusion rate) and particle properties such as wettability. For large values of *Pe*, the particles concentration is high near the droplet surface, leading to the change of evaporation rate. For small values of *Pe*, the effect of particles on the evaporation rate of droplet in the

first drying stage is small because particles are allowed sufficient time to redistribute within the droplet.

The model analysis also reveals that particle wettability is an important factor affecting the first drying stage. For hydrophilic particles, the contact angle of the particles at the droplet surface is small, leading to small change of evaporation in the first stage. For the hydrophobic particles that have large contact angles, the change of evaporation rate in the first drying stage is larger.

The evaporation model that accounts for the internal convection is also used to describe the evaporation process. In this model, the evaporation behavior during the first stage is controlled by the particle mobility, initial particle concentration, and droplet recession/evaporation rate. For particles with high mobility, the particle distribution within the droplet tends to be smooth. The effect of convection flow on the particles distribution becomes stronger as particle mobility decreases. Once the particles mobility is decreased to a limit at which the surface particle density is only controlled by the internal flow and the evaporation process is independent of the particles mobility. For a given internal flow field and a specific particles mobility, the duration of the first stage and the final dry particle size are both controlled by the initial particle concentration. A smaller/larger initial particle concentration results in a longer/shorter first stage and smaller/larger dry particle.

To my family Weiwei and Kevin

ACKNOWLEDGMENTS

First of all I want to thank my advisors Dr. Ruey-Hung Chen and Dr. Weiwei Deng, whose guidance is priceless for me. I learned from them not only specific skills, but also principles in research. For example, one thing I learned from them is that we must have “good taste”, which means we should set a high standard for our research. Another example is that we should be persistent and find ways to finish tasks we initiated, no matter how challenging they are. These skills and principles will continue to influence me in the future.

Second I want to thank my parents, who gave their best to raise me up and provided me a good environment. No matter what decisions I made, they always gave me their unconditional support. I felt really lucky to have them as my parents and I wished I could have visited them more often.

Third I want to thank Professor Shawn Putnam and Professor Thomas Wu for serving the committee. I also want to thank all my lab mates for their help to make this dissertation possible.

Last but not least, I want to thank Weiwei Yang, who is my loving husband, my best friend, my inspiring colleague, and the father of our baby Kevin. Weiwei and Kevin are true blessings in my life.

TABLE OF CONTENTS

LIST OF FIGURES

LIST OF TABLES

CHAPTER 1. INTRODUCTION

Over the past 20 years, the study of the evaporation of droplet containing particles has grown into an active area of research due to the needs for applying nanofluids into heat transfer and combustion engines and manufacturing desired micro/nano particles in the pharmaceutical industry. The aim of this dissertation is to build an experimental setup to allow the study of evaporation of a single free standing micrometer droplet and develop a theoretical model to predict the effect of particles on the evaporation behavior in the first stage.

In this chapter, we first review the application of nanofluids in heat transfer equipment, combustion engines, and particle manufacturing. Then, we review the experimental and theoretical studies on evaporation of droplets containing particles. Finally, we provide an overview of this dissertation.

1.1 Emerging applications of nanofluids

Nanofluids have been gaining growing interest in the past decade, due to its great important applications in nanotechnology and thermal engineering. Nanofluids are engineered by dispersing nanoparticles in liquid. The average size of the nano particles is below 100 nm. (Das et al., 2008). In the past 10 years, the number of the publications in this emerging filed has been exponentially increased. (Castro et al., 2012).

1.1.1 Enhancement of heat transfer

The study of enhancing conductivity of the fluid has been focused on adding metallic particles in the traditional heat transfer fluid. Maxwell (Maxwell, 1891) first theoretically studied the effective thermal conductivity of the liquid suspension. Since then, numerous publications on the theoretical and experimental studies of improving the thermal conductivities came out. However, all the studies focused on suspensions with particle size between micrometers to millimeters. The liquid suspension with micrometer or millimeter size particles has two major disadvantages: (1) the large particles settle rapidly in fluids, (2) the particle concentration in the liquid suspensions is limited at low level. Compared to liquid suspensions with millimeter or micrometer sized particles, nanofluids are much more stable. The conduction is enhanced in liquid suspension with nanoparticles due to larger surface to volume ratio. Furthermore, erosion and clogging can be dramatically reduced due to smaller particle size. Eastman et al. (Eastman et al., 2001) studied the effective thermal conductivity of ethylene glycol by adding 0.3 vol% of Cu nanoparticle coated with thioglycolic acid and observed 40% increase compared with pure ethylene glycol.

In industry cooling is usually performed in convection conditions. Experimentalists have shown that nanofluids also show that the effective heat transfer coefficient is larger than that of base fluids (Faulkner et al., 2004, Wen and Ding, 2004, Ding et al., 2006, Xuan et al., 2000).

1.1.2 Enhancement of heat of combustion

Because of their high energy density, the combustion of metals has always been of interest to the combustion community. In propellant and explosives, metallic particles are usually

added in the fuel liquid serving as energetic additives. (Gan et al., 2011). Beckstead et al. (2004) and Yetter and Dryer (2001) gave a review on the ignition of micro sized aluminum particles. Huang et al. (2001) compared the burning time of aluminum particles at various sizes. They observed that there is a slope change when particle size is around 10 μm, indicating the possible transition from a diffusion controlled combustion process to a kinetic controlled combustion process. Bazyn et al. (2007) proved the existence of this transition in oxygen mixture at particle size around 10 μm from shock tube measurements. Bazyn's study (2007) also showed that combustion temperatures of nanoparticles were below the aluminum boiling temperature.

Experimental studies showed that the ignition and combustion of nanoparticles were more difficult to distinguish (Huang et al., 2009). For larger particles (>100 μm), the ignition was achieved near the melting point of the particles oxide (Aluminum oxide, 2350 K). While for aluminum particles with diameter between 1 – 100 μm, the ignition can be achieved from 1300 to 2300 K. For the nanoparticles, it is reported that the ignition temperature can reach as low as 900 K (Bulian et al., 2004), which is below the melting point of aluminum.

By adding energetic nanoparticles in the fossil fuel, the combustion efficiency and the stability will be increased. Macek (1972) showed 10-25% increase of combustion efficiency by adding 0.5% of aluminum nanoparticles in the fuel. Selvan et al., (1009) observed that the cerium oxide nanoparticles serving as catalyst, which improves the combustion efficiency and reduces the pollutions. Gan et al. (2011) studied the effect of nano aluminum particles on the burning characteristics of ethanol and observe a complete burning of the fuel.

1.1.3 Applications in functioning of micro/nano particles

"Controlled drug delivery is the engineering of physical, chemical and biological components into a system for delivering controlled amounts of a therapeutic agent to a patient over a prolonged period" (Saltzman et al., 2001). To achieve the goal, controlled drug delivery systems is developed which consist of macromolecular carriers that transport the therapeutic agent throughout the body to the desired site of action. Among the large variety of forms of the therapeutic agent, micro and nano-particles are attractive and have been extensively studied over the past few decades (Brannon-Peppas et al., 1995, Soppimath et al., 2001, Mainardes et al., 2004, Park et al., 2010. Brannon- Peppas, 1995). Among the various manufacturing methods of microparticles (Chow et al., 2007; Kumar et al., 2000; Chan et al., 2003), such as wet chemistry, spray freeze drying and spray drying, we focus on spray drying, which involves the drying process of droplets containing solids.

1.2 The need for improved understanding of the droplet evaporation

The combustion of liquid fuel in the combustion systems involves the injection of fuel spray to the hot environment. The cloud of droplets absorb heat and evaporate quickly. The combustion takes place in the gas phase. The evaporation process of droplets containing metallic particles involves complicated multiphase heat and mass. The complicated interactions encountered in the industrial processes, such as time dependent air flow fields and turbulent brings challenge. Study of evaporation of droplets containing particles provides way to observe the evolution of droplet temperature, size, evaporation rate and morphological changes involved in the evaporation process.

The evaporation kinetics of droplets containing particles consists of two stages (Mezhericher et al., 2010). In the first evaporation stage, the liquid evaporates from the droplet surface, resulting in droplet size recession and increase of particle concentration at the droplet surface. Particles accumulate on the droplet surface until the droplet surface is populated with solid particles. Then, the droplet turns into the second evaporation stage. In the second evaporation stage, the liquid-vapor interface retreats to inside of the crust. The droplet size remains unchanged. Evaporation would then occur when the liquid from within the crust reaches the crust through capillary action until complete drying is achieved.

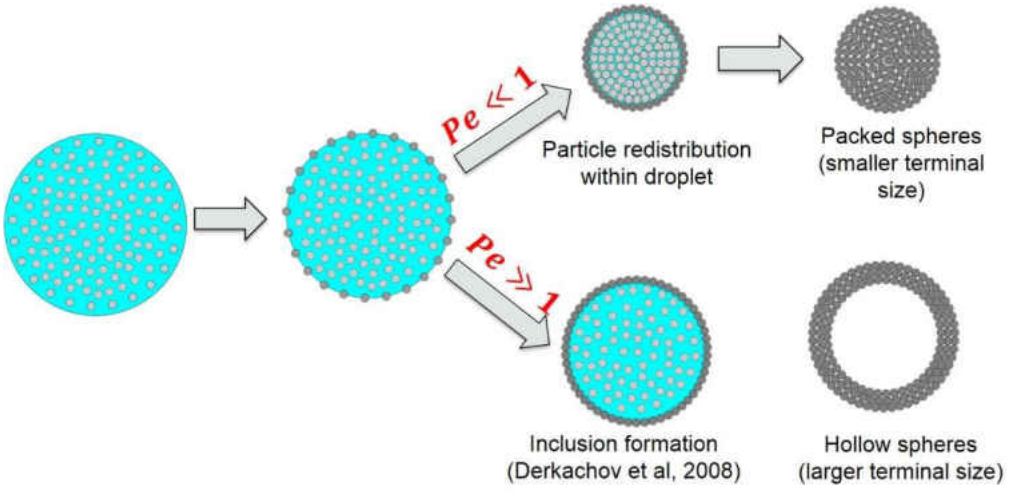

Figure 1. Effect of particles on the morphology of dry particles

The morphology of the dry aggregate particles are controlled by the Peclet number, which is the ratio of evaporation rate constant to the particle diffusion coefficient,

$$Pe = \frac{K}{8D_{pl}} \tag{1.1}$$

Where K is the evaporation rate constant of pure liquid, D_{pl} is the particle mass diffusivity in the liquid phase. D_{pl} is obtained from Einstein Stokes equation,

$$D_{pl} = \frac{k_B T}{6\pi\eta r_p} \tag{1.2}$$

The morphology the dry aggregate particle is controlled by *Pe* number. For small *Pe*, the particle diffusion rate is high and the particles have enough time to redistribute during the evaporation process. The effect of particles on the evaporation is small and a solid dry particle will be formed. While for large *Pe*, the droplet recession rate is high, the particles would be trapped at the droplet surface and a shell will be formed at the end of the drying process.

Vehring et al., (2008) gave an insightful review on the particle engineering through spray drying. The author introduced a dimensionless Peclet number, the ratio of liquid evaporation rate to the solid mass diffusivity within the droplet. For low Peclet numbers, the particle diffusion is fast compared to the droplet recession rate. In the absence of internal circulation, the particle concentration is during the evaporation. The enrichment of surface particles is small. In this case, solid particles are likely to form. For Peclet larger than 1, the surface recession rate is faster than particle diffusion. The surface becomes enriched with the particles, a shell may be formed. Figure 2 showed the dry glycoprotein particle under various Peclet number. As *Pe* number increases, the void of the dry particle is larger due to the enhanced droplet recession rate comparted to particle diffusion.

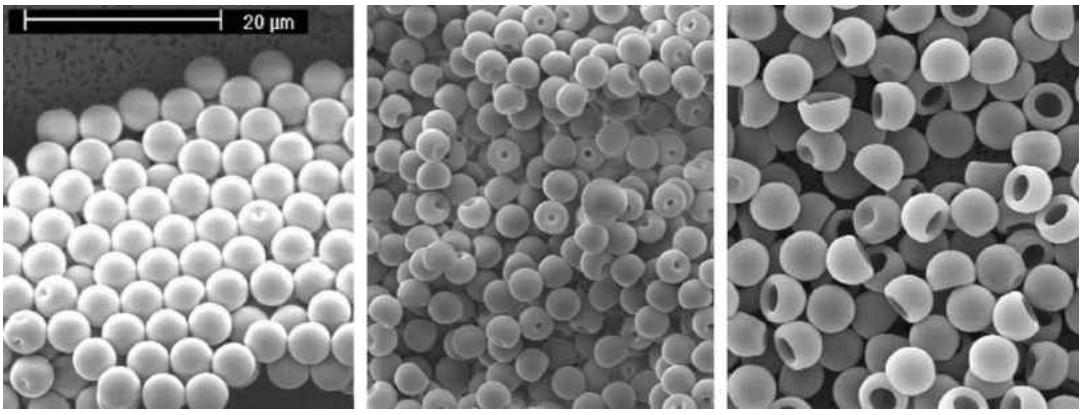

Figure 2. Morphology of monodisperse glycoprotein particles at Peclet numbers of 2.7, 5.6, and 16.8 (Vehring et al., 2008)

Besides morphology, the particle size is also important in application due to its effect on the cellular and tissue uptake, the drug delivery and the clearance by the immune system (Alexis et al., 2008). Particle size should be restricted in order to reach the areas where the drug is meant to be delivered. In treatment of cancer (Neeves et al., 2007), nanoparticles with of the size of 100-200 nm is of interest to penetrate deeply into tumor tissues through their small blood vessels and fine capillaries.

1.3 Literation review of droplet evaporation

This section is a review of relevant topics of the evaporation of droplets, with and without particles. The evaporation of droplet containing particles is a multi-phase heat and mass transfer process. The evaporation of pure liquid is reviewed, followed by the evaporation of droplets containing particles. The review is divided into two subsections, experimental findings and theoretical work.

1.3.1 Evaporation of pure liquid droplet

The mass transfer process from liquid to its surroundings is called evaporation. Consider a spherical liquid droplet in stagnant environment undergoing evaporation process. The process is assumed to be quasi-steady, at which the time scale of the change of the droplet size is large compared with the time scale over which the diffusion process around a sphere of constant size reaches steady state. Therefore, it is reasonable to consider it to be

isothermal. The rate of evaporation can be described by the linear d^2-law according to Maxwell's theory:

$$-\frac{dd^2}{dt} = K = -\frac{8D_{df}\rho_s}{\rho_l}\ln(1+\frac{m_s - m_\infty}{1-m_s}) \tag{1.3}$$

Where d, K, D_{df}, m, and ρ represent droplet diameter, evaporation constant, liquid vapor mass coefficient to the surrounding environment, concentration of liquid vapor at the droplet surface and in the environment and liquid density. The subscript s refers to a location at the droplet surface, and ∞ the location far away from the droplet surface. The parameters in the right hand side of the Equation (1.3) are constant for the steady state process, so the evaporation rate is constant. This is the classical d^2-law.

The d^2-law is the simplest possible model describing droplet vaporization, and it has the following assumptions:

(i) Diffusion being rate-controlling.

(ii) The droplet is immersed in a quiescent infinite environment.

(iii) Isobaric process.

(iv) Gas phase quasi-steadiness: the properties such as droplet recession rate, species concentrations, and temperature change rate at the droplet surface much slower than those of the gas-phase transport processes.

The evaporation processes of droplets involved in the atmosphere and in industrial processes such as droplet combustion and spray drying and are usually diffusion-controlled, at which the evaporation rate depends on the liquid diffusion rate to the droplet surface. The evaporation of droplet at small Reynolds number is applicable for the classic d^2-Law, according to Davis et al. (1987). Studies on the evaporation of droplet at higher Reynolds number have been done by Johnstone (1938) and Garner (1958) with either potential flow

theory or boundary layer theory. They introduced the dimensionless parameters, Pe and Sh ($Pe = dU_\infty / D_{ij}$, $Sh = Kd / D_{ij}$, where d is droplet diameter, U_∞, gas velocity of the gas flow, D_{ij} mass diffusivity of species i in gas j) and derived the correlation between evaporation rate and Sh, where Sh depends on Pe. The evaporation rate of the droplet at higher Reynolds number condition still follows d^2-law, which is expressed as the product of evaporation rate in the stagnant air and Sh. Levich et al. (1962) developed a correlation of mass transfer coefficient for larger Pe:

$$Sh = 1.008 Pe^{1/3} \tag{1.4}$$

Kronig et al. (1951) used singular perturbation techniques to get the expression of Sh for $Pe = o(1)$. Reviews on the experimental studies of drops evaporating into a gas stream have been given by Fuchs (1959).

1.3.2 Evaporation of droplet containing particles

As discussed earlier the evaporation of droplet containing particles is involved in various industry applications, such as particle engineering in pharmaceutical, heat transfer enhancement and combustion. The size of suspended particles differs depending on specific application. In pharmaceutical systems, nanometer sized particles are of interest (Hsieh et al., 1983), leading to the molecular level of suspended particles within the droplet. The slurry fuels in the combustion systems contain energetic particles with the size range of 30 -70 μm (Lee and Law, 1991). The particle size in nanofluid is chosen to be smaller than 100 nm because of the capability of nanofluid in enhancing thermal conductivities in the molecular level.

1.3.2.1 Experimental studies

In the past few decades, the most common experimental techniques on studies of the evaporation of single droplet containing particles are categorized into three groups (Fu et al., 2012): pendant droplet, droplet levitated by acoustic of aerodynamic fields and free falling droplet as shown in Figure 3.

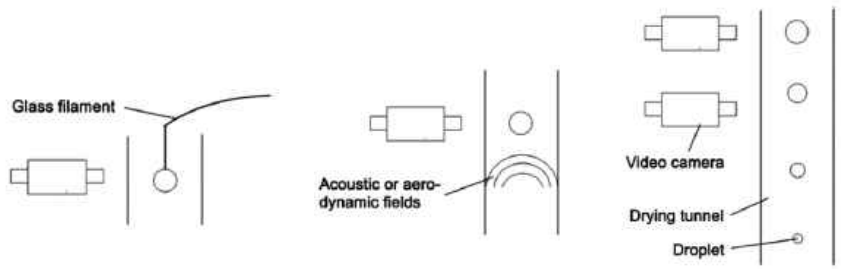

(a) (b) (c)

Figure 3. The three experimental methods of single droplet: (a) droplet suspended on a gfilament; (b) droplet levitated by acoustic or aerodynamic fields; (c) free- falling droplet (Fu, 2012)

Pendant droplet method is an intrusive approach, in which a single droplet is suspended by a thin filament. The connection between the droplet and filament allows the connection of external measurement device such as micro-balance to get the change of droplet mass. The whole particle formation process of a single droplet can be observed and particle morphology and drying rate can be easily investigated. Ranz et al. (1952) investigated the factors that influence the evaporation of water drops containing suspended solids by suspending a millimeter droplet from a feed capillary in the air stream. The study was performed under different Reynolds numbers ranging from 0 to 200. The author discovered that for droplets containing insoluble solids, the droplet initially behaves like pure liquid until a solid structure is formed. After that the evaporation rate gradually

decreases and the temperature increases due to the additional resistance of the crust. Later, Ranz and Marshall (1952) investigated the weight loss and temperature history during the evaporation process of water droplet containing 26.0 wt. % coffee extract. The evaporation process is consists of two stages. In the first stage the evaporation occurs from the liquid surface and the evaporation rate is comparable to that of pure liquid droplet. A second period starts when a solid crust is formed and the evaporation rate gradually decreases. Cheong et al. (1986) studied the evaporation process of slurry droplet by suspending the droplet from the thin film thermocouple in flowing air. The experimental results show two drying stages, an initial constant evaporation rate period and a falling evaporation rate period after a crust is formed. The formation of crust is defined by a critical moisture content value at the droplet surface. The falling rate period happens as the crust thickens. Nesic et al. (1991) studied the evaporation kinetics of water droplet containing 30 wt. % colloid silica. The experiment observed that the initial evaporation is controlled by the mixing and diffusion of solids within the droplet, which is caused by the vigorous internal circulation.

Chen et al. (2010) used pendant water droplet with addition of laponite, Fe_2O_3 and Ag nanoparticles to study their effects on evaporation rate. They observed a transition of droplet evaporation rate from a constant to another constant. The author attributed to the change of latent heat. Gan et al. (2011) studied the evaporation characteristics by adding 0.5 wt.% and 2.5 wt.% aluminum nanoparticles under natural and weak forced convection conditions. The experimental observations show the evaporation deviates from classical d^2 law at natural convection and behaves like pure liquid at weak forced convection.

Pendant droplet approach has limitations. Because of the intrusive filament, the suspended droplet experiences density gradient as well as particle concentration gradient

along the droplet surface due to breaking of spherical asymmetry. The pendant droplet approach is also limited to the millimeter size range, where internal circulation and rotation of droplet cannot be avoided.

Charlesworth et al. (1960) observed the evolution of crust formation resting on the surface in pendant droplets. During the crust formation process, the solid phase first appeared at the bottom of the droplet and gradually develops along the droplet surface until the entire surface is covered. The author attributed the phenomena to the existence of spherically asymmetry. For a droplet with spherical symmetry, it is expected that the termination of first drying stage coincides with the starting of second stage.

Figure 3 (b) shows the configuration of a single droplet suspended by aero-dynamic fields or acoustic wave. In the system, an upward force is applied to balance the droplet weight. In the acoustic levitation system, a standing sound wave is established to provide a regime close to acoustic resonance (Yarin et al., 1999). The size of the droplet ranges from 100 μm to 1cm. The droplet was levitated at a fixed position which allows droplet size, morphology and kinetic parameter be monitored.

Yarin et al. (2002) used acoustic tube levitator to study the size history during the evaporation process of aqueous droplets with solid glass beads. The experimental results show two distinct evaporation stages. At the 1st stage, liquid evaporation proceeds from the droplet surface. The 2nd stage starts from a fast precipitation of particles at the droplet surface. At the 2nd stage, the droplet size remains unchanged, while liquid evaporation still proceeds. Saha et al. (2012a) used infrared thermography and high speed imaging to study the structure formations of acoustically levitated droplet with nanosilica suspensions. They found that bowl structures are dominant at low initial particle concentrations and ring

structures are dominant at high concentrations. In another paper by the same authors (Saha et al., 2012b) detailed explanation on the effect of acoustic-steaming induced flow on the evaporating nanofluids droplets is provided. The migration of nanoparticles due to internal convective flow from a density stratification leads to force imbalance. The structure formation is controlled by the initial particle concentration.

The disadvantage of the acoustic levitation is that the droplet suffers from shape distortions due to ultrasonic and aerodynamic field. It is expected the evaporation rate of droplet under the acoustic or aerodynamic streaming is larger than those under gas convection induced by flow (Yarin et al., 1999).

In the aerodynamic levitation system, the droplet is maintained in the system where the stream velocity is controlled to provide a balance between the drag and the gravity forces (Schiffter et al., 2007). Miura et al. (1977) suspended a distilled water drop in the air flow stream. They studied the convective heat and mass transfer of water drops in the air stream at velocities of 7.5-9 m/s and temperatures of 53 -75 °C. With the fixed droplet position, the evaporation rate, temperature and the surface morphology can be monitored by a video camera coupled with infrared radiant meter. The gas drag force in the aerodynamic levitation system can also introduce vigorous internal circulation, which affects the heat and mass transfer.

Lee and Law (1991) studied the gasification of slurry droplets. They found that the droplet evaporates as that of base liquid before the crust forms. However, turbulence in the gas stream may cause fluctuations in pressure, leading to the instability of the droplet, and causing the droplet to fall out of the gas stream.

Another single droplet evaporation system - the free falling droplet approach is shown in Figure 3(c). The system allows a continuous and stable chain of monodisperse droplets to freely fall through the tube. Lee and Law (1991) studied the gasification process of a freely falling carbon slurry droplet. It is found that the effect of solids on the evaporation of slurry droplet is limited and the evaporation of the slurry in the first stage is closely approximated by pure liquid, which obeys the classic d^2 -law. Adhikari et al. (2000) review the droplet chain technique. In all their studies droplet size was bigger than 170 μm. Vehring et al. (2007) used an improved version of droplet chain technique to study the evaporation process of aqueous droplet with monomorph protein particles. The vibrating orifice generator can generate 10 μm droplets. These authors investigated the particle evaporation process at gas temperatures of 25, 50 and 125 °C. They observed that the dried particles have little or no void space at lower gas temperature, while the void becomes bigger as the temperature increases.

A major drawback of such droplet chain technique lies in the difficulty in monitoring the evaporation kinetics. Usually the droplet evaporation rate was determined by indirect measurements such as the measurement of droplet terminal velocity (Kinzer et al., 1951). Wallack et al. (1990) improved the technique by monitoring the moisture content in the droplet being evaporated. The moisture content provides much more related information of the droplet evaporation, but the system is more complicated (Fu et al., 2012).

The experimental studies described above have provided insightful view on the evaporation mechanism of single droplet containing solids. However, the experimental approaches have restrictions. For pendant droplet approach, the intrusive fiber brings challenge in understanding evaporation of spherically axisymmetric droplet. For acoustic

wave and aerodynamic levitation approaches, the internal circulation complicates the heat and mass transfer by introducing other convective transport process. Also, in industrial applications the evaporation of micro/nano meter size droplet is of interest, while the droplets that are studied in the above experimental techniques are limited to hundreds of micrometer or millimeter size range. The introduction of vibrating orifice generator in the novel droplet chain technique allows the study of droplet down to 10 micro meters. However, the free falling droplet brings challenges in monitoring the evaporation process. Therefore it is necessary to develop an experimental technique that allows instantaneous observation of evaporation of a free standing micro or sub micro droplet which contains insoluble nanoparticles for the purpose of this study.

1.3.2.2 Theoretical studies

In last few decades, the theoretical study of the evaporation process of droplet containing particles has drawn growing interest. Cheong et al. (1986) developed a receding interface model of the evaporation of slurry droplet. The model describes the evaporation process in two stages, an initial constant evaporation rate stage and a falling evaporation rate stage due to the formation of a crust. The falling-rate evaporation period happens when the crust thickens. The evaporation rate in the second stage is controlled by the existence of resistance of the crust. N. Abuaf et al. (1985) used a first-order model to predict the evaporation process of a slurry droplet. The model hypothesizes that the evaporation occurs in two stages. In the 1st stage the evaporation is gas-side-controlled diffusion at the droplet surface. Then the droplet enters into the second phase at a pre-specified critical solid-liquid mass ratio when the particles cannot compact anymore. Lee et al. (1991) divided the evaporation process of

slurry droplet into three periods, regress-diameter period, transition from regressing-diameter period to rigid-shell period and rigid shell period. In regressing-diameter period, gasification is described by the classic d^2-law. The effect of particles on the gasification process is not accounted for. In the transition from regressing-diameter period to rigid-shell period, the gasification continues with increase of particle density at the droplet surface until it reaches a critical value, at which the particles cannot compact anymore. After then the crust layer thickens until it reaches a critical value. A rigid, porous shell is established. In the rigid-shell period, an expanding spherical vapor bubble within the shell is assumed to describe the mass transfer. The gasification rate through the shell is constant. The diameter of the inner surface of the shell varies cubically with time. In the model the particle diffusion within the droplet is not considered and slurry particles are assumed to be motionless.

Nesic et al. (1991) simulated the evaporation kinetics of a water droplet that is suspended in air stream. Their model adopted five-stage concept involved in the evaporation process: initial heating, equilibrium evaporation, crust formation and growth and porous particle evaporation. For simplicity, the first two stages are considered to be constant evaporation rate stage and the rest are defined as the declining evaporation rate period. The model is validated by the evaporation of water droplet containing colloidal silica using the aerodynamic suspension technique. In the model the internal convection is accounted for by modifying the solid mass diffusion coefficient.

Levi-Hevronia et al. (1995) proposed a one-dimensional two phase flow model to describe the simultaneous mass, heat and momentum transfer for a parallel steady-flow pattern of coal slurry droplets. Compared to the model developed by Abuaf et al. (1987), this model takes the gas temperature change into account. The evaporation process is divided

into two stages. In the first stage the evaporation rate is controlled by the gas phase resistance, which obeys the classical d^2-law. The transition from the first stage to the second stage is defined by a critical solid-to liquid mass ratio. Elperin et al. (1995) divided the evaporation process in two stages, gas phase resistance controlled stage and the second stage after some critical solid-liquid mass ratio is reached. In the second stage, the shell fragmentation caused by compressibility and filtration of a gas-vapor mixture was discussed.

Minoshima et al. (2001) developed a simplified spray evaporation of slurry droplets.The particles were considered motionless within the droplet and were trapped at the droplet surface by surface tension. The shell was formed when the particles form a dense packing mode where particles could not compact anymore. The shell formation was described by the maximum particle volume fraction, 0.6. After the shell was formed, the droplet surface was assumed to be the filtrate interface, which is pushed by pseudo-external pressure. When pressure difference through the particle layer (the shell of the droplet) is larger than the buckling pressure of the hollow droplet, the outer particles move inward to yield the smaller droplet diameter. The buckling pressure increases as the shell becomes thick. When buckling pressure equals the pressure difference through the particle layer, the solid aggregate is formed.

Yarin et al. (2002) theoretically studied the evaporation of a droplet containing particles with the acoustic levitation method. The evaporation of the suspension droplet consists of two stages: Stage I, the droplet recesses due to the liquid vapor diffusion toward the surrounding environment. Stage II, the droplet size is unchanged after shell formation and the liquid within the shell evaporates and blows through the pores of the crust. In this

model the concept an effective “liquid radius” was adopted. Balance equations of mass and volume fraction of the liquid were used to calculate the liquid size history.

Seydel et al. (2006) applied population balances approach to simulate the microscopic aggregate structure during the evaporation process of a suspension droplet. Different from the models discussed so far, the definition of the beginning of the second evaporation stage is when the particles form dense packing at the droplet.

Mezhericher et al. (2007) developed a model including initial heating up in the 1st evaporation stage and the time-dependent character of the heat transfer in the evaporation process. The evaporation process in the 1st evaporation stage is analogous to that of pure liquid, and the evaporation rate is the same as that of pure liquid. The termination of first evaporation stage was defined at when a dry porous solid crust was formed.

Vehring et al. (2007) used both theoretical and numerical models to describe the coupled heat and mass transfer equations involved in the evaporation process. The model adopted species diffusion equation to describe the instantaneous distribution of solids within the droplet.

Dalmaz et al. (2007) developed a model to describe the both mass and heat transfer involved in the evaporation process of water droplets containing suspended solids. In the model, evaporation rate is initially constant followed by a falling rate process resulting from the additional resistance of the crust. From the model, the recession of the outer diameter of the droplet is due to loss of water vapor through convective mechanism in the constant evaporation rate period. During the falling evaporation rate period, the droplet size remains constant due to the formation of shell.

Derkachov et al. (2008) used molecular dynamics to simulate the evolution of morphology during the evaporation process of a water suspension droplet. The particles diffusion and the structure of the dry are determined by the particle mobility and the droplet recession rate. The morphology history showed that there are several regimes.Initially, the particles density at the droplet surface is small. As evaporation proceeds, the particles are trapped at the droplet surface due to the droplet shrinking. It can be seen in Figure 4 that islands of particles are formed at the droplet surface (see Figure 4). For longer time, large islands and high-coverage patterns form a layer or a shell of nanoparticles. Further evaporation leads to collapse of the shell and a solid structure is formed.

Handscomb et al. (2009) incorporated population balance approach to study the evaporation of droplets with solid. The formation of a shell is defined by a predefined volume fraction, 0.6, at which the solid particles at the droplet surface can no longer freely move past each other to be drawn into the center of the droplet. The droplet ceases to shrink at this point.

Mezhericher et al. (2010) gave a review of the theoretical studies on the droplet evaporation kinetics. The theoretical models were categorized into following types: empirical model that is developed based on the characteristic evaporation curve(CDC); numerical model that describe the evaporation process based on the conservation equations of mass, momentum, energy and species, and population balance approach.

Gan et al. (2011) solved population balance equation (PBE) to help explain their experimental observations. The author attributes the reduction of evaporation rate under natural convection to the obstruction of large aggregate to the diffuse of liquid to the surfaces.

For natural convection or weak forced convection, the aggregates formation time is larger droplet recession. The effect of aggregates on droplet evaporation is weak.

Mezhericher et al. (2011, 2012) developed a model to describe the heat and mass transfer phenomena in the first stage. These authors divided the stage into two morphologically different periods: liquid evaporation before the shell formation and shell submerging after the shell formation. The "after the shell formation" stage is defined as when a layer of shell is formed at the droplet surface. They assumed that before shell is formed the particles were submerged in the liquid and the liquid evaporated until a menisci with particles cap showing at the droplet surface appears. During the shell thickening period, the compression of shell result in the buckling and shrinkage of the shell. If the shell is recessed, the particles would be submerged into the liquid and the contracted shell would be covered by a liquid layer. The droplet evaporation included many repetitive steps of liquid evaporation from the droplet surface recession. The authors argued that due to the rapid submergence of the shell, the evaporation rate after the formation of the first layer of shell was the same as that of pure liquid until the thickening shell became strong enough to overcome the capillary compression. Then the evaporation rate decreases due to the reduced exposure of liquid to the surroundings.

The above evaporation models of droplet containing insoluble particles have provided important insights. However, most of the models ignore the effect of particles on the first evaporation stage and regard the evaporation rate in the first stage is regarded as the same of the pure liquid. Furthermore the moment of shell formation could not be calculated, instead it has to be determined by a predefined solid-to-liquid ratio according to the given properties of particle material. Neither do the simplifications allow the calculation

of particle concentration within the droplet as well as the particles agglomeration on the droplet surface. Evaporation of droplet suspension can result in various morphologies during the evaporation process (Vehring et al., 2008). Most evaporation models with insoluble particles focus on the effect of second evaporation stage on the dried particle morphology, while the particles accumulation on the droplet surface in the first stage is of less interest. Such simplifications may restrict the capability of the model to monitor the morphology change during the evaporation process and therefore the structure of the dry particle. Derkachov et al. (2008) studied the aggregate morphological change using light scattering method (shown in Figure 4). The inhomogeneity of the nanoparticle concentration during the whole evaporation process shows the existence of aggregate islands in the first evaporation stage. For the pure liquid droplet evaporation, the liquid vapor can diffuse through the whole droplet surface. While during the evaporation of liquid suspension, the aggregate islands block the area the liquid vapor can go through, affecting the evaporation rate. Recent findings by Chen et al. (2010) and Gan et al. (2011) show that the evaporation rate may change depending on the evaporation medium temperature, particle material, size of particles and gas stream velocity.

It can be concluded that to study the effect of particles in the first evaporation stage, it is necessary to develop a theoretical model that allows the explanation of experimental findings such as decrease of evaporation rate constant in the 1st evaporation stage and help with the industrial design.

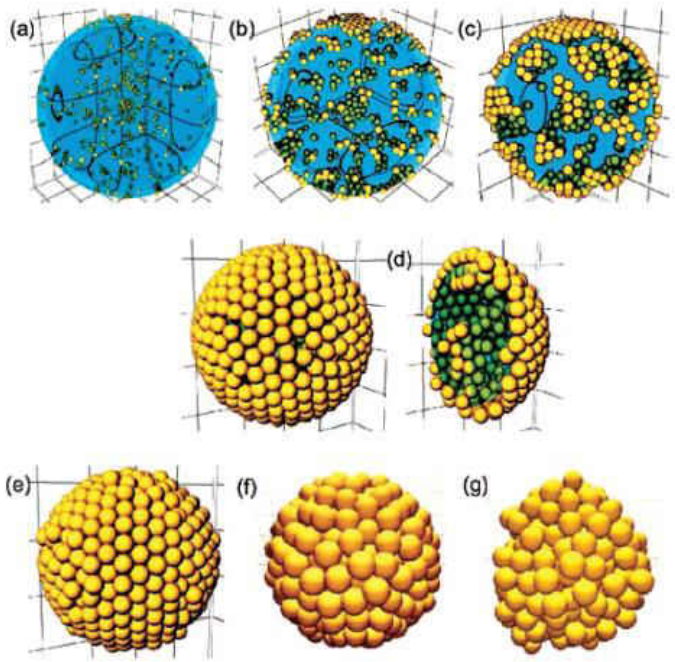

Figure 4 Morphological evolution from numerical simulation illustrating the evaporation dynamics of an aqueous droplet containing 200 nm polystyrene particles (Derkachov et al., 2008)

1.4 Scope of the study and thesis outline

As discussed in section 1.4, many researchers have adopted an assumption that prior to crust/shell formation the evaporation rate of droplets containing insoluble particles follows the d^2- law with a constant value of K, just like pure fluids. When crust is formed, the observed diameter is also defined as the terminal droplet diameter.

A recent study on evaporation of water droplets containing various insoluble nanoparticles found that K decreases with droplet diameter that in turn decreases with time (Chen et al., 2010). The investigators of this study suggest that the d^2-law is closely followed except that the values of K changes with time; they proposed an apparent latent heat of vaporization that increase with time and with the decreasing droplet diameters.

Another study (Gan, 2011) investigated the evaporation characteristics of several hydrocarbon liquids containing aluminum nanoparticles under forced convection at varying gas flow temperatures. It was found (a) that the deviation from the d^2-law (i.e., non-constant K) is more pronounced under forced convection than under natural condition conditions, as expected, (b) that under both forced and free conditions the value of K decreases with time and thus with decreasing droplet diameter, and (c) that the deviation from the d^2-law is more pronounced with higher initial particle concentrations. The authors of this study suggest that the deviation results from the particle aggregation inside the droplet. As evaporation progresses, the size of particle aggregates (again, inside the droplet) increases, lead to hindering the internal diffusion of liquid.

The studies described above (Chen et al., 2010 and Gan et al., 2011) on the evaporation of droplet containing particles have provided profound insights, but there still remain many question., such as the mechanism that leads to the increase of apparent heat of vaporization and how particle aggregates hinder internal diffusion of liquid are not fully understood.

In the study by Derkachov et al., 2008 a numerical simulation of the inclusion process (the capturing of nanoparticles on the regressing droplet surface) reveals that the particle density on the regressing surface, forming "islands," increases with time (while particles also agglomerate within the droplet). This observation suggests that the surface area from which evaporation occurs might be smaller than that determined by the droplet geometry. In other words, the part of the droplet surface occupied by the islands formed by inclusions effectively reduces the liquid surface area for evaporation.

This dissertation aims to provide a full understanding of the evaporation mechanism in the evaporation of single droplet containing particles experimentally and theoretically. The conventional experimental techniques discussed above have their drawbacks, to study the effect the particles on the evaporation of liquid suspension, a nonintrusive levitation method that allows the observation of evaporation of micro-size droplet is needed. In this thesis, the electro-dynamic balance (EDB) is introduced. This droplet suspension technique is capable of suspending droplet diameters of a few tens or micrometers (Davis, 1978 and 1980) that are desirable for investigating both diffusion-rate controlled and kinetically controlled evaporation regime. To use EDB, the droplet would have to carry electric charges, which requires integrating the capability of adding electric charges to droplets with droplet generation.

To dope droplets with electric charges, the electrospray (ES) technique can be used. By its very nature and design, spray droplets generated using the ES technique are electrically charged and is accelerated toward the oppositely charged target. The combination of EDB and ES provides an effective tool suited for the study of droplet evaporation. The ES technique is capable of producing a wide range of droplet sizes, from nanometers to approximately 100 μm. For a given combination of flow rate and the electric conductivity of the fluid, a nearly mono-dispersed spray of droplet can be produced. Droplets thus generated carry static electric charges and, when placed in a properly designed electric field, can be suspended immediately followed by experimental probing prior to significant evaporation (this is especially notable as the d^2-law indicates that smaller droplets evaporate faster than larger droplets). The detailed principles on the EBD and ES will be discussed in Chapter 2.

In Chapter 3, an analytical model is described to quantitatively address the combined effects of (i) the initial particle concentration in the droplet and the particle mobility within the liquid, i.e., a Peclet number (Pe), and (ii) the surface coverage by particles on the deviation of the d^2-law. The model is an extension of the theory of evaporation of pure liquid droplet. As evaporation proceeds, the gradual accumulation of particles at the droplet surface alters the surface heat and mass transfer and the boundary conditions are modified. The aggregates development process is described through species diffusion equation. The developed model is validated by the published experimental data. Then a discussion based on the model is provided to gain a better understanding of how Peclet number, initial solid concentration, particles size and experimental conditions affect the evaporation kinetics in the evaporation process, with the aim of guiding the industrial process and device design.

The effect of internal circulation on convection is addressed in Chapter 4. To better understand the convection transport process, the length and time scales of convection, diffusion and droplet shrinking processes are compared.

Chapter 5 summarizes the major findings of effort of this dissertation.

CHAPTER 2. EXPERIMENTAL METHODS

As we argued in Chapter 1, the ideal experimental approach that completely isolates small droplets is through electrodynamic balance (EDB). However, to implement this method and obtain useful results requires several subsystems of the experimental apparatus. These subsystems include: charged droplet generation, droplet injection, droplet levitation, and visualization. In this Chapter we discuss the theory and implementation of components of the experimental apparatus and show how they work together to lend us the powerful tool to investigate the evaporation of sub-100 micron droplets elevated by electrostatic force,

2.1 Droplet generation

Many conventional droplet generation methods rely on the microdispening of liquids by a syringe and hypodermic needle (Gan, 2011; Imanura, 2005 and Nesic, 1991). This approach limits the droplet size to be comparable with the capillary length $L_c \sim (\gamma/\rho g)^{1/2}$, where γ is the surface tension, ρ is the liquid density, and g is the gravitation constant. Typical liquids have a capillary length of ~1mm, which makes the droplet size too large for our investigation due to the potential complication brought by internal circulation. On the other hand, many applications of interests, such as in internal combustion engines, the droplets size are usually around 100 μm to increase combustion efficiency and reduce pollution emissions..

To generate sub-100 μm droplets, one mature and popular technique is inkjet. The inkjet head uses a short pressure pulse generated either thermally or piezoelectrically to expel one or more ~100 picoliter liquid droplets out of a nozzle (typically about 30 μm in

orifice diameter to avoid frequent clogging). The working principle of inkjet may impose several restrictions on the type of suspension and solution it can handle. For example, the IJP limits the liquid viscosity to 20 mPa (Holland, 1983). Also, the droplet diameter generated by inkjet is > 10 μm because the inertia based atomization requires the droplet size to be comparable to nozzle inner diameter.

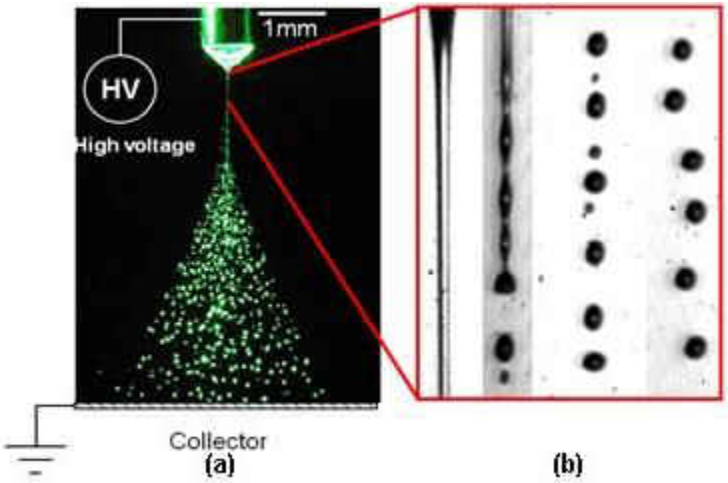

Figure 5 (a) Electrospray atomizer; (b) ordered breakup

One atomizer that can achieve both quasi-monodisperse and small (<100 μm) droplets is electrospray. Electrospray is the liquid atomization principle behind the 2002 Nobel Chemistry Prize recognizing Prof. John Fenn's contribution to the electrospray ionization mass spectroscopy (ESI-MS) (Fenn, 1989). Compared to other techniques discussed above, *ES* has the unmatched capability of producing monodispersed droplets in the few nm to 10 μm range (Almeria, 2014). A typical *ES* system (Fig. 4) is implemented by feeding a liquid with high electric conductivity (such as deionized water) through a tube which is charged to a few kV. The liquid at the nozzle tip has several different operation modes (Yang, 2012). Among these modes, the most widely used and studied one is the *cone-*

jet mode (Ganan-Calvo, 1997; Hartman, 2000). There, the liquid takes a conical shape (named Taylor-cone (Taylor, 1964)) resulting from the balance of surface tension and electric *norm* stress. The electric *shear* stress drives and accelerates the liquid at the liquid surface, from nearly zero velocity at the base of the cone to >10m/s at the apex of the cone (Wilhelm, 2004; Duff, 2003). This unique jetting mechanism eliminates liquid-solid friction which leads to low-pressure drop and a minimum risk of clogging.

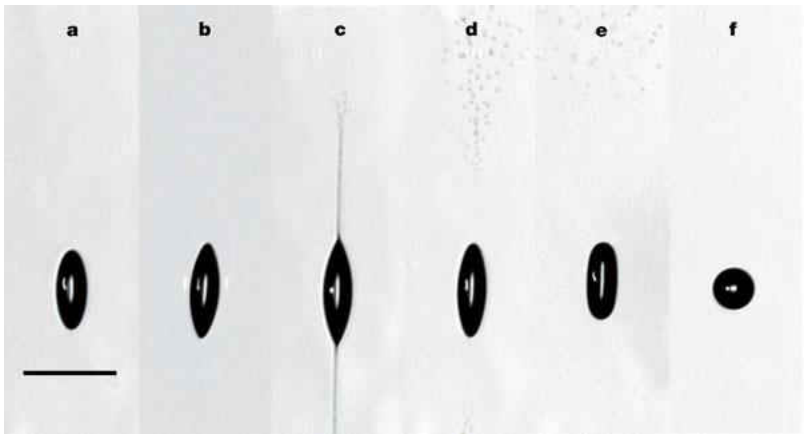

Figure 6 Coulomb fission of a charged droplet. (Duft, 2003)

It is worth noticing that during the evaporation process the surface charge density is increased due to the decreasing droplet diameter. Once the charge density reaches or surpasses a threshold at which the cohesive force as a result for the surface tension equals or smaller than the repulsive electrostatic force, the droplet becomes unstable. The unstability leads to droplet breakup and progency droplets are formed, which is referred to Coulombic fission.

It is preferable that droplet can stay as long as possible before it explodes. Rayleigh, 1882 first analyzed the stability of a charged droplet. According to his theory the instability

of a droplet occurs when the charge on the droplet reaches a critical value, which is expressed as

$$q_R = 8\pi\sqrt{\varepsilon_0 \gamma a^3} \tag{2.1}$$

where ε_0 is the permittivity constant, γ is the surface tension of the droplet, and a is the droplet radius. Eq. (2.1) shows the charge limit of a droplet decreases as droplet size decreases.

Consider a droplet with the initial size of a_0 and charge of q_0. The Rayleigh limit can be expressed as

$$q_{R0} = 8\pi\sqrt{\varepsilon_0 \gamma a_0^3} \tag{2.2}$$

Assume the droplet charge reaches Rayleigh limit when the radius decreases to a,

$$q_0 = 8\pi\sqrt{\varepsilon_0 \gamma a^3} \tag{2.3}$$

Then we have

$$\frac{q_0}{q_{R0}} = \left(\frac{a}{a_0}\right)^{3/2} \tag{2.4}$$

where q_0 / q_{R0} is defined as charge ratio. If we would like to the study the evaporation process from beginning to 10% of the initial size, the charge of the droplet needs to be less than 3% of the Rayleigh limit. The charge ratio of droplets under cone jet mode is around 70%. The value gradually decreases under pulsing mode and dripping mode. Therefore the ES will be performed under dripping mode and pulsing mode to reduce the initial charge ratio.

2.2 Droplet injection

There are two issues with using electrospray atomization for levitation. First, the electrospray process generates droplets at very high rate (~100,000 droplets/second), which are way more than we need. Second, the velocity of the droplets is too high (~10m/s) for the levitation device to be discussed in Section 2.3. Therefore, the droplet injection component will serve two functions: firstly to serve as a filter and shutter, and secondly to decelerate the droplet to the velocity of ~5cm/second.

Figure 7 illustrates the design of the droplet injection component. It mainly consists of two flat parallel metal plates with small holes at the center. The top plate functions as the first filter of droplets, as the area of the hole is only 1/1000 of the footprint of the electrospray. The second plate will further filter excess droplets. A simple mechanical shutter is placed on top of the top plate that allows manual open and block of the first injection hole. By opening the shutter for a few seconds, a charged droplet will pass both holes and reaches the levitator.

In addition, the DC electric field is established between the two plates which slow down the charged droplets. The potential difference between the two plates is slightly smaller than the voltage required for generating electrospray. This makes sense because the electrospray is a very efficient process which convert majority of the electric potential energy into liquid droplets' kinetic energy during the atomization phase; while during the injection process the droplets lose nearly all kinetic energy (99%) in penetrating the electric potential barrier.

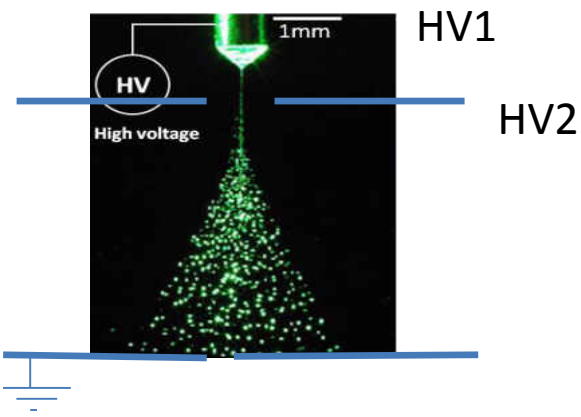

Figure 7: Design of the droplet injection component

2.3 Electrodynamic Balance Levitation System

We use the electro-dynamic balance (EDB) which is capable of levitating droplet diameters of a few tens or micrometers (Shaw, 2000; Davis, 1980; Agnes, 2002) that is desirable for investigating both diffusion-rate controlled and kinetically controlled evaporation regime (Davis, 1980). To use EDB, the droplet would have to carry electric charges, which requires integrating the capability of adding electric charges to droplets with droplet generation. The combination of EDB and ES provides an effective tool suited for the study of the evaporation and burning characteristics of fuel nanofluid droplets. Droplets thus generated carry static electric charges and, when placed in a properly design electric field as that using EDB, can be suspended immediately followed by experimental probing prior to significant evaporation (this is especially notable as the D^2-law indicates that smaller droplets evaporate faster than larger droplets).

EDB is developed based on the quadrupole mass filter that is proposed by Paul and Steinwedel (1953). A charged particles suspended by means of the electrical fields. The

device can trap particles with the size range of nanometer to hundreds of micrometer by adjusting the AC frequency and magnitude.

Many configurations have been developed according to specific application. Wuerker (1959) introduced the bihyperboloidal electrode configuration to trap ion. Straubel(1959) developed a relatively simple configuration consisting of an AC ring electrode placed in the middle of DC planes. Maloney, 1995 developed a modified version of EDB to measure the trajectories and drag force characteristic of individual particles. A simple form of electrodynamic balance with the double ring geometry was analyzed by Davis, 1990. Zheng, 2001 also introduced a double ring device to achieve control of a particle in three dimensions.

In all these electrode configurations, the oscillatory forces that is exerted by the AC filed to trap the particle. The DC field applied is used to balance the gravitational force and any other vertical forces on the particle.

2.3.1 Theory of classic bihyperboloidal EDB device

The classic bihyperboloidal configuration includes hyperboloidal endcap electrodes and a central ring electrode. The ac voltage is applied to the ring electrode to achieve the focusing. The endcaps are connected to dc voltages to introduce upward electrical force and the distribution of the positive and negative potential is adjusted according to the polarity of the charged particle. If the particle has positive charge, the positive voltage should be applied on the bottom endcap and negative voltage should be connected to the top endcap and vice versa.

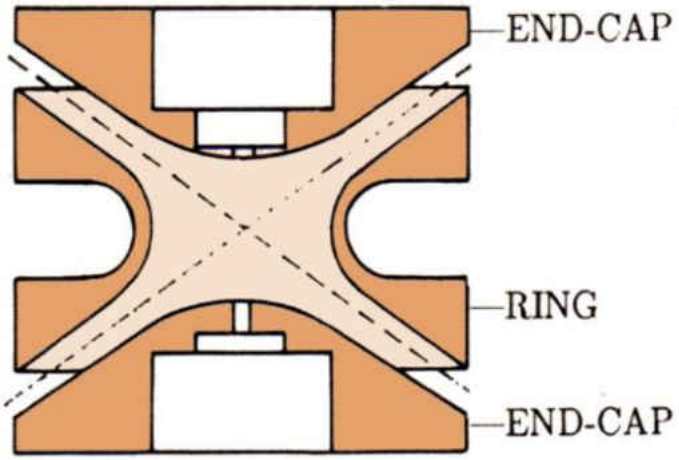

Figure 8 Schematic of the hyperboloidal ion trap
(http://static.sewanee.edu/physics/SEMINARS/HTML%20Griffith/sld004.htm)

The electric field generated by ac voltage applied on the ring electrode is expressed as

$$E_z = 2C_1 \frac{V_{ac} z}{z_0}(\cos \Omega t)\vec{k} \tag{2.5}$$

$$E_r = -C_1 \frac{V_{ac} r}{z_0}(\cos \Omega t)\vec{r} \tag{2.6}$$

where Ω is the frequency of the AC voltage, $\vec{k}$ and $\vec{r}$ are the unit vectors in the vertical and radial direction, 2 z_0 is the distance between the two endcap electrodes, E_z and E_r are electric field vectors in the vertical and axial directions, respectively. Since the geometry of the device is axisymmetric the electrical field component in the angular direction is 0. C_1 is geometric constant. For the classical bihyperboloidal configuration $C_1 = 1/z_0$, so Eq. 4.5 can be expressed as

$$E_z = 2V_{ac} \frac{z}{z_0^2}(\cos \Omega t)\vec{k} \tag{2.7}$$

From the expressions of electrical field induced by ac voltage, we can see the charged particle in the space surrounded by the electrodes is subject to periodic forces whose

strength are proportional to the distance from the center of the device. The electric field tha is produced by a dc voltage, V_{dc}, in the EDB device is

$$E_{dc} = C_0 \frac{V_{dc}}{z_0} \vec{k} \tag{2.8}$$

where C_0 is also a geometrical constant. In the electrical field of two infinitely large parallel plates the electrical field is uniform and C_0 is 1. While in the bihyperboidal configuration the electrical field is not uniform and the value of C_0 varies at different positions. Since the ac voltage is used to encounter the vertical forces when the particle is trapped in the nullpoint where the minimum electrical potential exists (the center of the device). The value of C_0 is important, which can be obtained by numerically solve the electrical field of the corresponding EDB configuration. Here the value of C_0 is assumed to be 1 from the expression of dc electrical field given in Davis, 1980. The dc electrical field at the nullpoint is expressed as

$$E_{dc} = \frac{V_{dc}}{z_0} \vec{k} \tag{2.9}$$

Suppose a charged particle is injected vertically from the center of the top endcap to a dynamic field. The trajectory of a charged particle with the mass of m and charge of q in the electrical filed are described as

$$\vec{F} = m\frac{d^2 z}{dt^2} = -C_d \frac{dz}{dt} + q\vec{E}_z - mg + q\vec{E}_{dc} + \vec{F}_z \tag{2.10}$$

and

$$m\frac{d^2 r}{dt^2} = -C_d \frac{dr}{dt} + q\vec{E}_r \tag{2.11}$$

where F_z are external forces such as the thermophoretic force , the photophoretic force and possibly, magnetic forces and so. We are not introducing any external forces here and $F_z = 0$ in our study, C_d is the drag coefficient and for a spherical particle it can be defined by

$$C_d = 3\pi d\mu \tag{2.12}$$

where d is the particle diameter, and μ is the viscosity of the gas phase.

Substitute equations 2.4, 2.6, 2.7 and 9 into equations 2.10 and 2.11, we have

$$m\frac{d^2z}{dt^2} = 2qV_{ac}\frac{z}{z_0^2}\cos\Omega t - \frac{qV_{dc}}{z_0} - 3\pi d\mu\frac{dz}{dt} - mg \tag{2.13}$$

$$m\frac{d^2r}{dt^2} = -3\pi d\mu\frac{dr}{dt} + qE_r \tag{2.14}$$

In the absence of external forces, the function of dc voltage thus becomes to overbalance the gravitational force.

$$-\frac{qV_{dc}}{z_0} = mg \tag{2.15}$$

Then Eq.2.13 becomes

$$m\frac{d^2z}{dt^2} = 2qV_{ac}\frac{z}{z_0^2}\cos\Omega t - 3\pi d\mu\frac{dz}{dt} \tag{2.16}$$

Equations 2.14 and 2.16 are second order nonlinear differential equations which are not easy to get analytical solution directly. Therefore the following nondimensional quantities are introduced,

$$\eta = \frac{z}{z_0} \tag{2.17}$$

$$R = \frac{r}{z_0} \tag{2.18}$$

$$\tau = \frac{\Omega t}{2} \tag{2.19}$$

We have

$$\frac{d^2\eta}{d\tau^2}+\left(\frac{6\pi\mu d}{m\Omega}\right)\frac{d\eta}{dt}-8\left(\frac{q}{m}\right)\left(\frac{V_{ac}}{\Omega^2 {z_0}^2}\right)\eta\cos(2\tau)=0 \tag{2.20}$$

$$\frac{d^2R}{d\tau^2}+\left(\frac{6\pi\mu d}{m\Omega}\right)\frac{dR}{dt}-4\left(\frac{q}{m}\right)\left(\frac{V_{ac}}{\Omega^2 {z_0}^2}\right)R\cos(2\tau)=0 \tag{2.21}$$

Apply transformations

$$\hat{\eta}=\eta e^{b\tau} \tag{2.22}$$

$$\hat{R}=\mathrm{R}e^{b\tau} \tag{2.23}$$

where $b=3\pi\mu d/m\Omega$, Equations 2.20 and 2.21 become

$$\frac{d^2\hat{\eta}}{d\tau^2}+\left(-b^2-8\left(\frac{q}{m}\right)\left(\frac{V_{ac}}{\Omega^2 {z_0}^2}\right)\cos(2\tau)\right)\hat{\eta}=0 \tag{2.24}$$

$$\frac{d^2\hat{R}}{d\tau^2}+\left(-b^2-4\left(\frac{q}{m}\right)\left(\frac{V_{ac}}{\Omega^2 {z_0}^2}\right)\cos(2\tau)\right)\hat{R}=0 \tag{2.25}$$

Rewrite the above two equations, eqs. 2.24 and 2.25

$$\frac{d^2\hat{\eta}}{d\tau^2}+\left(a-2q_z\cos(2\tau)\right)\hat{\eta}=0 \tag{2.26}$$

$$\frac{d^2\hat{R}}{d\tau^2}+\left(a-2q_r\cos(2\tau)\right)\hat{\eta}=0 \tag{2.27}$$

where $a=-b^2$, $q_z=2q_r=4\left(\frac{q}{m}\right)\left(\frac{V_{ac}}{\Omega^2 {z_0}^2}\right)$.Now we have the classical Mathieu Equation whose stability region has already been established. Figure 9 shows the stability region (enclosed by red lines) in parameter space of a and q_z. It has many separated regions; we can call the most left enclosed region stability region 1, the next stability region 2, etc. The solution in the r direction can be solved similarly. The stable region should be intersection of the both

directions. Compare equation (2.26) and (2.27), q_z is two times of q_r, which means the displacement in r direction is always stable as long as it is stable in z direction. Therefore the electrical field is adjusted to fulfill the stability in the z direction.

It should be noticed from equations 2.22 and 2.23 that the solutions of equations to the displacement is actually the product of the solution of Mathieu's equation and an exponentially decreasing term, therefore the stability region is expanded, which means some of the unstable region in Stability chart of Mathieu's equation is now stable due to the exponentially decreasing term. The details of the expanded stability region are derived in Appendix B.

If a particle is to be trapped in the nullpoint, it goes through a complicated trajectory before it is focused at the center. At a fixed time, if the electric field has coverage effect at the x direction, then it will have diverge effect at the z direction, and vice versa, but the overall effect is to focus the particle to the center after a complicated trajectory if we chose parameters to be at the overlapping region.

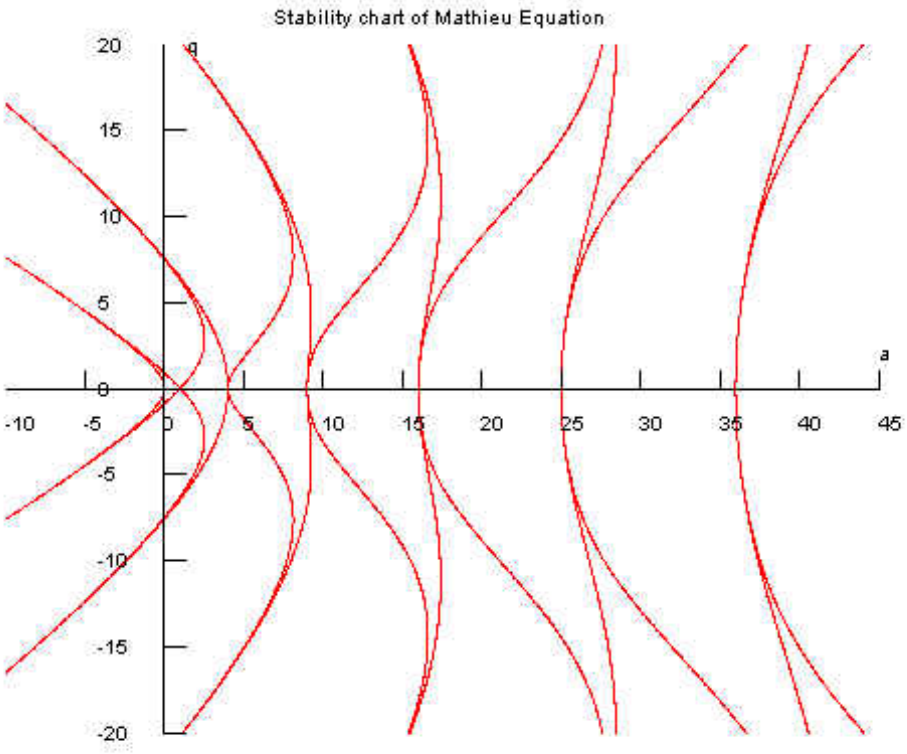

Figure 9 Stability chart of Mathieu Equation

2.3.2 Numerical approach to determine ideal operating conditions

From stability analysis in section 2.3.1 the parameters involved in determining whether trapped particles can stabilize in the nullpoint finally are V_{ac} , V_{dc} , Ω and charge mass ratio(q/m). It does not take the maximum displacement the particle can travel nor the time needed to stabilize into account. Besides satisfying the stability criteria the trapped particle should always remain inside the chamber, which means the maximum displacement the particle could travel should be less than the minimum dimension of the center to the wall of the trapping system. Furthermore once the particle is injected to the trapping system the time needed to stabilize the particle in the center also matters for some time consuming

experiment such as evaporation, reaction and combustion process. We are interested in studying the evaporation of micro sized liquid droplet. The lifetime of the droplet in our study is around a few seconds, and our goal is to study the evaporation process from the initial injected droplet. Therefore reducing the response time in trapping the droplet is important.

For the above reasons, we adopted the numerical simulation approach to solve the 2^{nd} order differential equation (2.7) with proper initial conditions. The Matlab code solving this problem is provided in Appendix C. The trajectories of ethanol and glycerol droplets with size of 10μm and 100 μm are studied under different induced velocities. The charge ratio of all the cases discussed below is 70% Raleigh limit.

The droplet is injected from the top of the four rings EDB setup right through the axis of the rings. The droplet vibrates up and down under the ac electrical field and will finally stabilize in the center point when dc is set to overbalance gravity and ac voltage and frequency was set to satisfy the stability criteria. The separation distance of ac rings is 6 mm, so the displacement should always be within the -3~3 mm during the vibration process. The simulation results shows that for a 100 μm droplet with induced velocity larger than 2 m/s the droplet can easily go out of the rings even it will stabilize finally.

Figures 10~13 list the trajectories of 100 μm droplet under various induced velocities. The droplet can go up to 10 mm under 0.7 m/s. By reducing the velocity the maximum displacement can be reduced, the droplet is maintained between the space of ac rings once the velocity (u) is 0.01 m/s. The figures also show the response time to stabilize droplet decreases as velocity decreases. Figure 11 shows the trajectory of a 100 μm droplet under the velocity of 3 m/s we can see the maximum displacement is around 7.5 mm, which is less

than that of a larger droplet (100 μm) under 0.7 m/s. From the above analysis we can conclude that the bigger droplet size needs much smaller velocity to help maintain the droplet within the EDB setup and reduce the response time to get stabilized. Since the droplet velocity from ES is usually larger than 3 m/s, the velocity should be damped before reaching the EDB setup. In our work extra upward electrical field is applied to reduce the droplet induced velocity, the detailed information will be discussed in section 2.4.

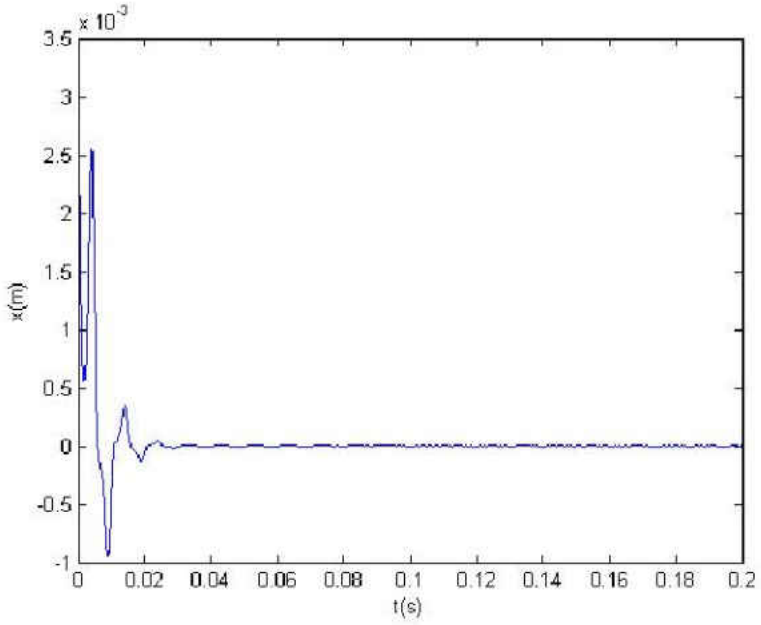

Figure 10 Trajectory of droplet in the vertical direction with d=100μm, Ω =1256rad/s, V_{ac} =2000V,u=0.01m/s

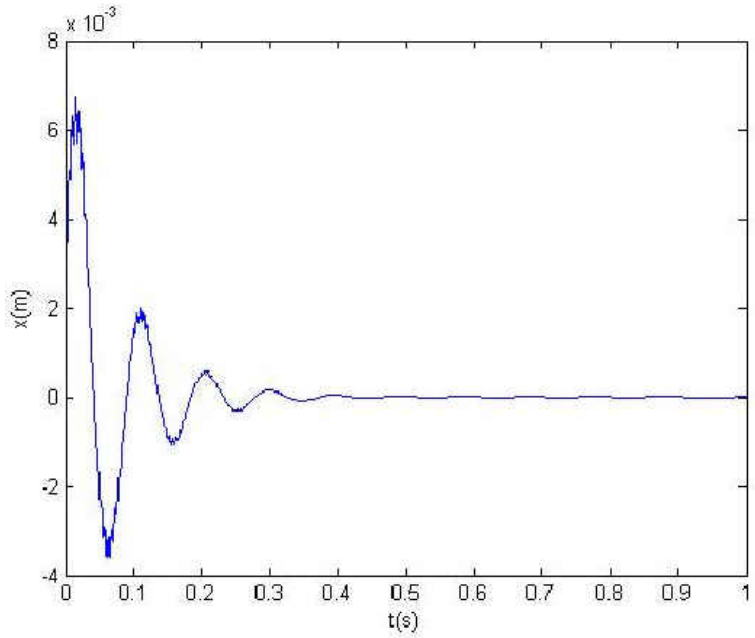

Figure 11. Trajectory of droplet in the vertical direction with *d*=100μm, Ω =1256r0ad/s, V_{ac} =2000V, *u*=0.4m/s

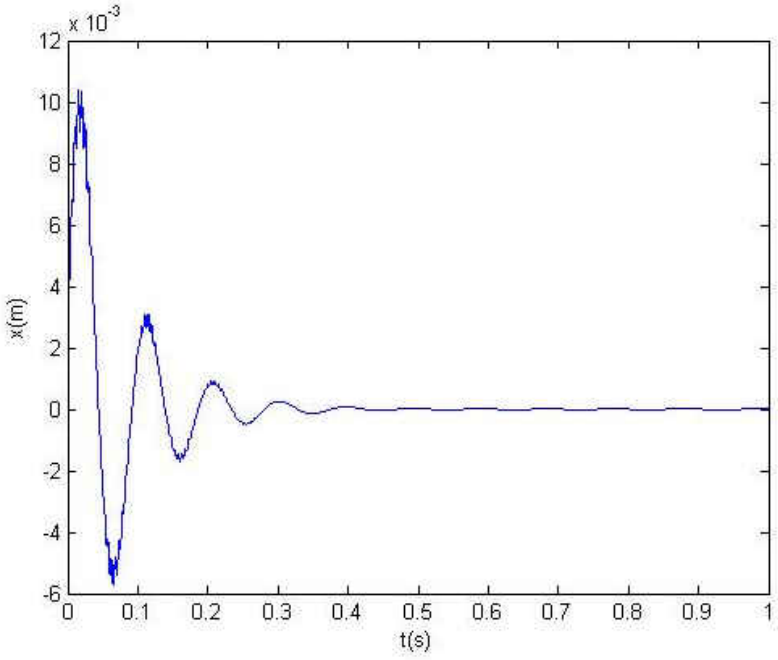

Figure 12. Trajectory of droplet in the vertical direction with *d* = 100 μm, Ω = 1256 rad/s, V_{ac} = 2000 V, *u* = 0.7 m/s

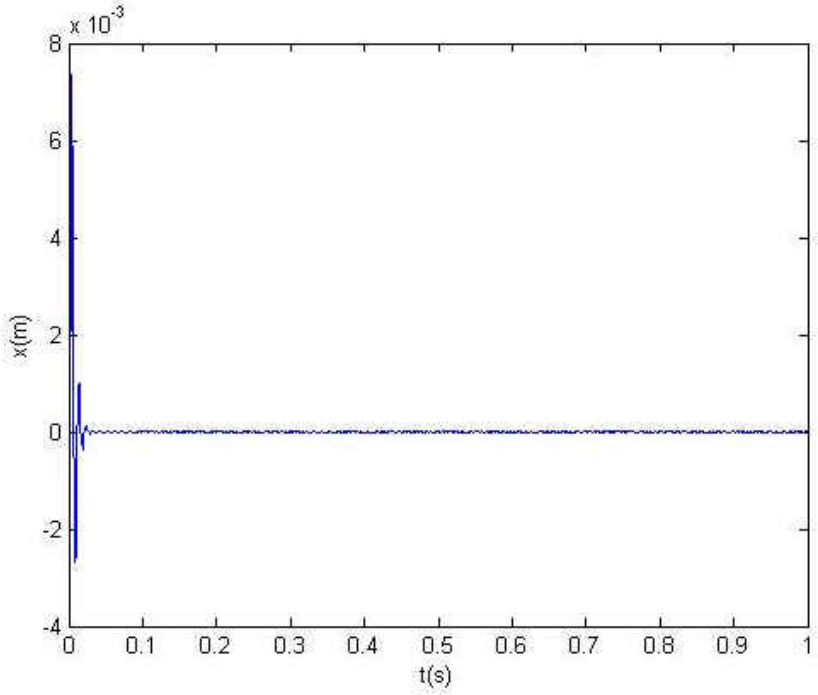

Figure 13. Trajectory of droplet in the vertical direction with d= 10 μm, Ω = 1256 rad/s, V_{ac} = 2000 V, u= 3 m/s

2.3.3 Theory of double rings EDB device

Although the classical configuration of the device is the bihyperboloidal chamber, many other configurations that are much easier to build have been developed as described in the introduction part in chapter 2.3. For the simplicity of construction and also feasibility for optical device, we adopted the simplest configuration developed by Weiss-Wrana, 1983, Ray and Souyri, 1989 and Davis, 1990. The ac and dc electrodes are replaced by four parallel rings. Figure 14 shows the geometry and circuitry. The top and bottom rings are connected to dc voltage. The relative potential difference is determined by the polarity of the charged droplet. In our study the droplet has positive charge, so the higher potential should be connected to bottom ring to induce upward electrical field. The middle rings are connected to ac voltage and the other end of the ac voltage is connected to the ac circuit with the

potential of $V_{ac}/2$. In our experiment the point is connected to ground with 0 potential, therefore the potentials of top and bottom rings become $-V_{ac}/2$ and $V_{ac}/2$, respectively. Analytical solution of the electrical field is provided in Davis, 1990.

$$E_{ac,z} = \frac{\pi V_{ac} \cos wt}{\psi(\xi_1, \xi_2)(R^2 + h^2)^{3/2}} z \tag{2.28}$$

$$E_{dc,z} = \frac{\pi V_{dc} z_0}{\varphi(\xi_3, \xi_4)(R^2 + {z_0}^2)^{3/2}} \tag{2.29}$$

where R is distance of the center point to electrodes, h and z_0 are the distances from the center point to the ac and dc electrodes, $\psi(\xi_1, \xi_2)$ and $\varphi(\xi_1, \xi_2)$ are geometrical parameters which are expressed as

$$\psi(\xi_1, \xi_2) = \frac{K(\xi_1)}{2R} + \frac{K(\xi_2)}{2(R^2 + h^2)^{1/2}} \tag{2.30}$$

$$\varphi(\xi_3, \xi_4) = \frac{K(\xi_3)}{2R} - \frac{K(\xi_4)}{2(R^2 + {z_0}^2)^{1/2}} \tag{2.31}$$

Where $K(\xi_1)$, $K(\xi_2)$, $K(\xi_3)$ and $K(\xi_4)$ are the complete elliptic integrals of the first kind. The function of $K(k)$ has the simplified approximation

$$K(k) = \frac{\pi}{2}\left\{1 + \left(\frac{1}{2}\right)^2 k^2 + \left(\frac{1 \cdot 3}{2 \cdot 4}\right)^2 k^4 + \cdots + \left[\frac{(2n-1)!!}{(2n)!!}\right]^2 k^{2n} + \cdots\right\} \tag{2.32}$$

The precision of the aproximation is smaller than 3×10^{-4} for $k < 1/2$. ξ_1, ξ_2, ξ_3 and ξ_4 have the following forms

$$\xi_1 = \xi_3 = 1 - t^2 / 4R^2 \tag{2.33}$$

$$\xi_2 = 1 - (t^2 + 4h^2)/(4R^2) \tag{2.34}$$

$$\xi_4 = 1 - (t^2 + 4{z_0}^2)/(4R^2) \tag{2.35}$$

where t is the radius of the ring electrode. Compared to the electrical field in classical bihyperboidal geometry (eqs. 2.5 and 2.7), eq.2.28 can also be written as the form of

$$E_{ac,z} = \frac{\pi V_{ac} \cos wt}{\psi(\xi_1, \xi_2)(R^2 + h^2)^{3/2}} z = 2C_1 V_{ac} \frac{z}{h} \cos wt \qquad (2.36)$$

where geometric constant of $C_1 = \pi h / 2(\psi(\xi_1, \xi_2)(R^2 + h^2)^{3/2})$, Similar to analogy in ac electrical field eq. 2. 29 can be written as

$$E_{dc,z} = \frac{\pi V_{dc} z_0}{\varphi(\xi_3, \xi_4)(R^2 + {z_0}^2)^{3/2}} = C_0 \frac{V_{dc}}{z_0} \qquad (2.37)$$

where $C_0 = \pi {z_0}^2 / (\varphi(\xi_3, \xi_4)(R^2 + {z_0}^2)^{3/2})$. The only differences of the electrical fields between classical bihyperboloidal and four rings configurations are the geometrical constants. The theoretical analysis in section 2.3.2 is also applicable for the four ring configuration.

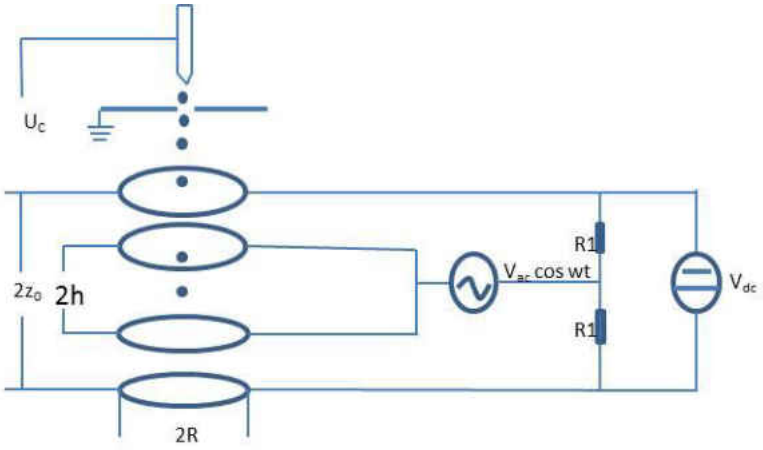

Figure 14 Configuration of the double-ring electrodynamic balance

The values of C_0 and C_1 can also be obtained with the numerical approach by solving the Laplace. For the boundary condition we use the dimension of the experimental setup (details will be shown in section 2.4), the four rings have the same dimension, the radius of the ring electrode (t) is 1.15 cm. The distance between the ring center and the electrode (R)

is 11.35mm. The separation distance of the middle ac electrodes ($2h$) is 6 mm. The distance of the two dc electrodes ($2z_0$) is 25 mm. The simulation is implemented in COMSOL. The origin of the 2-d cylindrical coordinate is set to be at the center point of the EDB setup. When calculating the electrical field induced by ac voltage, the potential of dc electrodes were set to be 0. From eq.2-29 we can see the relation between the electrical field and the z coordinates is linear at any time. To get the constant value (C_1), we only need to apply a potential to the ac electrodes and get the plot of vertical electrical vs. coordinates, the slope of the plot is $2C_1 / h$. The ac electrodes were set to be 2000 K. Figure 14 shows the electrical field in the z direction. It shows the electrical field can be approximated to be linear between the two ac rings (-0.003-0.003m) (shown in Figure 15).

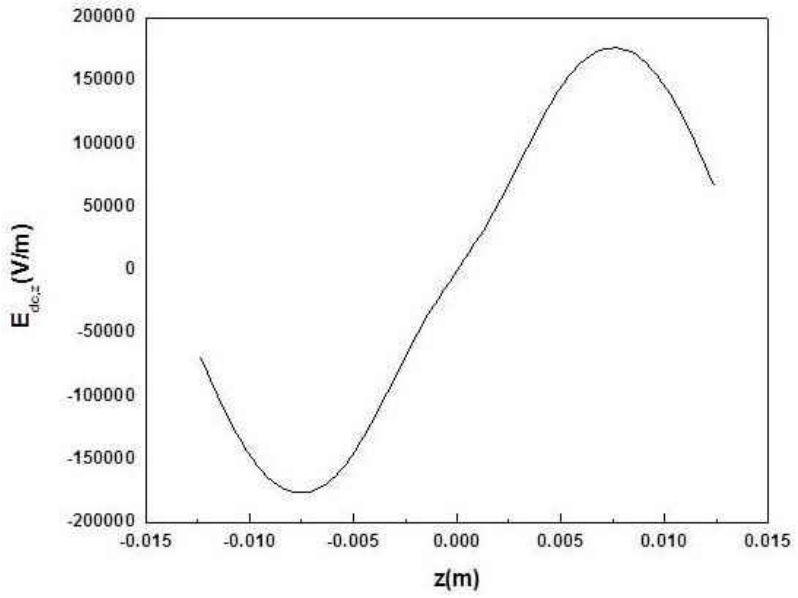

Figure 15 Vertical electrical field at V_{ac}=2,000 V

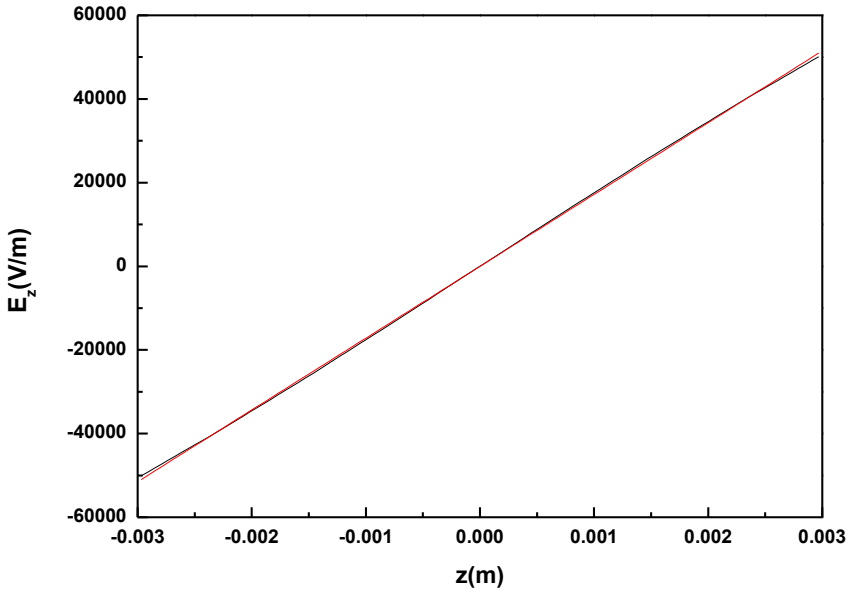

Figure 16 Zoom in picture of vertical electrical field between ac rings at V_{ac}=2,000 V

2.4 Droplet visualization

To image the micro droplet with highest possible optical resolution (i.e. only limited by the Abbe diffraction limit), great care needs to be taken on the design of the visualization subsystem. The challenges come from two aspects: first, the high AC voltage of the EDB; second, the motion blur caused by the combined high magnification rate and hovering motion of the droplet.

We used a 10x long working distance microscope lens (Edmund Optics EO M Plan Apo infinity-corrected) to allow sufficient distance away from the charged metal rings. The working distance of the lens is 33.5mm, with a focal length of 20mm. The Numerical Aperture NA is 0.28. The diffraction limit states:

$$d = \lambda_L / 2NA \tag{2.38}$$

where d is the resolution limit, λL is the light source wavelength. This suggests that with typical visible light wavelength of 540nm (green light), the resolving power of the lens is ~

1μm. It also suggests that shorter wavelength will result in slightly higher resolution. In addition, the light source should be nearly monochromatic to minimize chromatic dispersion. Because of these considerations, we choose a high power blue LED as the light source, which is collimated into approximately parallel beam.

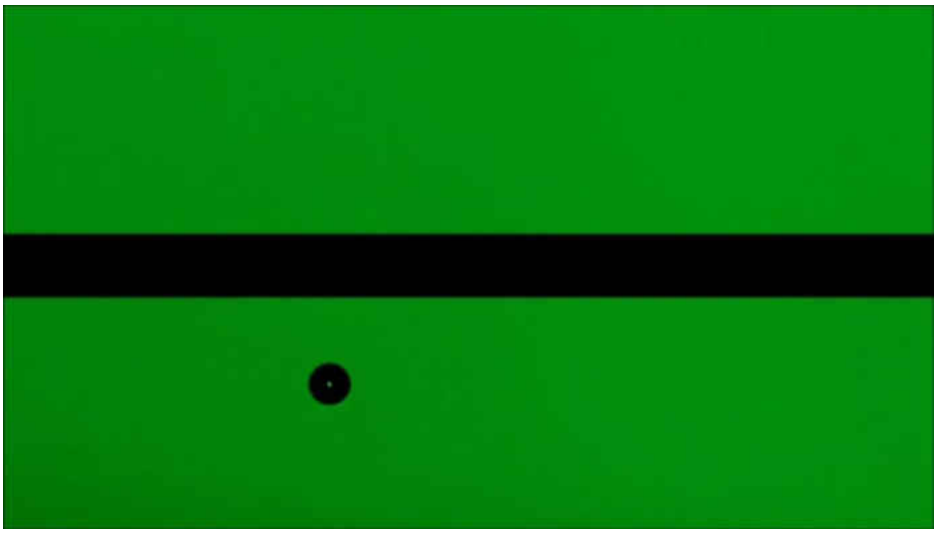

Figure 17 Single levitated evaporating ethanol droplet

The camera we used is a Canon 650 DSLR. The sensor size of the camera is 22.3 ×14.9 mm, and the pixel number is 5184 ×3456 with the pixel size of 4.3 ×4.3μm. To ensure each pixel matches the revolving power of the lens (~1μm), we added extension tube adapter to the lens and achieved 8.3x effective optical magnification.

The droplet will not be absolutely still in the EDB. The typical hovering speed of the droplet is about 5 cm/s. With 8x magnification, the image moving speed is 40cm/s. To avoid motion blur, an exposure time should guarantee the image does not shift more than half of a pixel, or ~5μs. This value is unachievable by the camera. Instead, we strobe the LED light with short pulse of ~1μs. The LED is driven by a pulse generator, which is triggered by a function generator set at 29.97 Hz (same frequency of the video mode of the camera). Note that if the

triggering frequency is not synchronize as the video mode of the camera, a rolling fringe artifact will appear on the video footage (shown in Figure 17).

2.5 The completed experimental apparatus

The complete experimental setup is shown in Figure 18, which consists of the subsystems previously described: droplet generation, droplet injection, droplet levitation, and visualization.

The atomizer is a stainless steel needle charged at positive high voltage V_1. The top plate of the injector (or extractor) is connected to negative high voltage ($-V_2$). Electrospray is generated by the voltage difference between the nozzle and the extractor ($V_1 + V_2$). After the extracted jet go through the hole (3 mm) right below the needle the jet breaks up into droplets with a certain velocity, as shown in Figure 18. The injection component and EDB are mounted on a 2-d stage to allow easy alignment. The two systems are connected with the metal rods with plastic screws on the connection parts for insulation.

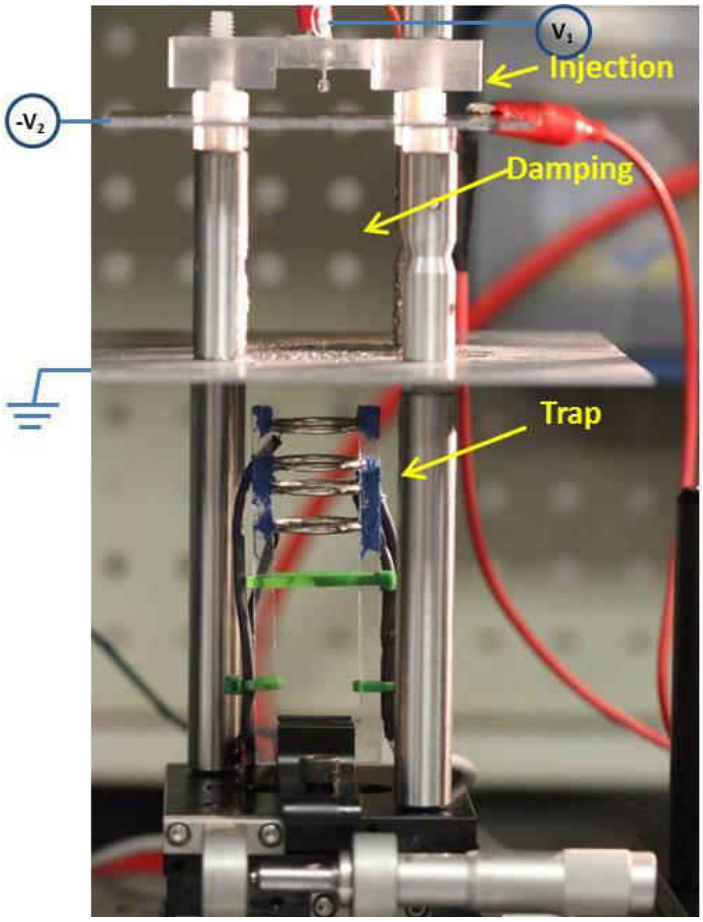

Figure 18. Experimental setup

As discussed in section 2.2 the velocity of the droplets should be reduced before entering the EDB. The injection system is formed by two parallel Alumina plates, one is used as extractor in ES system with the dimension of 2 inches ×2 inches, the other is used as ground with the dimension of 4 inches × 4 inches (shown in Figure 18). The grounded plate separates the electrical field in the damping system and that in the EDB. The reason for the lager ground plate is that the spray profile is developing as it propagates, and the radius of cross section is approximately proportional to the square root of distance it travels. The separation distance of the two plates is 2 inches, so the grounded plate has the dimension of 4 inches ×4 inches. There is one hole on the plate with the radius of 3 mm, which allows very

few droplets to go through. The holes on the two plates are aligned with the center of the trapping system. There is an upward electrical field to damp the droplet velocity. $-V_2$ can be adjusted to make most of the droplet fly back while still allows few to go through the hole in the grounded plate.

Figure 19 shows the spray profile in the injection section. Compared to Figure 20 most droplets fly upward and only a few droplets can go through the holes on the bottom plate to the trapping system. Figure 21 shows the droplet injection velocities into the trapping systems under various negative high voltages. The velocity decreases as voltage increases. As discussed in section 2.3.3 smaller velocity is good for trapping.

The four rings are inserted to a machined support to make the four rings coaxial. The support is fixed right below the grounded plate. Therefore once the droplet goes through the grounded plate it can be levitated.

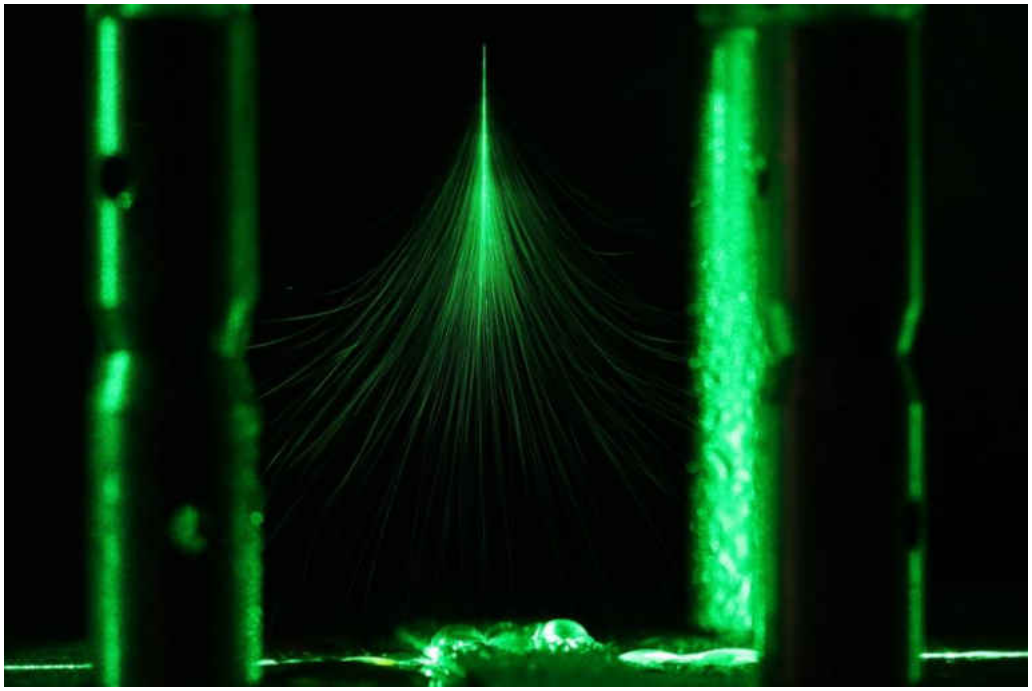

Figure 19. Electrospray profile of glycerol under cone jet mode with the flow rate of 2 ml/h without damping system

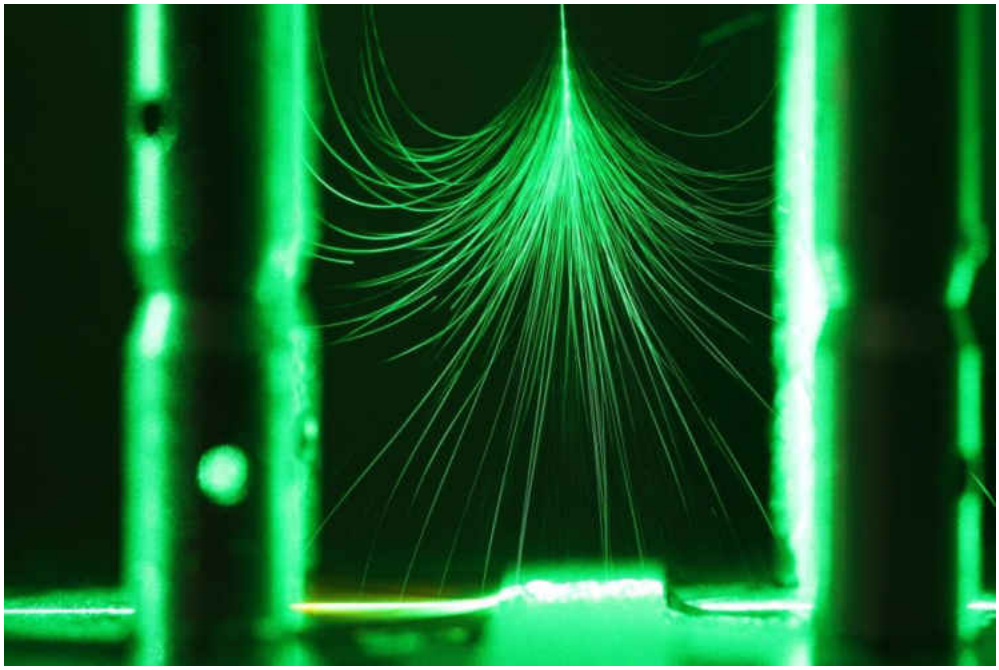

Figure 20 Electrospray profile of glycerol under cone jet mode with the flow rate of 2 ml/h with damping system by setting $-V_2$ = -0.943 kV

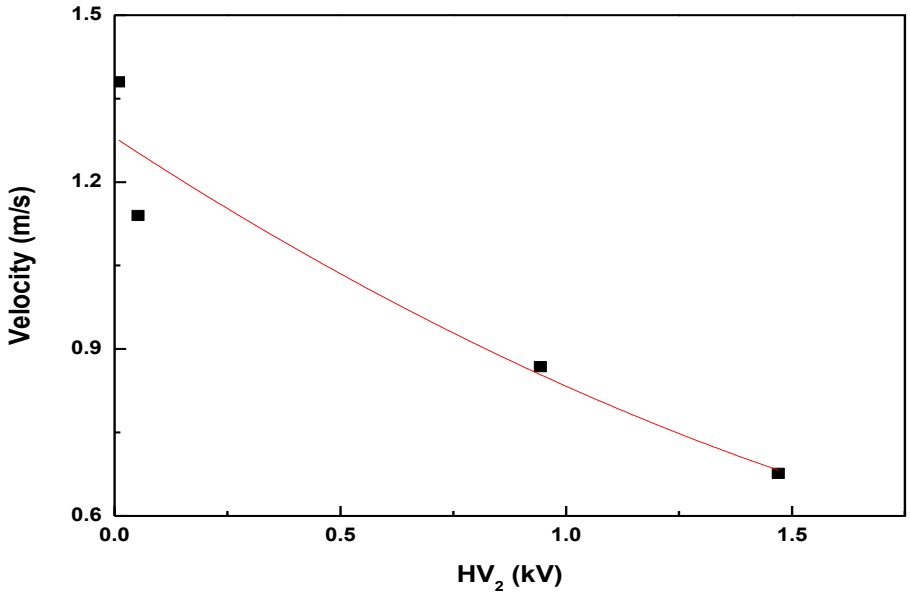

Figure 21 Droplet injection velocities under different electrical field

2.6 Performance of the experimental apparatus

We have successfully generated, injected, levitated, and imaged microdroplets of glycerol, water, and water+ethanol mixture. Figure 22 (a) shows the still image of the levitated micro glycerol droplet. The droplet size is measured through counting the number of pixels. The uncertainty is ± 0.52 μm.

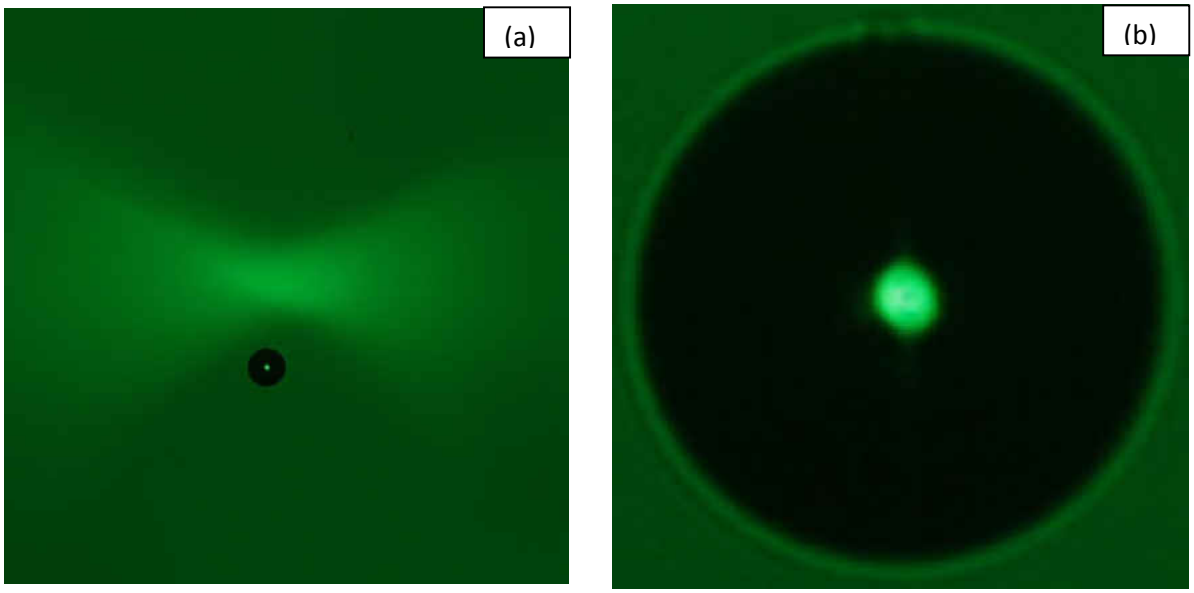

Figure 22 Microdrop imaging. (a) Direct zoom lens image. (b) Magnified image of 102 μm droplet

Because the video recording frame rate is 30 Hz, and the typical droplet evaporation time (100μm) is ~3 seconds, the complete evaporation even can be capture with 100 or more frames, which are adequate for both qualitative and qualitative investigation. For example, Figure 23 shows the image sequence of the complete evaporation history of a 90 μm water droplet with 178 images which allow full characterization of the droplet size change history.

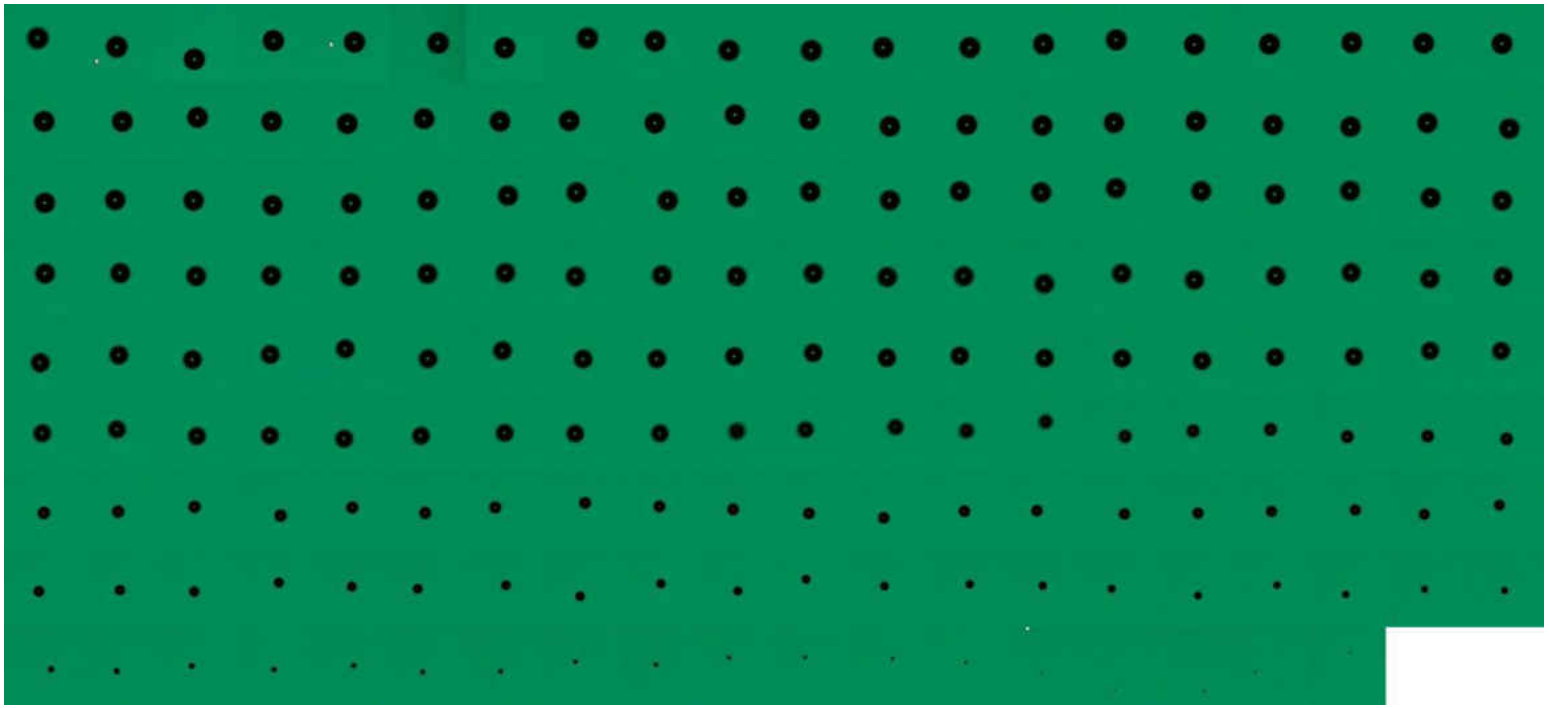

Figure 23 Complete evaporation history of a micro water droplet

Figure 24 shows the typical behavior of pure DI water, which closely follows D^2-law. This suggests our experimental setup is a powerful tool to study the evaporation of microdroplets.

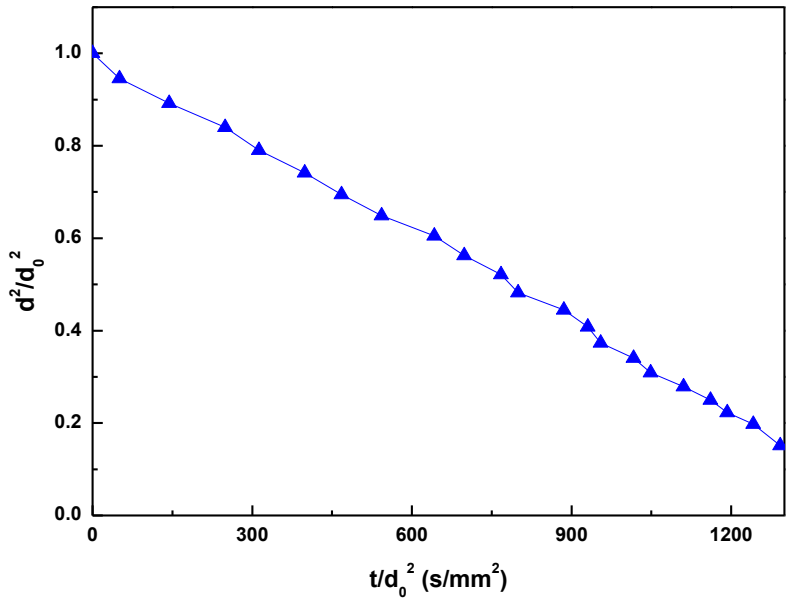

Figure 24 Droplet size history of a evaporating micro water droplet

CHAPTER 3. THEORETICAL MODEL WITHOUT INTERNAL CONVECTION

This chapter aims to develop a novel model to describe the evaporation of the droplets containing particles. The governing equations of the heat and mass transfer mechanism are based on evaporation of pure liquid. The effect of accumulation of solid particles at the droplet surface in the first stage is considered. The model is validated through published experimental data. Then the effects of Peclet number, initial particle concentration, and particle properties, such as wettability, on the evaporation process are discussed.

3.1 Theoretical model

3.1.1 Evaporation stages

As it has been described in Chapter 1, from the droplet morphological point of view, the evaporation process consists of two stages. During the first evaporation stage, the liquid evaporates from a free liquid surface. The evaporation rate can be assumed to be the same as that for a pure liquid droplet until the droplet surface is populated with solid particles. The pure liquid-like evaporation is followed by formation of the clusters of particles (i.e., solid crust), beginning with the appearance of particle aggregates until the droplet surface is completely covered by the crust, which can be considered as rigid. In the second evaporation stage, the liquid-vapor interface retreats to the inside of the crust. Evaporation would then occur when the liquid from within the crust reaches the crust through capillary action until complete evaporation is achieved.

The transition from the first evaporation stage to the second evaporation stage is quantitatively defined by the minimum liquid concentration or maximum solid concentration. The present work is focused on the detailed modeling during the first evaporation stage.

3.1.2 Heat and mass transfer at the droplet surface

Consider a droplet containing insoluble spherical particles. The particle size can be either micro or nano sized. Assume that the particles are initially evenly distributed within the droplet, as shown in Figure 25 (phase (i)). As the liquid evaporates, some particles from the evaporated volume are "trapped" at the droplet surface ("inclusion" as described in Derkachov et al. (2008) and phase (ii) in Figure 25). The particles on the surface will be partly immersed in the liquid (Yarin et al., 2002) and the exposed area of these trapped particles represent a reduction in the droplet surface from which liquid evaporates. The effective surface area for evaporation is denoted as A_e in Figure 25, while the nominal surface of the droplet is A_t (the total area). The enlarged view illustrating A_e is shown in the inset of Figure 25. Further evaporation and reduction of the droplet diameter lead to more gathering of particles on the surface. When the surface concentration of the particles reaches its maximum value, a shell of densely packed particles is formed at the droplet surface. (Sen et al., 2009). The saturated surface density corresponds to the neatly packed particles on the droplet surface (phase (iii) in Figure 25) and to the shell formation.

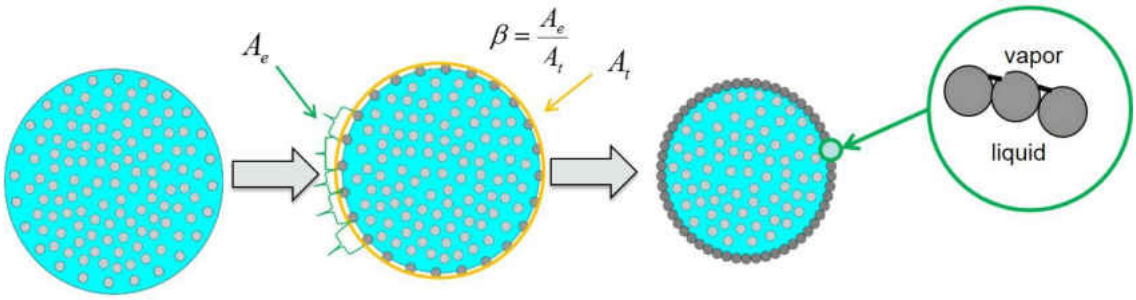

i ii iii

Figure 25 Evaporation of liquid suspension droplet

Since the size of the suspended particle is far smaller than the liquid droplet size of engineering interest, the effect of adsorbed particles on the fluid interface deformation is negligible and a nearly flat interface is reasonable approximation near the particle (Zeng et al., 2012). Therefore the shell is a layer of densely packed partially wetted particles. The evaporation front becomes a shell of particles containing the remaining solution inside of it and enclosing interstitial areas filled with liquid. The total of the interstitial area is thus A_e, which depends on the wettability of the particle that in turns depends on the contact angle of the particles in the liquid-air interface (Zeng et al., 2012).

For a single droplet in a non-convective atmosphere, the classical d^2-law assumes quasi-steady evaporation and uniform and constant temperature throughout the droplet. Under these assumptions, the conservation of mass in the gas phase (i.e., the surrounding environment can be written as (Glassman et al., 2008)

$$4\pi r^2(\rho v)\left(\frac{dY}{dr}\right) = \frac{d}{dr}\left[4\pi r^2 \rho D\left(\frac{dY}{dr}\right)\right] \quad (3.1)$$

where v, Y, and D are, respectively, the gas velocity, the mass fraction of liquid vapor, and liquid vapor mass diffusion coefficient. Applying the boundary conditions at the surface, Eqn. (3. 1) becomes

$$\rho_l \mathrm{A}_t \dot{r}_s = \rho_s A_e v_s = \rho_s Y_s v_s A_e - \rho D \left(\frac{dY}{dr}\right)_s A_e \tag{3. 2}$$

Where ρ_l is the liquiddensity and $\dot{r}_s$ the rate of change of droplet radius, and the subscript s denotes conditions at the droplet surface. The definitions of A_t and A_e are shown in Figure 25. For the pure liquid droplet $\mathrm{A}_t = A_e$. Equation (3.2) states that the bulk mass flow rate ($\rho_s A_e v_s$) leaving the droplet surface equals to the amount of the liquid vapor that is being evaporated minus the amount of the liquid vapor that diffuses back to the surface. In Eqn. (3.2), $D\rho$ is constant for the equilibrium (i.e., $D\rho = D_s \rho_s$). It is known that the liquid vapor velocity, v_s, is related the surface vapor mass fraction by the following expression:

$$v_s = \frac{D\left(\frac{dY}{dr}\right)_s}{Y_s - 1} \tag{3. 3}$$

Where Y is the liquid vopor mass fraction and the subscript s denotes conditions at the droplet surface. Substituting Eqn. (3. 3) into Eqn. (3. 2) and rearranging yields

$$v_s = -\beta \frac{\rho_l}{\rho_s} \frac{dr_s}{dt} \tag{3. 4}$$

where $\beta = A_e / \mathrm{A}_t$.

Solving Eqn. (3. 3) and incorporating surface conditions leads to

$$\frac{r_s v_s}{D_s} = \ln \frac{Y_\infty - 1}{Y_s - 1} \tag{3. 5}$$

By combining Eqns. (3. 4) and (3. 5), the following relationship between droplet diameter and time can be found

$$\frac{dd^2}{dt} = -K' = -\frac{8\beta D_s \rho_s}{\rho_l} \ln \frac{Y_\infty - 1}{Y_s - 1} \tag{3. 6}$$

where K' is the effective evaporation rate constant. Comparing the pure liquid result for K

$$K = -\frac{8D_s\rho_s}{\rho_l}\ln\frac{Y_\infty - 1}{Y_s - 1} \quad (3.7)$$

one finds

$$\beta = K'/K = A_e/\mathrm{A}_t \quad (3.8)$$

A more detailed description of evaporation rate of the pure liquid is given Appendix A. Equation (3. 8) indicates that the effective evaporation rate from the droplet surface can be reduced due to accumulation of particles at the droplet surface. To determine β, the task becomes that of determining the rate of particle accumulation on the droplet surface, and thus A_e.

3.1.3 Solid- liquid interaction

The partially submerged particle on the droplet surface is shown in the schematic in Fig. 25. It can be seen that $A_e = \mathrm{A}_t - A_p$, where A_p is the droplet surface area occupied by all the particle at the surface. The area A_p is the product of area that occupied by a single particle (A_{sp}) and the surface particles number (N_s). Therefore,

$$A_p = N_s A_{sp} \quad (3.9)$$

With the nomenclature shown in Fig. 2, $A_{sp}$is expressed as

$$A_{sp} = \pi r^2 = \pi(r_p sin\phi)^2 \quad (3.10)$$

Geometric consideration of the angles shown in Fig. 2 reveals that

$$\phi = \theta + \varphi \quad (3.11)$$

where θ is the particle contact angle on the liquid-gas interface. As mentioned earlier, the deformation of the liquid surface at the contact region of particles much smaller than the

droplet is negligible and the liquid surface can be assumed to be flat (Zeng et al., 2008), resulting in $\varphi = 0$. Therefore

$$\phi = \theta \tag{3. 12}$$

Equation (3. 9) becomes

$$A_{sp} = \pi r^2 = \pi(r_p sin\,\theta)^2 \tag{3. 13}$$

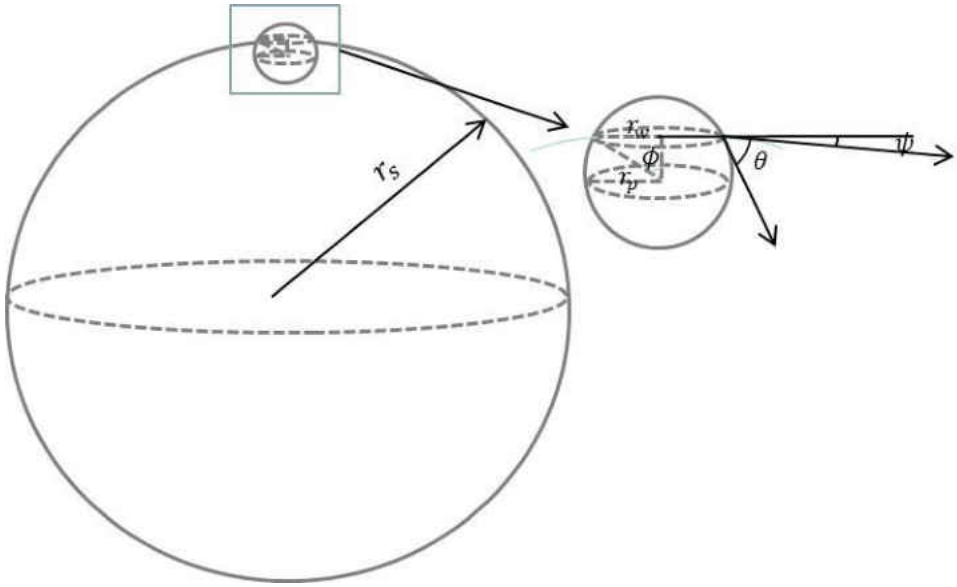

Figure 26. Side view of a single particle trapped at the liquid-gas interface

It is now desirable to determine N_s in Eqn. (3. 9) as a function of time. As droplet surface regresses, the particle concentration on and near the surface increases, while the concentration near the droplet center takes a longer time to adjust to the regression, resulting in a concentration gradient in the radial direction. To obtain the instant surface density (C_s), the particle number in the unit volume, Fick's second law of diffusion (Vehring et al., 2007) is adopted to account for the two competing process involved in the evaporation process—droplet receding and particles diffusion:

$$\frac{\partial C}{\partial t} = \frac{D_{pl}}{{r_s}^2}\left(\frac{\partial^2 C}{\partial R^2} + \frac{2\partial C}{R\partial R}\right) + \frac{R\partial C\partial r_s}{r_s \partial R \partial t} \tag{3. 14}$$

where C is the instantaneous concentration of solute as a function of time and location, D_{pl}, the diffusion coefficient of particles in the liquid phase, r_s, the droplet radius, and R, the normalized radial coordinate, $R = r/r_s$. The analytical solution of Eqn. (3. 14) is provided in Vehring et al. (2007) and Leong (1987), that is

$$C_s = C_m \frac{exp\left(\frac{K}{8D_{pl}} \cdot R^2/2\right)}{3\int_0^1 R^2 \exp(\frac{K}{8D_{pl}} \cdot R^2/2)dR} \tag{3. 15}$$

where C_s and C_m denote the volumetric particle concentration at the droplet surface and the volume-average particle concentration throughout the entire droplet. The average concentration is described as

$$C_m = C_0(\frac{d_0}{d})^3 \tag{3. 16}$$

where d_0 is the initial droplet diameter.

Equation 3.15 describes the surface particle concentration change in the evaporation process. The combined results of Eqns. (3. 15) and (3. 16) suggest that both C_s and C_m are functions of C_0 and d_0. The value of the term following C_m on the right-hand side of Eqn. (3. 15) depends on K/D_{pl}, which is essentially a Peclet discussed in the chapter 1. For simplification, Vehring et al. (2007) used $Pe \equiv K/8D_{pl}$ and the rest of this paper adopt this definition. Thus

$$C_s = C_m \frac{exp(Pe \cdot R^2/2)}{3\int_0^1 R^2 \exp(Pe \cdot R^2/2) dR} = C_o \left(\frac{d_o}{d}\right)^3 \frac{exp(Pe \cdot R^2/2)}{3\int_0^1 R^2 \exp(Pe \cdot R^2/2) dR} \quad (3.17)$$

Where $E = \frac{exp(Pe \cdot R^2/2)}{3\int_0^1 R^2 \exp(Pe \cdot R^2/2) dR}$, C_o and d_o are the initial particle concentration and initial droplet diameter, respectively. With C_s known, N_s can be obtained for a given r_p by accounting the particles number in the control volume where the first layer particles reside. The thickness of the first layer particles is δ, and as an approximation $\delta = d_p$. Therefore,

$$N_s = C_s(\pi d^2 \delta) = \pi C_s d^2 \delta \quad (3.18)$$

By incorporating Eqns. (3. 8), (3. 9), (3. 13), and (3. 18), one finds

$$\beta = \frac{A_t - A_p}{A_t} = 1 - \frac{N_s A_{sp}}{A_t} = 1 - C_s \alpha \left(\frac{\pi d_p^3}{4}\right) = 1 - \frac{\alpha d_p^3 E}{4} C_o \left(\frac{d_o}{d}\right)^3 \quad (3.19)$$

where $\alpha = sin^2\theta$. Combine equations (3. 6) and (3. 18), the evaporation rate of droplet containing insoluble particles, K', is written as

$$K' = \beta K = K\left(1 - \frac{\alpha d_p^3 E}{4} C_o \left(\frac{d_o}{d}\right)^3\right) \quad (3.20)$$

The results of Eqns. (3. 19) and (3. 20) suggest that the effective surface area and the evaporation both decrease with C_s and d_p, as expected. Equation (3. 18) indicates that the value of C_s depends on Pe and C_m, with the latter being a function of time.

The solutions for β and K' involve an iterative procedure for K' (so that C_m in Eqn. (3. 16) can be calculated as a function of time) and C_s. The initial step assumes that $K' = K$ (i.e. $C_s = 0$). Then C_m (and R) in Eqn. (3. 16), or d in Eqns. (3. 18) and (3. 19) are calculated as functions of time; it is clear that C_m, R, and d are related. The values in turn lead to C_s in Eqn. (3. 17) or, directly, to a new value of K', thus completing the iteration.

The parameter α depends on the contact angle, θ, the liquid-particle pair. Judging from the fact that K' decreases with time (Chen et al., 2010; Gan et al., 2011), it is expected that the particle at the droplet surface is not entirely covered by the liquid, leaving part of the particle surface dry and exposed to the surrounding gas phase environment. It is for this reason of the exposed dry particle surface that $K' < K$ and increasingly so as more particles gather on the droplet surface. The partially dry and exposed particle surface suggests that $\theta > 0$ during the evaporation; otherwise $\theta = 0$ would mean total immersion of the particle in the liquid. Combining the colloidal stability (with or without the aid of surfactant) requirement, $0 < \theta < \pi/2$ and the true angle is more likely to be on the smaller side of this range. During the evaporation process (which is non-equilibrium), the value of θ is not fixed, much like during receding process of a sessile droplet. Another complicating factor is that, to these authors' knowledge, no contact angle has been determined on a solid surface with nano-scales. In this study, the contact angle is assumed to be constant throughout the evaporation process; For example, for aluminum nanoparticle-ethanol nanofluid, the known macroscopic value of $\theta = 40^o$ is used (along with values for other solid-liquid pairs) unless the value is provided otherwise.

3.2 Model Validation

The model is validated by comparing the prediction of droplet size history with the literature data for the same physical process. The detailed information about the experiment is provided in Table 1. In the model, the evaporation rate of pure liquid (K) is needed. The model will adopt the evaporation rate of pure liquid if the value is given, otherwise, it will use the evaporation rate of the liquid suspension at the beginning of the evaporation process.

The details and values of relevant parameters are given in Table 1 for the experimental results used for validating the present model.

3.2.1 Comparison with Derkachov et al. (2008)

Derkachov et al. (2008) used electrodynamic trap construction to study the evaporation of nanofluid by levitating a droplet. The experiment was performed at a temperature of 15 ± 0.3℃, environmental pressure of 1006 kPa and environmental water vapor relative humidity of 94%. The droplet has the initial diameter of 26 μm and the initial volume fraction of polystyrene spheres was around 0.1%. The size of the suspended particles was 200 nm. The detailed parametric values are given in Table 1.

Figure 27 shows the droplet size evolution process of the water droplet containing PS particles. The figure shows that the model agrees well with the experimental result in the first evaporation stage. As discussed in section 3.1, $K' = \beta K$. Therefore, $K$is constant for the isothermal evaporation, and the change of K' is caused by the change of β. The β plot shows little change before 10 s, then a remarkable drop, demonstrating a change from the first stage to the second stage at around 10 s (14793 s/mm^2 in Figure 27). The Peclet number for the experimental condition is 3.2 (shown in Table 1). The small change of evaporation rate in the first evaporation stage can be explained by the Peclet number. For small Peclect numbers ($Pe\sim1$), the value of E is around 1. The particles have enough time to redistribute inside the droplet. Therefore, there is little difference in the concentrations between within the droplet and on the surface, which means that the particles have enough time to redistribute inside the droplet. The small change of β in the first stage shows that the particle number at the

droplet is small. The evaporation is similar to that of pure liquid. Figure 27 shows the evaporation rate reduces by 10% by the end of first stage.

3.2.2 Comparison with Gan et al. (2011)

Gan et al. (2011) used the pendant droplet approach to study the evaporation characteristics of ethanl droplets containing nano Al particles. Figure 28 shows the comparison of size history of an ethanol droplet with 2.5 wt.% nano-Al under natural convection at 300K. It is worth noting that if the model applies the Peclet number that is calculated from the experimental parameters (68), the droplet size (d^*) when the shell forms is bigger than the experimental observation. With equation 3.17, d^* is expressed as

$$\frac{d^*}{d_0} = \left(\frac{c_0 E}{c_s^*}\right)^{1/3} \tag{3.21}$$

where $C_s{}^*$ is the surface particle concentration when the shell is formed. For a Peclet number of 68, d^* is 0.66 mm. But, the experimental observation traces the droplet diameter down to smaller droplet size, around 0.5 mm. The difference between the experiment and the model predictions can be explained by the Peclet number. In the model, the value of D_{pl} is derived from the Einstein Stokes relation, in which internal flow is not taken into account. As discussed in Chapter 1, for pendant droplets, the internal circulation is a major factor that affects the heat and mass transfer of the evaporation process. The internal convective flow results in enhancement of the mass diffusion coefficient. For vigorous internal circulation involved in the acoustic levitation system, the mass diffusivity can be enhanced by 6 orders of magnitude (Nesic et al., 1991). For pendant droplets at natural convection conditions, the internal flow is moderate. Therefore, the enhancement of mass diffusivity is small. In this work, the mass diffusivity is modified in the model until the prediction of droplet size history

agrees with the experimental data. The comparison with the experimental data shows good agreement at around $Pe = 30$, in which the value of D_{pl} is enhanced by two times.

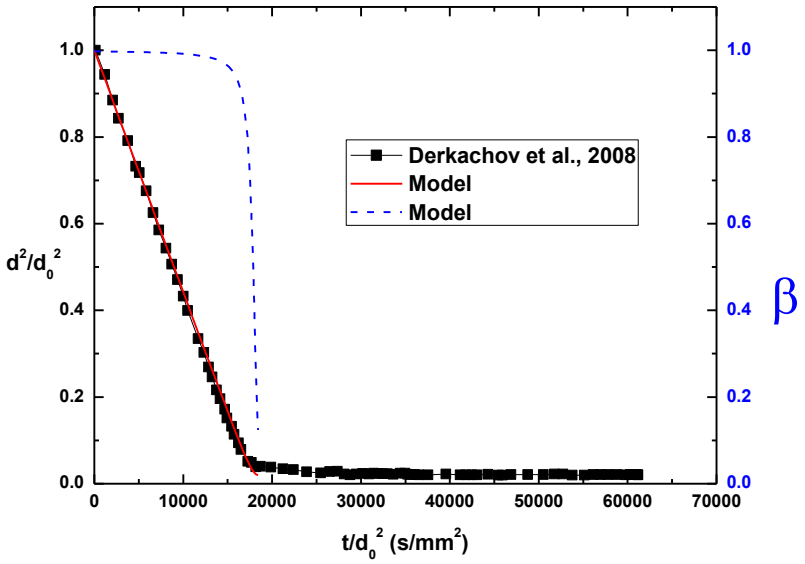

Figure 27 Evaporation of water droplet with 0.1% nano-polystyrene particles

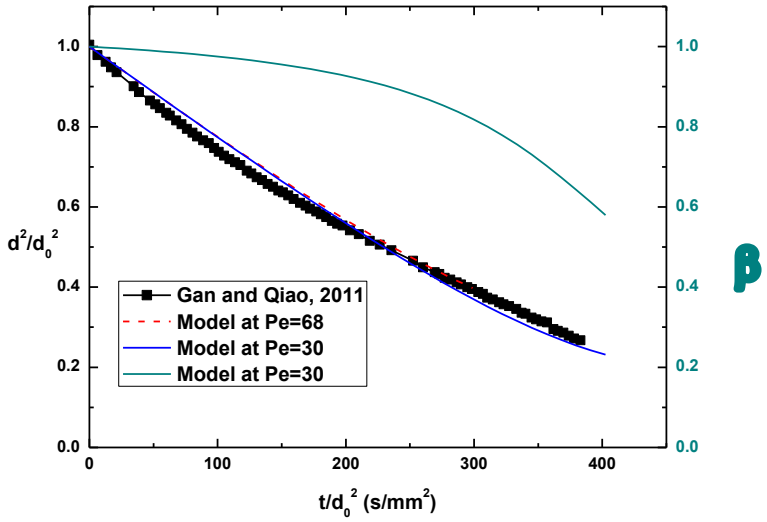

Figure 28 Evaporation of ethanol droplets containing 2.5 % nano-Al under natural convection at 300K

The model is also applied to predict the evaporation of liquid suspension under weak forced convections. The internal circulation is more vigorous when the droplet is surrounded by gas flow, leading to a bigger discrepancy of mass diffusion coefficient. Table 2 shows the prediction of d^* based on experiment parameters and the final droplet size it can reach, respectively. It shows that d^* is overestimated under the weak forced convection. For the weak forced convection at 330 and 380 K, the predicted droplet size at the end of the first evaporation stage is reduced by 10%, while experiments show that the droplet size can reduce to 50% of initial size. To account for the effect of internal circulation on the particle transport, the mass diffusivity is modified. Since studies on mass transfer coefficient in the pendant droplet are rare, the mass diffusivity is modified to fit the experimental curve in this work. A Peclet number is pre-assumed until the model agrees with the experimental droplet size history. Table 2 shows that the Peclet number is around 1 under forced convection at higher temperatures (330 K and 380 K).

Figure 29 shows comparison of droplet size histories of evaporating ethanol droplets containing 2.5 wt.% nano aluminum under various temperatures. The model predictions show that for natural convection, the evaporation deviates from the classical d^2-law. For evaporations at weak forced convections, it shows the evaporation behavior of pure liquid droplets, which is consistent with experimental observations. It is worth noting that experimental data only provides the droplet size down to 50%. The stabilization of droplet size may be caused by either the termination of the first evaporation stage, at which the droplet forms a crust and liquid vapor diffuses through inter particle space, or the distortion of the droplet involved in the pendant droplet approach. However, there is no explanation for the termination of experiment at 50% of initial size in Gan et al. (2011). The model

predicts the size histories in the first evaporation stage and shows that the values of d^* are different under various gas temperatures. The droplet sizes at the end of the first evaporation stage are smaller than in the experiments.

The model is supported by Gan et al. (2011), while the reason for the change of evaporation rate during the evaporation of liquid suspension under natural convection conditions is still not clear. Figure 30 shows the evolution of evaporation rate of liquid suspension at different temperatures based on the model. The two axis are dimensionless. The horizontal axis is the ratio of time to lifetime of the first stage. The β (K/K') plots show a gradual decrease of evaporation rate in the first evaporation stage in all the cases. The decrease of evaporation rate at larger Peclet number is faster than at lower. For a higher Peclet number, the evaporation rate starts to decrease at the beginning of the evaporation process. It is worth noting that the reduction of evaporation rate in the first evaporation stage is the same for all the cases. It can be explained from the expression of β

$$\beta = 1 - C_s \alpha \left(\frac{\pi d_p^3}{4}\right) \tag{3.22}$$

Since the solid volume fraction is

$$Y_V = C_s \left(\frac{\pi d_p^3}{4}\right) \tag{3.23}$$

The evaporation rate ratio at the end of the first evaporation stage $\beta^*$is rewritten as

$$\beta^* = 1 - {Y_V}^* \alpha = 1 - {Y_V}^* (sin\theta)^2 \tag{3.24}$$

In this model, the termination of the first evaporation stage is defined by the maximum solid volume fraction, which is ${Y_V}^* = 0.6$. β^* is determined by the contact angle. As explained before, for all the cases discussed above, the contact angle is made to be 40° unless the experimental data is given otherwise. The same contact angle leads to the same

reduction of evaporation rate by the end of the first evaporation stage. It can also be concluded form equation 3. 24 that for solid particles that have larger contact angles, the decrease of evaporation rate in the first evaporation stage is larger.

Table 1. Parameters used for the validation of analytical model, where * denotes application of Einstein- Stokes correlation, # denotes the Peclet number based on experiment

Investigators	Experimental conditions	Base fluid	Initial droplet size	Particles	Particle size (μm)	Concentration* ($/m^3$)	Contact angle θ (°)	D_{pl}^{*} (m^2/s)	Evaporation rate K (m^2/s)	Pe#
Derkachov et al. (2008)	EDB	Water	26 μm	Polystyrene	0.2	2.39×10^{17}	73	2.2×10^{-12}	5.65×10^{-11}	3.2
Gan and Qiao, (2011)	Pendant droplet NC 300K	Ethanol	1 mm	Al	0.08	2.76×10^{19}	40	5.49×10^{-12}	3×10^{-9}	68
Gan and Qiao, (2011)	Pendant droplet WC 300K	Ethanol	1 mm	Al	0.08	2.76×10^{19}	40	5.49×10^{-12}	9.5×10^{-9}	216
Gan and Qiao, (2011)	Pendant droplet WC 330K	Ethanol	1 mm	Al	0.08	2.76×10^{19}	40	9.39×10^{-12}	1.62×10^{-8}	216
Gan and Qiao, (2011)	Pendant droplet WC 380K	Ethanol	1 mm	Al	0.08	2.76×10^{19}	40	2.32×10^{-11}	3.52×10^{-8}	190
Mezhericher et al. (2012)	Acoustic levitated At 15°C	Water	1.5 mm	silica	0.2	4.58×10^{17}	40	2.2×10^{-12}	1.09×10^{-9}	61.9

Table 2 Comparison of droplet size at the end of first evaporation stage

Experimental conditions	Temperature (K)	Prediction of d^* based on exp.		Prediction of d^* based on end of exp.	
		Pe	d^* (mm)	Pe	d^* (mm)
Natural convection	300	68	0.66	30	0.48
Weak forced convection	300	198	0.89	25	0.46
Weak forced convection	330	216	0.94	3	0.27
Weak forced convection	380	246	0.96	1	0.24

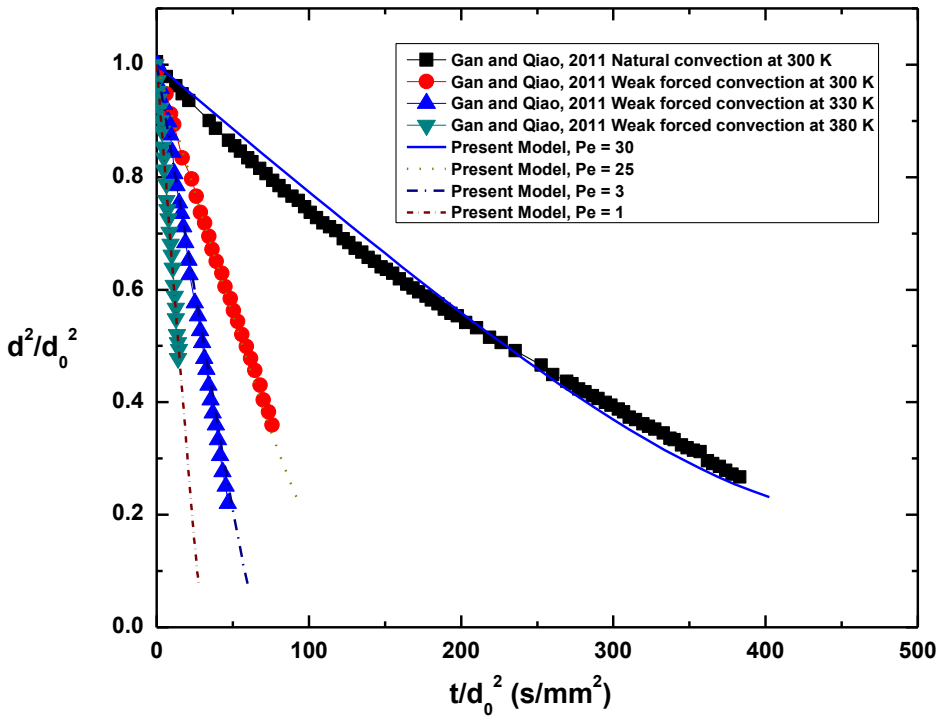

Figure 29 Droplet size history of ethanol droplets containing 2.5% nano- aluminum particles under various temperatures

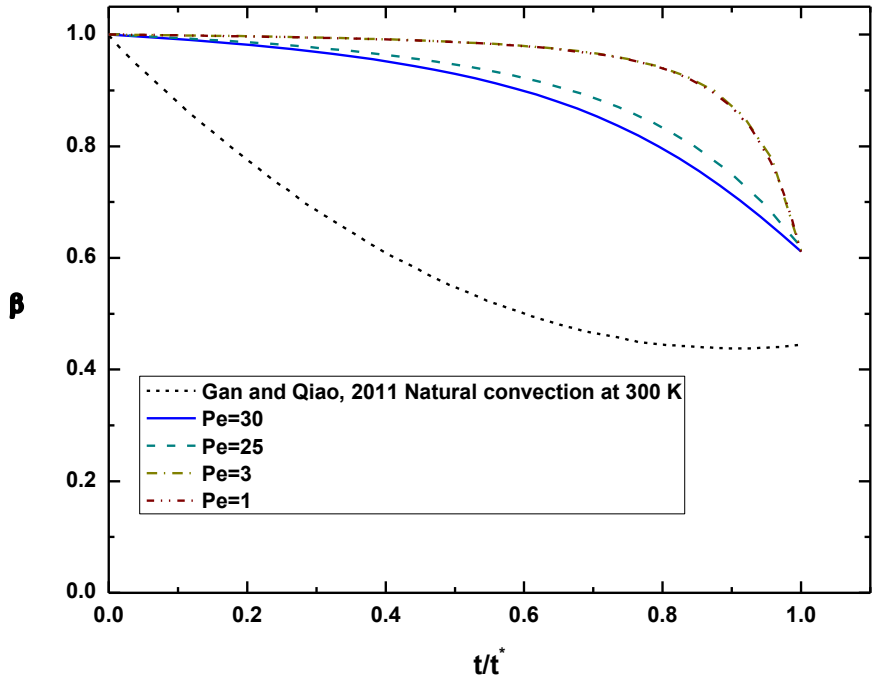

Figure 30 Evaporation rate of ethanol droplets containing 2.5 wt.% nano aluminum particles under forced convection

3.2.3 Comparison with Mezhericher et al. (2012)

Mezhericher et al. (2012) used the acoustic levitation approach to study the evaporation of droplets containing nano silica particles. Figure 31 shows the comparison of droplet size history during the evaporation process with the various theoretical models, continuous species transport model (CST), population balance approach (PB) and our model. CST considers the external heat and mass transfer between the droplet and surrounding gas, and intra-droplet suspended particles diffusion. The population balance model takes into account the particle growth and aggregation phenomena of suspended particles.

In the CST method, the first e stage is divided into two morphologically different periods: before shell formation and the transition period after shell formation. In the "before

shell formation" period, the liquid vapor diffuses through the liquid surface until the solid concentration reaches saturation value, at which point, a shell is formed and the transition period begins. In the transition period after the shell formation, the shell thickens because of the continuous evaporation of liquid. The model considers that in this period the thickening shell is always submerged within the droplet and the liquid can still freely evaporate from the droplet surface. Therefore, the model considers that the evaporation in such a period still obeys the d^2 –law, and the evaporation rate is constant through the first evaporation stage. The termination of the first evaporation stage is determined when the capillary compression is balanced by the shell strength.

In the PB method, the dispersed solid phase is described by particle number density. The model considers the diffusion of particles. The end of the first evaporation stage is defined by the saturation of particles on the surface, which is similar to our model.

It is notable that in the CST and PB, the diffusion coefficients are modified by taking into account the vigorous liquid circulation involved in the acoustic levitation system (Yarin et al., 1999; Nesic et al., 1991; Mezhericher et al., 2012). D_{pl} is enhanced by 6 orders of magnitude, from 10^{-12} m^2/s, as obtained through Einstein-Stokes relation, to 10^{-6} m^2/s. In Mezhericher et al.'s CST model, the particle diffusion coefficient D_{pl} is a function of particle concentration. In our model, D_{pl} is simplified to be constant (10^{-6} m^2/s). It is reasonable to make such a simplification because during the evaporation process the maximum solid volume fraction in the droplet varies from initial value to saturation (D_{pl} ranges from 10^{-6} to 3×10^{-9} m^2/s). [2]. Pe is far smaller than 1 (Pe varies from 1.4×10^{-4} to 4.67×10^{-2}). For $Pe \ll 1$, E is 1. In such conditions, the effect of concentration change on the mass diffusivity is negligible.

For $Pe \ll 1$, the particles have sufficient time to redistribute within the droplet, so the surface concentration of particles is nearly the same as the average value. The accumulation of particles on the droplet surface is minor. The effect of particles on the evaporation rate of droplets in the first evaporation stage is small. The evaporation of droplets containing particles can be regarded as that of pure liquid, which is captured by CST, PB and our model, as shown in Figure 31. The predictions of droplet size history agree well with the experiment. It is notable that, compared to CST and PB, our model gives a shorter duration of the first evaporation stage, which is closer to the experimental observation.

As discussed in section 3.1, since the contact angle of nano particles at the liquid surface is unknown, the model adopts a general value, 40°. The study of the effect of contact angle on evaporation behavior is listed in Table 3. It shows that the droplet size when the first evaporation stage ends is 0.5 mm for all the contact angles. The ratio of evaporation rate to that of pure liquid decreases as contact angle decreases. If the contact angle is 10°, the evaporation rate at the end of the first stage is 98% of the pure liquid. In such case, the evaporation process in the first evaporation stage is the same as that of pure liquid.

Figure 31 also shows the size history and β plots under various contact angles. The figure shows that for a specific Peclet number, the droplet size at the end of first evaporation stage is the same. The evaporation duration time decreases as the contact angle decreases. It can be explained from the average evaporation rate in the first evaporation stage. Since the droplet size change is the same for all the cases, the effect of evaporation rate is determined by the contact angle. For the higher contact angle case, the reduction of evaporation rate in the first evaporation stage is larger, due to the more surface area that is

blocked by particles. Therefore the average evaporation rate is lower for higher contact angle, leading to the same size change in the first stage.

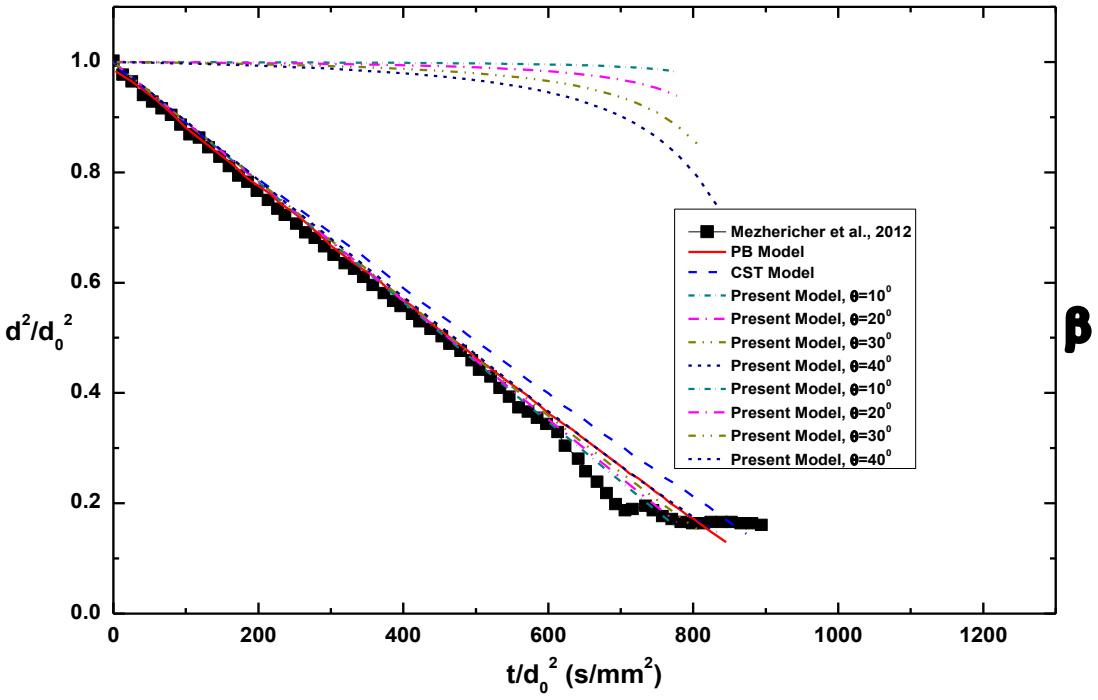

Figure 31 Comparison between the experiment and various models

Table 3 The evaporation constant and droplet size at the end of first evaporation stage as a function of contact angle

Θ (°)	ß*	d*(mm)
10	0.98	0.5
20	0.924	0.5
30	0.838	0.5
40	0.732	0.5

3.3 Discussion

A novel model has been developed to investigate the effect of particles on the evaporation of liquid suspension in the first evaporation stage. The model is validated by the published experimental data. As shown in equation (3. 20), the evaporation rate is rewritten as

$$K' = f(Pe, C_0, \alpha) = f(Pe, C_0, \theta) \quad (3.25)$$

The evaporation rate in the first evaporation stage is determined by three factors, Peclet number, initial particle concentration and particle contact angle. Next we will discuss their effects on the evaporation behavior of droplet containing particles, which includes duration time of first evaporation period t^*, $d^*$and evaporation rate. The study case for the discussion is a single free standing water droplet containing Aluminum nanoparticles. The droplet has the initial size of 1 mm and the evaporation rate of pure liquid is 10^{-9} m^2/s. The size of Al-nanoparticles is 100 nm. The contact angle is 40 °.

3.3.1 Effect of Peclet number on the evaporation of droplet containing particles

Figure 32 shows the β plots as a function of *Pe*. The initial particle volume fraction is 1%. As the evaporation rate constant,$K' = K\beta$, the β shows the change of evaporation rate constant. Initially the evaporation rate constant equals the evaporation rate constant of pure liquid, K. As evaporation proceeds, the evaporation rate constant gradually decreases. For small Peclet number, the particles diffusion rate is large. The particles have enough time to redistribute. The decrease of evaporation rate constant is slower. As Pe increases, more particles are trapped at the droplet surface due to the higher droplet recession rate, the decreases of evaporation rate constant is accelerated. It is noted that the reduction of evaporation rate constant in the first stage is the same for all the Pe numbers, which will be explained in section 3.3.3.

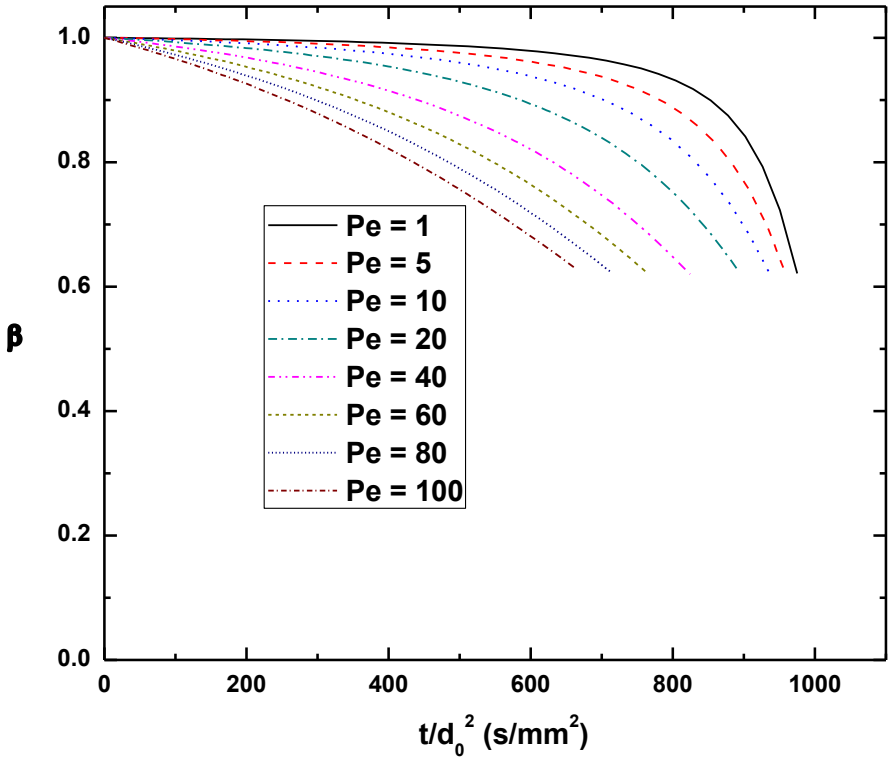

Figure 32 β plots as a function of *Pe*

In the expression of evaporation rate (eqn. 3. 20), the term related to Peclet is

$$E = \frac{exp(Pe/2)}{3\int_0^1 R^2 \exp(Pe \cdot R^2/2) dR} \tag{3.26}$$

The plot in Figure 33 shows that E is proportional to *Pe*. E is valid for Pe <1400. For Peclet number larger than 10, the correlation between E and *Pe* is simplified as

$$E = \frac{Pe}{3} \tag{3. 27}$$

The droplet size at the end of first evaporation stage in equation 3.21 is rewritten as

$$\frac{d^*}{d_0} = \left(\frac{c_0 E}{c_s^*}\right)^{1/3} = \left(\frac{c_0 Pe}{3c_s^*}\right)^{1/3} \tag{3. 28}$$

Figure 34 shows the size of the dry particle as the function of Peclet number under various initial particle volume fractions. The figure shows that the size increases as Peclet

number increases. For larger Peclet number, the particles diffusion velocity is smaller than the droplet shrinking velocity. As evaporation proceeds, more and more particles will be trapped on the surface. For the same initial particle concentration, the time for particles getting saturated is shorter than at smaller Peclet number, leading to smaller reduction of droplet size. Figure 34 also shows that the particle size at lower particle concentration is smaller at the same Peclet number condition.

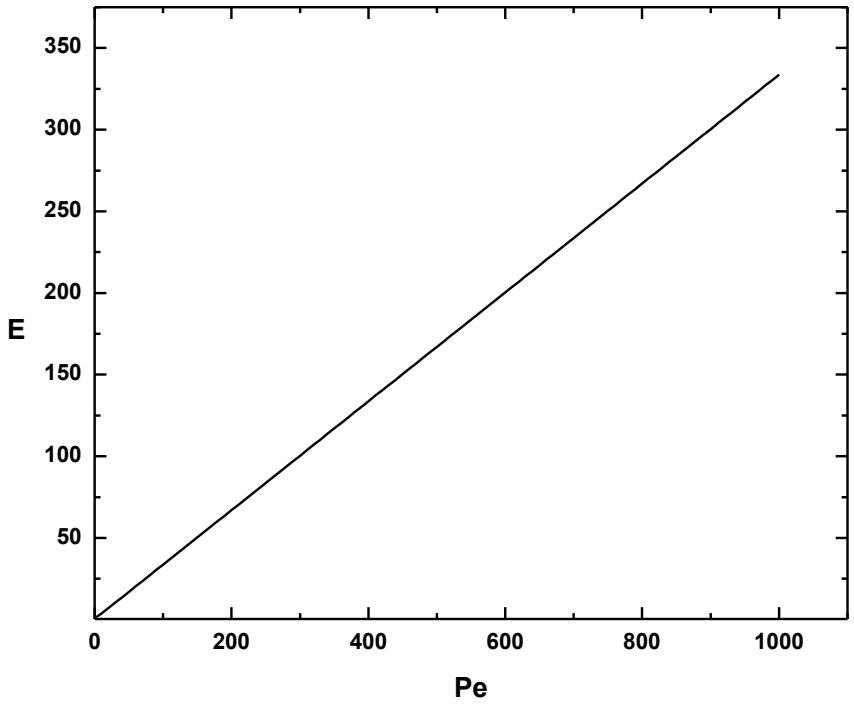

Figure 33 E vs. Pe correlation

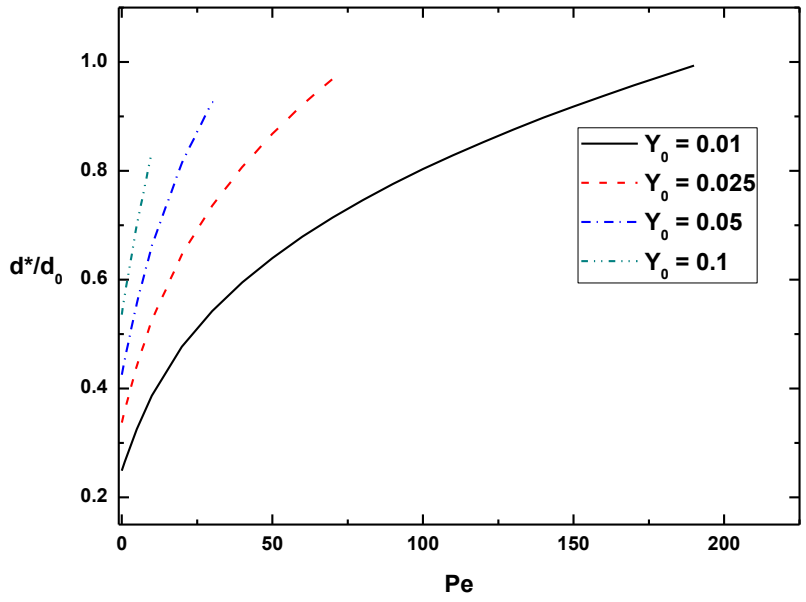

Figure 34 The droplet size at the end of the first evaporation stage as a function of Peclet numbers under various initial particle volume fractions

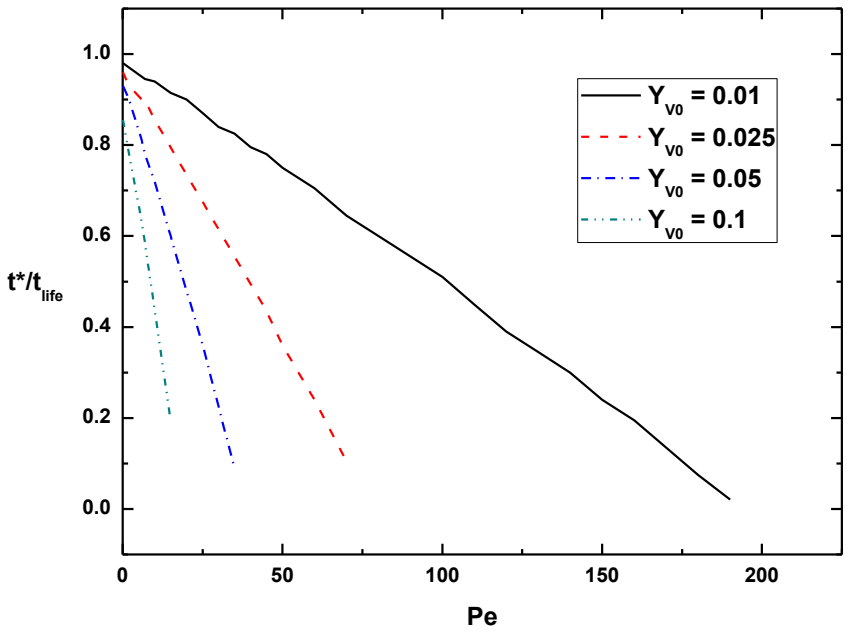

Figure 35 The duration time of first evaporation stage as a function of Peclet numbers under various initial particle volume fractions.

Figure 35 shows the duration of first evaporation stage (t^*) as a function of Peclet number under various initial particle conditions. The vertical axis is the ratio of t^* to the lifetime of a pure liquid droplet with the same initial size and evaporation rate($t_{life} = \frac{d_0^2}{K}$). Figure 35 shows that for the same Peclet number condition t^* is larger at lower initial particle concentration than at higher particle concentration and decreases as particle concentration increases. Since the particle concentration at the end of the first evaporation stage is fixed, at which the particles could not compact anymore. For the same Peclet number, it needs more time to reach saturation at lower initial particle concentration. At the same initial particle concentration, the duration time of the first evaporation stage decreases as Peclet number increases due to the higher droplet receding velocity compared to particles diffusion velocity.

3.3.2 Effect of initial particle concentration on evaporation

This section aims to study the effect of initial particle concentration on the evaporation process in the first evaporation stage. Figures 36 shows the droplet size histories of aqueous suspension droplet with the initial particles volume fractions of 1%, 2.5%, 5% and 10% under a wide range of Peclet numbers, 0.1~1000. The figure shows that for small Peclet number condition (Pe = 0.1), the evaporation of aqueous droplet behaves similar to that of pure liquid. The evaporation gradually deviates from the classic d^2-law as particle concentration increases. For the initial particle volume fraction of 10%, the deviation starts from the beginning of the evaporation process. For the homogeneous liquid suspension, at

the beginning of the evaporation process, there are particles residing on the droplet surface. The surface particles decreases the effective liquid surface area. For smaller initial particle concentration, the particle number is low. The effect of particles on the evaporation is insignificant. While as initial particle concentration increases, the higher particle number density on the droplet surface reduces the effective area for the liquid vapor. The effect of particles on the evaporation is significant at the beginning of the evaporation.

It is worth noting that at larger Peclet number condition, the evaporation of droplet under relative bigger particle concentration could not be plotted. The first evaporation stage terminates quickly after the evaporation starts. For Peclet number of 50, the evaporation stops near the beginning of evaporation under the initial volume fraction of 10%. The initial particle concentration that results in quick termination of first evaporation stage decreases as Peclet number increases. For Peclet number of 100, the first evaporation stage is negligible at the particle volume fraction of 5%. For Peclet number of 1000, the first evaporation stage can proceed under 1%. The reason for such phenomena lies in the competing transport processes involved in the evaporation process: droplet shrinking and particles diffusion. For larger Peclet number conditions, the droplet shrinking velocity is bigger than particle diffusion velocity. More and more particles are trapped on the surface until the surface particles get saturated. The saturation of surface particles can be further pushed to earlier time by enhancing particle concentration. There is a criteria that when the particle concentration reaches a limit value that the surface particles get saturated at the beginning of the evaporation process.

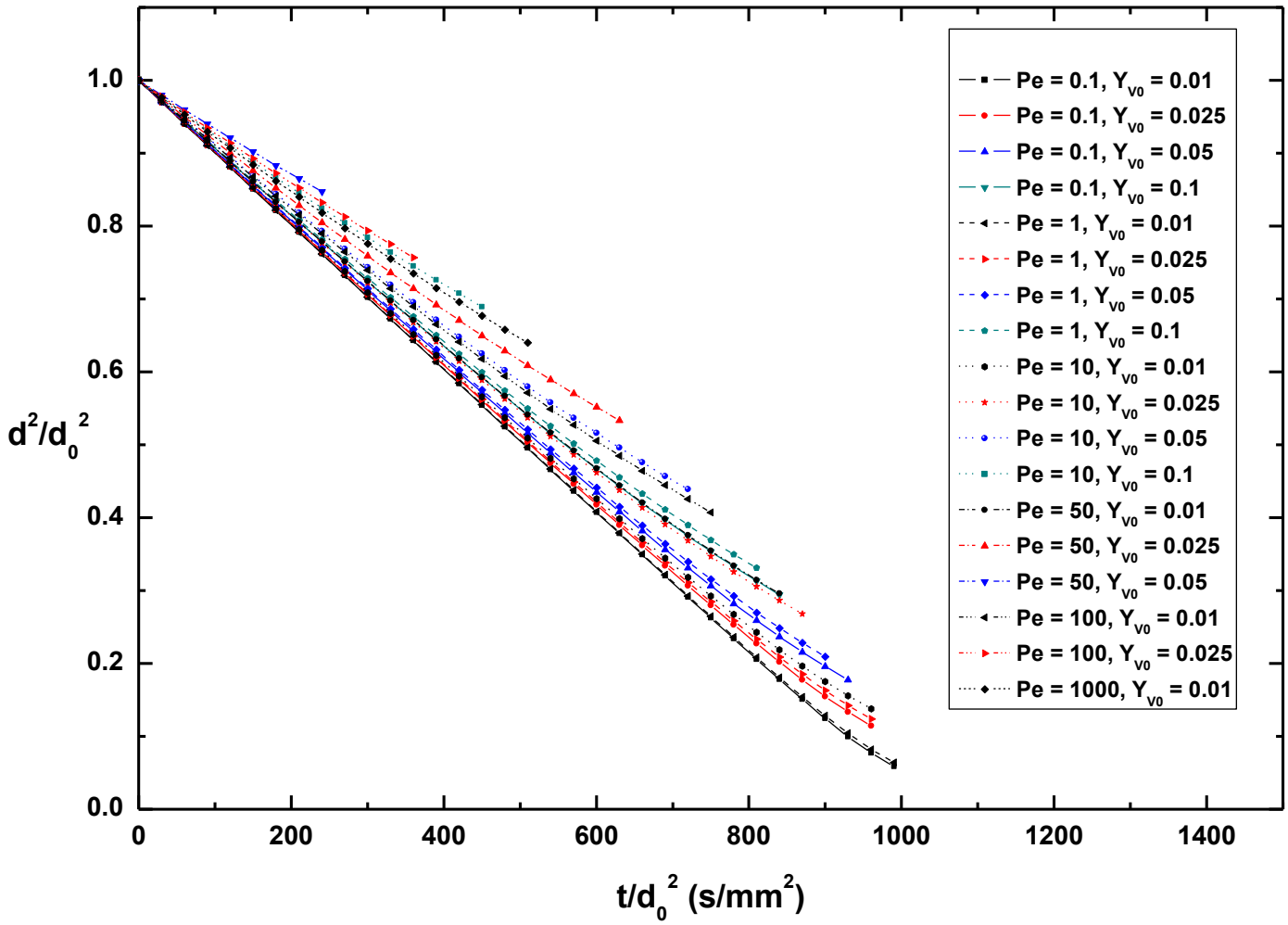

Figure 36 Evaporation process of aqueous suspension at various particle concentrations under different Peclet number

To get the criteria for the relation between Peclet number and initial particle volume fraction, we adopt expression of droplet size d^* at the end of first evaporation stage from equation 3.21 and rewritten the equation as a function of particle volume fraction

$$\frac{d^*}{d_0} = \left(\frac{Y_{V0}E}{Y_{Vs}^*}\right)^{1/3} \tag{3.29}$$

For $Y_{Vs}^* = 0.6$ and droplet size at the end of first evaporation stage does not exceed initial droplet size (${}^{d^*}/_{d_0} \ll 1$), we have

$$Y_{V0}E \ll Y_{Vs}^* \tag{3.30}$$

From equation 3.27, then

$$Y_{V0}E = \frac{Y_{V0}Pe}{3} \ll 0.6 \tag{3.31}$$

The criteria to allow droplet shrinking process in the first evaporation stage is

$$Y_{V0}Pe \ll 1.8 \tag{3.32}$$

To allow droplet shrinking process in the first evaporation stage, the product of initial particle volume fraction and Pe should be smaller than 1.8, otherwise the first stage terminates at the beginning of the first evaporation stage and the size of final dry particle is the same as initial droplet size.

The criteria is applied to verify the study cases in Figure 37. Table 4 lists the evaporation cases under different initial particles volume fraction and Peclet numbers. For the small Peclet numbers and small initial concentration cases, the evaporation of the first evaporation stage can proceed. While for large Peclet number and large initial particles concentration, the evaporation directly switches to the second evaporation stage due to the particles saturation at the beginning of the first

evaporation stage. The study cases that could not be shown in figure 37 are due to the termination of first evaporation stage at the beginning of the evaporation process, in which $Y_{V0}Pe > 1.8$

Table 4 The validation of the study cases shown in Figure 36

Pe	c_0	c_0Pe	Plots of evaporation in the first evaporation stage
0.1	0.01	0.001	√
0.1	0.025	0.0025	√
0.1	0.05	0.005	√
0.1	0.1	0.01	√
1	0.01	0.01	√
1	0.025	0.025	√
1	0.05	0.05	√
1	0.1	0.1	√
5	0.01	0.05	√
5	0.025	0.125	√
5	0.05	0.25	√
5	0.1	0.5	√
10	0.01	0.1	√
10	0.025	0.25	√
10	0.05	0.5	√
10	0.1	1	√
30	0.01	0.3	√
30	0.025	0.75	√
30	0.05	1.5	√
30	0.1	3	×
50	0.01	0.5	√
50	0.025	1.25	√
50	0.05	2.5	×
50	0.1	5	×
100	0.01	1	√
100	0.025	2.5	×
100	0.05	5	×
100	0.1	10	×
1000	0.01	10	×
1000	0.025	25	×
1000	0.05	50	×
1000	0.1	100	×

Figure 37 shows the criteria for allowing proceeding of first evaporation stage. Y_{cV0} is the critical initial particle volume fraction. The configuration of initial particle volume fraction and Peclet number conditions should be performed below the critic line to allow droplet shrinking process. For evaporation process performed at higher Peclet number condition, the initial particle concentration should be controlled in a lower level to allow droplet shrinking before shell formation.

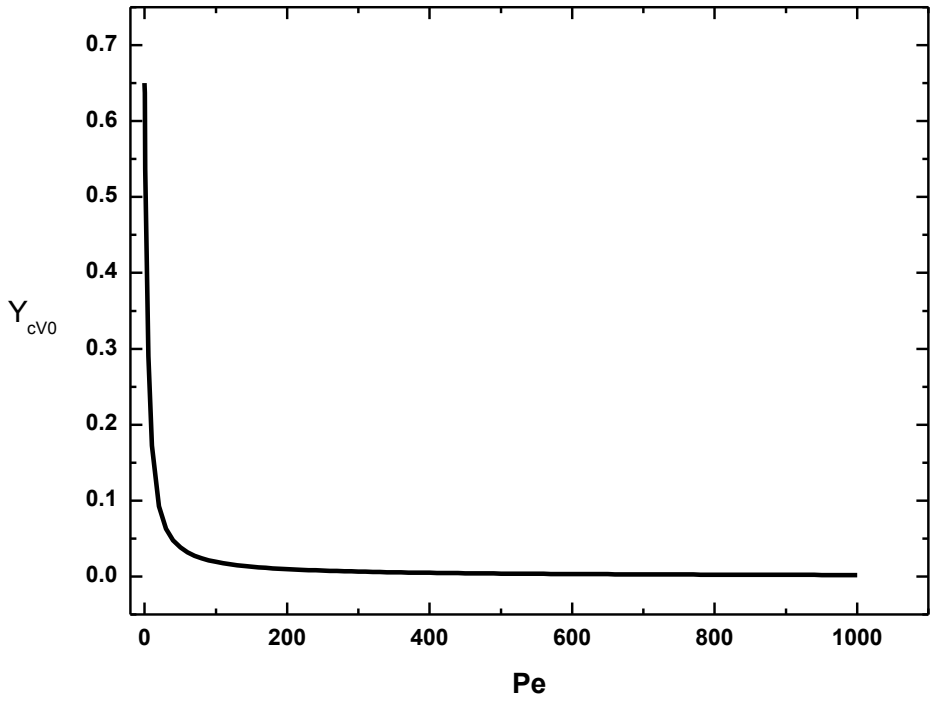

Figure 37 The criteria for allowing droplet shrinkage in the first evaporation stage

3.3.3 Effect of contact angle on evaporation in the first evaporation stage

As discussed before the contact angle of nano particles at the liquid surface is nowhere to obtain, we adopt a general contact angle, 40°. In our model, the contact angle is a major factor that affects the evaporation rate of droplet containing particles at the end of the first evaporation stage.

$$\beta^* = 1 - \frac{3\alpha {Y_S}^*}{2} = 1 - \frac{3sin^2\theta {Y_S}^*}{2} \tag{3.33}$$

For the particles with uniform size, the maximum volume fraction on the droplet surface ${Y_S}^*$ is 0.6. Eqn. 3.33 shows that β^* is only dependent on the contact angle (θ). Figure 38 shows the value of β^* as a function of contact angle. For particles with small contact angle, the evaporation rate change is insignificant. For the hydrophilic particles with the contact angle of 10°, the evaporation rate at the end of first evaporation stage is 97.3% of the pure liquid. For small contact angle, the cap of the particles that are exposed above the liquid surface is small. The effect of particles on the evaporation in the first evaporation stage is negligible for particles with small contact angle. However, the effect on the evaporation rate change becomes more significant as contact angle increases. For a particle with the contact angle of 30°, the evaporation rate at the end of the first evaporation stage is 77.5% of the pure liquid. The change of evaporation rate in the first evaporation stage is 22.5%, in which the evaporation in the first evaporation stage could not be simplified as that of pure liquid.

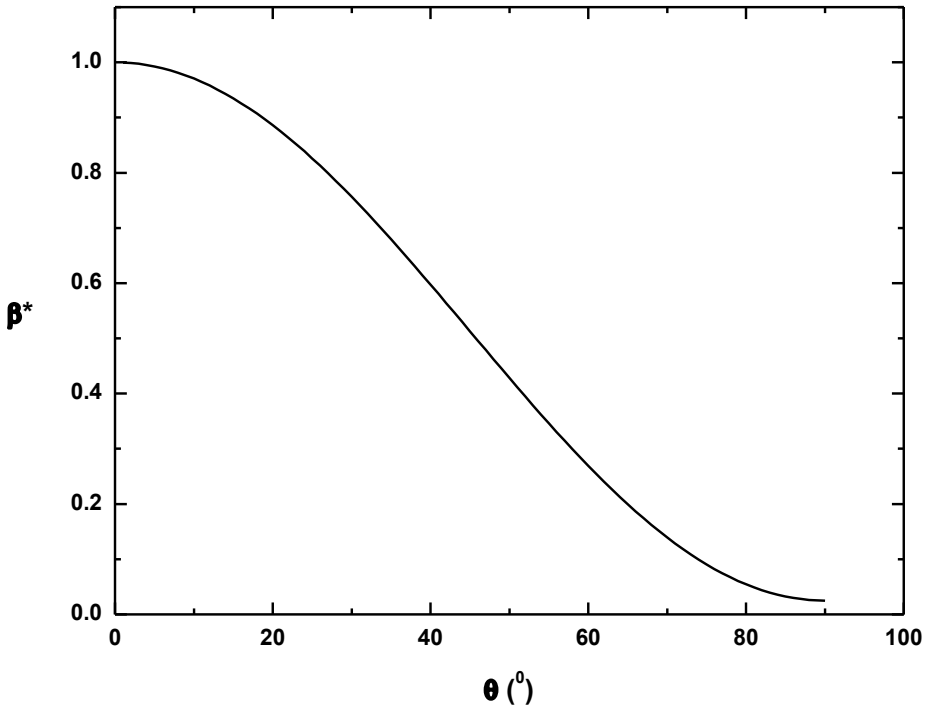

Figure 38 The evaporation rate ratio at the end of first evaporation stage as a function of contact angle

3.4 Conclusion

A theoretical model is developed to describe the effect of particles on the evaporation of droplet containing particles in the first evaporation stage. The particle transport process is described by diffusion equation without considering internal circulation. For the liquid suspension, the introduction of particles on the droplet surface reduces the area the liquid vapor can go through. The effect of particles on the evaporation is described by the ratio of effective surface area that the liquid vapor diffuses to the whole droplet surface area. The analytical solution of the model is described as a function of Peclet number, initial particle concentration and particle contact angle.

The model is validated by comparing the prediction of droplet size history with the published data for the same physical process.

The effect of Peclet number on the evaporation process in the first evaporation stage is studied. For $Pe \ll 1$, the particles have sufficient time to redistribute within the droplet, leading to a small number of particles residing on the surface. The effect of particles on the evaporation rate of droplet in the first evaporation stage is therefore small. For larger Peclet numbers, the particles accumulation rate is enhanced due to relative smaller particle diffusion inward speed. More particles are trapped on the droplet surface, resulting in a decreasing surface area for in the first evaporation stage. The Peclet number also has an effect on the droplet size when the first evaporation stage terminates. Under specific initial droplet size, the final dry particle size increases as Peclet number increases.

Studies on the effect of duration of the first evaporation stage show that for smaller concentration and lower Peclet number, the duration time is much closer to the evaporation time of pure liquid. For the higher particles concentration, the time to reach the shell formation and the end of the first stage is shorter.

It is also found that there exists a criteria for allowing the evaporation of liquid suspension under different initial particles concentration and Peclet numbers, The evaporation can proceed only when $Y_{V0}Pe \ll 1.8$, otherwise the the first stage terminates at the beginning of the first evaporation stage and the size of the final dry particle is equivalent to the initial droplet size.

Contact angle is a major factor affecting the change of evaporation rate in the first evaporation stage. For particles with small contact angle, the overall change is

insignificant and it is reasonable to simply the first evaporation stage as that of pure liquid. While for the large contact angles, the change of evaporation rate in the first evaporation stage is significant and the effect of particles on the evaporation in the first evaporation stage should be considered.

CHAPTER 4. THEORETICAL MODEL WITH INTERNAL CONVECTION

4.1 Introduction

Chapter 3 discussed the two competing transport processes: droplet shrinking and particles diffusion. It is notable that for the evaporation of droplet, interaction between the droplet surface and the surrounding gas plays an important role in the levitation of the droplet. When there exists a velocity between the droplet and the surrounding gas, a shear force will be generated on the droplet surface. The shear force results in liquid motion on the droplet surface, leading to liquid motion on droplet surface and internal recirculation within the droplet. The liquid recirculation enhances both heat and mass transport by affecting the particles mixing and droplet recession rate (Law 1982; Sirignano 1983). In Chapter 3, the effect of internal recirculation on the evaporation is described by modifying particle diffusion coefficient in the liquid phase. The particle mass diffusivity is elevated when internal circulation is involved. The stronger internal circulation, the larger the particle mass diffusivity. It is expected that when internal circulation is strong enough that the particles have enough time to redistribute within the droplet during the evaporation process. This chapter aims to study the effect of particles on the evaporation of liquid suspension with vigorous internal circulation. First, the characteristic times of various transport processes, namely particle diffusion, axi-symmetric gas-phase convection and droplet evaporation, are discussed. Then a dynamic model which accounts for the liquid flow field, particles diffusion and axi-symmetric gas-phase convection is applied to study the effect of particles initial volume fraction, particles

mobility and evaporation rate on the evaporation of liquid suspension in the first stage.

4.2 Characteristic time of particles diffusion, internal convection and droplet evaporation

The interaction of the two phases across the liquid-gas interface frequently introduces internal circulation (Hill, 1894). For droplets containing particles, the particles diffusion is affected by the convective flow within the droplet.

The fundamental theory of internal circulation within a droplet was first theoretically investigated by Hill (1894). The author proposed an axisymmetric vortex, which is now known as Hill's vortex, to describe the internal flow in the droplet that is exposed to a laminar flow. Hadamard (1911) solved the basic hydrodynamics of the liquid droplet with creeping viscous flow passing by. Hill's vortices were later visualized by Garner (1954). Recently, Wong et al. (1992) provided evidence of internal recirculation inside large, hydrocarbon droplets in high temperature gas streams. They captured the transient internal temperature distribution that is caused by internal droplet dynamics.

The mechanism of internal circulation of liquid droplets has been described in several droplet evaporation models (Prakash and Sirignano, 1980; Renksizbulut and Haywood, 1988). Creeping flow analysis is mostly adopted to predict the strength of the internal circulation and the flow patterns inside the liquid droplet (Hardamard, 1991). Consider a uniform, axi-symmertric, slow viscous flow passing around a droplet. The stream function inside the liquid droplet, ψ_i, is written as

$$\psi_i = \frac{1}{4} U_\infty sin^2\theta \left(\frac{1}{1+\sigma}\right) r^2 \left(\frac{r}{r_s}^2 - 1\right) \quad (4.1)$$

$$\text{With } \sigma = \mu_o/\mu_i \quad (4.2)$$

Where r is the radial distance from the droplet center, r_s the droplet radius, U_∞ is the velocity of the gas flow far away from the droplet, μ_o and μ_i are the dynamic viscosities outside and inside the droplet. The tangential velocity $v_i(r,\theta)$ inside the droplet is defined from equation 4.1

$$v_i(r,\theta) = \frac{1}{rsin\theta}\left(\frac{\partial \psi_i}{\partial r}\right)_\theta = \frac{sin\theta}{2}\left(\frac{\sigma}{1+\sigma}\right)\frac{U_\infty}{r_s^2}(2r^2 - r_s^2) \quad (4.3)$$

The evaluation of ψ_i shows that the flow field inside the liquid droplet is symmetric to the flow axis of the flow outside the droplet. Figure 39 shows the flow field inside a circulating water droplet at an intermediate Re number (Re=30). It is seen that there exists a stagnation point inside the droplet, $r = r_{s/\sqrt{2}}$. The velocity of the liquid is zero along a stagnation ring where $\theta = \pi/2$ and where $\theta = 3\pi/2$ and $r = r_s/\sqrt{2}$. The characteristic lengths and times are changed by the internal circulation. For droplet evaporation with a lack of internal circulation, the particles transport process is driven by the Einstein Stokes diffusion and the length for particles diffusion is r_s.or droplet evaporation with internal circulation, the particle diffusion length is the distance from the stagnation point to the droplet surface. The characteristic time of particle diffusion is

$$\tau_{diff} = \frac{L_{diff}^2}{D_{pl}} = \frac{\left(1-\frac{\sqrt{2}}{2}\right)^2 r_s^2}{D_{pl}} = \frac{0.086 r_s^2}{D_{pl}} \sim \frac{0.02 d_s^2}{D_{pl}} \quad (4.4)$$

where d_s is the droplet diameter, and D_{pl} is the mass diffusivity of particles in the liquid phase.

The characteristic time of evaporation is

$$\tau_{evap} = \frac{d_s^2}{K} = \frac{4r_s^2}{K} = \frac{d_s^2}{K} \tag{4. 5}$$

where K is the evaporation rate of pure liquid. The characteristic time of flow convection is

$$\tau_{conv} = \frac{d_s}{V_0} \tag{4. 6}$$

Where V_0 is the characteristic velocity of the internal flow, which is to be determined. To get the value of V_0, the boundary condition is applied. For a droplet with gas flow passing by, the drag (shown in Figure 40) is written as

$$F = 3\pi\mu_{gas}u_\infty d_s \tag{4. 7}$$

The shear force at the gas liquid interface is

$$\mathrm{F} = \mu_{liquid}A\frac{\partial u}{\partial r} = \mu_{liquid}(\pi d_s^2)\frac{V_0}{d_s/2} \tag{4. 8}$$

where A is the droplet surface area, μ_o and μ_i are the dynamic viscosity of the surrounding gas and liquid. Combining equations (7) and (8) we have

$$V_0 = \frac{3}{2}\frac{\mu_{gas}}{\mu_{liquid}}U_\infty \tag{4. 9}$$

For water droplet in air flow

$$V_0 \sim \frac{\mu_{gas}}{\mu_{liquid}}U_\infty \sim \frac{1}{1000}U_\infty \tag{4. 10}$$

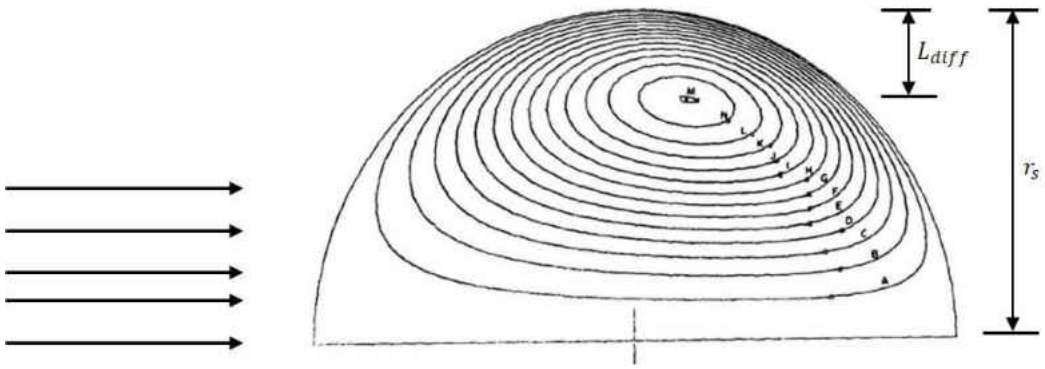

Figure 39 Flow fields inside circulating water droplet for Re=30, (Leclair et al. 1972)

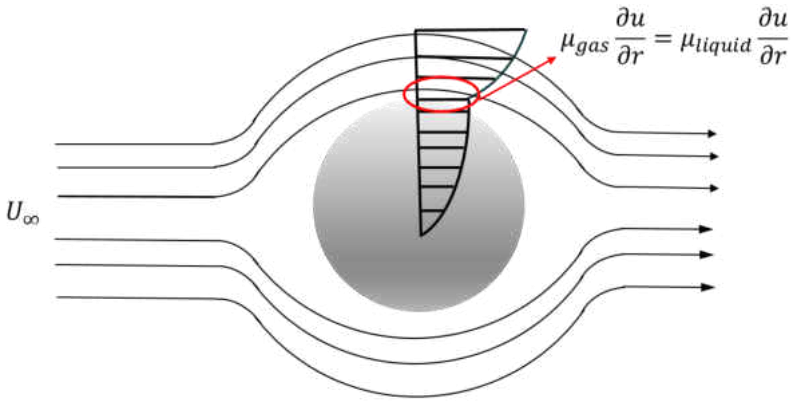

Figure 40 Schematic of flow passing a single droplet

Consider a single water droplet suspension in air flow at weak forced convection, where the size of the suspended particles is 100 nm and the air velocity is 5.5 cm/s. The evaporation rate constant of K of the water is 10^{-9} m^2/s. For 100 nm particles, $D_{pl} = 10^{-11}$m^2/s from Einstein-Stokes equation. The value of τ_{diff}, τ_{conv} as a functions of d_s are plotted in Figure 41. The figure shows there are two cross sections between the various transport time scales. The diffusion time and convection time are the same at the droplet size of 18 μm.

For droplet size larger than 18 μm,

$$\tau_{diff} > \tau_{evap} > \tau_{conv} \tag{4. 11}$$

The convection time is much smaller than the diffusion time. Internal circulation is dominant. The particles are driven toward the inside of the droplet, and the effect of particles on the surface heat and mass transfer is negligible due to the quick particle redistribution within the droplet. For droplet size between 8.9 μm and 18 μm,

$$\tau_{diff} > \tau_{conv} > \tau_{evap} \tag{4. 12}$$

The droplet shrinking process is fast. The particle diffusion time is longer and particles are trapped on the surface. For a droplet of size smaller than 8.5 μm,

$$\tau_{conv} > \tau_{diff} > \tau_{evap} \tag{4. 13}$$

The evaporation time is the shortest. The particles will be captured at the droplet surface before the particles redistribute by diffusion. Also, the particles diffusion time is shorter than the liquid convection time. The effect of the internal circulation is limited and can be regarded negligible. The theoretical model can be simplified without accounting for the internal convection.

The above discussion of the characteristic times are based on specific flow velocity under intermediate *Re* number (Re=5). The following will discuss the transport processes under different flow velocities.

The ratio of the characteristic time of evaporation to that of particle diffusion is

$$\frac{\tau_{evap}}{\tau_{diff}} = \frac{50D_{pl}}{K} \tag{4. 14}$$

The ratio of characteristic time of convection to that of particle diffusion is

$$\frac{\tau_{conv}}{\tau_{diff}} = \frac{d_s/V_0}{V_0} = \frac{1000d_s/U_\infty}{0.02d_s^2/D_{pl}} = \frac{5\times10^4 D_{pl}}{U_\infty d_s} \tag{4. 15}$$

In the theoretical model discussed in chapter 3, the *Pe* is defined as

$$Pe = \frac{K}{8D_{pl}} \tag{4. 16}$$

Equation 14 is rewritten as

$$\frac{\tau_{evap}}{\tau_{diff}} = \frac{50D_{pl}}{K} = \frac{6.25}{Pe} \tag{4. 17}$$

Equation 17 shows that the ratio of evaporation and diffusion time is independent of the droplet size. The morphologies of the dried particles in the evaporation process are determined by the Peclet number. For Pe ≫ 6.25

$$\tau_{evap} << \tau_{diff} \tag{4. 18}$$

Because the evaporation time is shorter, more particles are trapped on the surface, the droplet surface can get saturated more easily. By the end of the first evaporation stage, a porous shell will be formed. For smaller *Pe*, the particle diffusion rate is fast and the particles have enough time to redistribute within the droplet. By the end of the first evaporation stage, a solid aggregate particle will be formed.

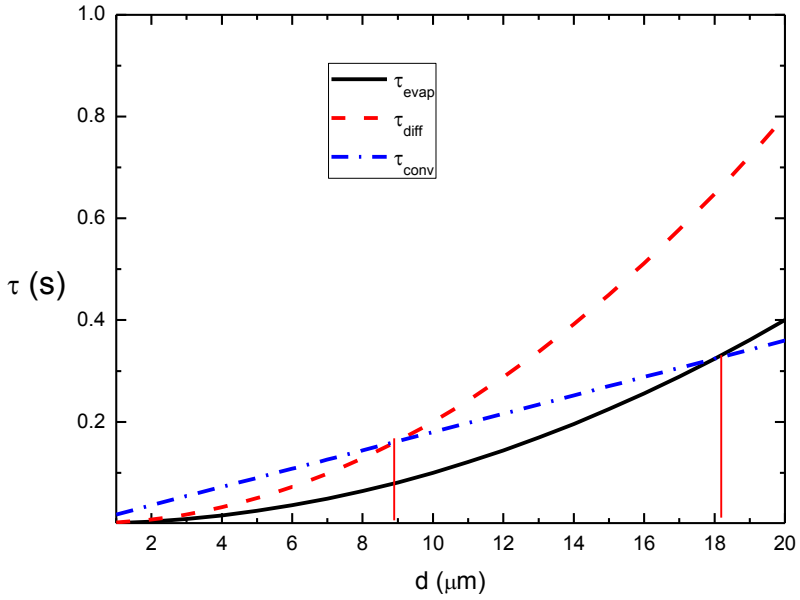

Figure 41 Times of various transport processes as a function of droplet size

A general form of the ratio of characteristic time of convection to that of particle diffusion is written as

$$\frac{\tau_{conv}}{\tau_{diff}} = \frac{5\times10^4 D_{pl}}{U_\infty d} \quad (4.19)$$

The droplet size, when the characteristic times of convection and particle diffusion are the same, d_{static}, is rewritten as

$$d_{static} = \frac{5\times10^4 D_{pl}}{U_\infty} \quad (4.20)$$

The droplet size at which whether the internal convection can be ignored, is controlled by the particle mass diffusivity and flow velocity. For droplet size smaller than d_{static}, the diffusion time is shorter than the convection time, and the internal circulation is weak compared to convection. For a larger droplet, the effect of the internal flow transport becomes much more important and should not be ignored. The droplet size, when the theoretical model in Chapter 3 applies, decreases as flow velocity increases.

4.3 Theoretical model with internal convection

The evaporation model that accounts for the internal vortex circulation was firstly developed by Lara-Urbaneja and Sirignano (1981) to simulate the evaporation of a multicomponent droplet in a convective field. Then, Tong and Sirignano (1984) simplified the model, which is based on the assumption that there exists a Hill's spherical vortex inside the droplet. Tong and Sirignano (1984) compared the results of their simplified model to a more detailed model and found close agreement. Eslamian and Ashgriz (2006) followed the same arguments in Tong and Sirignano (1986) and extended the analysis to the evaporation of droplet containing insoluble solutions. The simulation results provide good insight in predicting the morphology

of the dry particles. In this study we extend the analysis to liquid suspension to study the effect of the internal circulation on the evaporation of droplets containing particles. For the evaporation of droplets containing particles at a given temperature and pressure, the particles are initially evenly distributed within the droplet. The evaporation is assumed to be quasi-steady and temperature through the droplet is uniform. The one-dimensional liquid phase mass concentration equation (Tong and Sirignano, 1986) is written as

$$\frac{\partial Y_l}{\partial \tau} = \frac{\phi}{Le}\frac{\partial^2 Y_l}{\partial \phi^2} + \left(\frac{1}{Le} + C\phi\right)\frac{\partial Y_l}{\partial \phi} \tag{4. 21}$$

Where the dimensionless stream function ϕ is expressed based on Hill's vortex approximation

$$\phi = 1 - 4s^2(1 - s^2)sin^2\theta \tag{4. 22}$$

and

$$s = r/r_s \tag{4. 23}$$

$$d\tau = \frac{\alpha_l}{R^2}dt \tag{4. (24)}$$

Y_l is the liquid mass fraction, τ isthe dimensionless time, and Le is the liquid phase Lewis number, which is defined as the ratio of liquid heat diffusivity to the inter particle liquid mass diffusivity.

$$Le = \frac{\alpha_l}{D_{pl}} \tag{4. 25}$$

C relates to the droplet evaporation rate and is given by

$$C = 2\left(\frac{R_0}{R}\right)^{\frac{3}{2}}\frac{d}{d\tau}\left(\frac{R}{R_0}\right)^{\frac{3}{2}} \tag{4. 26}$$

Note that this is different from c in chapter 3, which denotes particle number concentration. The initial and boundary conditions are:

$$(1)\,\tau = 0, Y_l = Y_{l0}$$

$$(2)\,\phi = 0, \frac{\partial Y_l}{\partial \phi} = Le\frac{\partial Y_l}{\partial \tau}$$

$$(3)\,\phi = 1, \frac{\partial Y_l}{\partial \phi} = f_l \tag{4. 27}$$

Where $Y_{l0}$is the initial liquid phase mass fraction. f_l is given by

$$f_l = \frac{LeC_{pl}(Y_{ls}-1)}{16\pi r_s \lambda_l}\dot{m} \tag{4. 28}$$

Where C_{pl} is the liquid phase capacity, Y_{ls} is the liquid mass fraction at the droplet surface, and λ_l is the conductivity of the liquid phase. In the case of strong internal convection and constant value of K, C can be rewritten as

$$C = 2\left(\frac{R_0}{R}\right)^{\frac{3}{2}}\frac{d}{d\tau}\left(\frac{R}{R_0}\right)^{\frac{3}{2}} = \frac{3}{\alpha_l}\frac{dR^2}{dt} = \frac{3K}{2\alpha_l} \tag{4. 29}$$

C is the ratio of evaporation rate to the liquid phase thermal diffusivity.

The partial differential equation (PDE) of diffusion of the liquid phase (equation 4.21) is numerically solved. With the time and space discretization method, the particle concentration distribution at any given time is obtained. The computation is stopped when the particle mass fraction at the droplet surface reaches the maximum value, at which the particles could not compact anymore. Note that for particles with uniform size, the maximum volume fraction is 0.6. Since the solution of the equations deals with mass fraction, we did the conversion based on the density of the liquid and solid phases ($Y_{pv} = \frac{Y_p\rho_l/(1-Y_p)}{Y_p\rho_l/(1-Y_p)+\rho_s}$, where$Y_{pv}$ and Y_p denote the particle volume and mass fraction. ρ_l and $\rho_s$are density of the liquid phase and solid phase, respectively.). Solving the liquid transport equations allows the study of the initial

particle concentration, particle mobility and evaporation rate on concentration distribution within the droplet, duration of the first evaporation stage and dry particle size for the evaporation process of droplet containing particles.

4.4 Results and discussion

Figure 42 shows the stream function contour within the droplet in the case of strong internal circulation. There exists two axisymmetric vortex within the droplet. The maximum strong function happens at the droplet surface and center. The stream function is zero along a stagnation ring where $\theta = \pi/2$ and where $\theta = 3\pi/2$ and $r = r_s/\sqrt{2}$, which has been discussed in Section 4.2. For the evaporation of droplet containing particles lack of internal circulation, the minimum particle concentration appears at the droplet center. The particles will build a crust at the droplet surface in the first stage and the crust thickens at the second stage. Finally a dry aggregate particle with the structure of either shell or solid is formed as described in Chapter 1. For the evaporation of a droplet with internal circulation, the maximum particle concentration occurs at locations with the strongest convection ($\phi = 1$). The two axisymmetric vortex results in two minimum particle concentration locations where $\phi = 0$. Once the particle concentration at the droplet center and droplet surface reaches the maximum value, the accumulation of particles start to grow and merge together to make a particle with two cavities. The liquid will diffuse through the inter particle space and a dry aggregate particle with two cavities is formed, which explain the dimples that appear on the dry spherical aggregate particle shown in Figure 2.

The evaporation of a single water droplet containing nano silica particles with the size of 30 nm has been studied. Table 5 provides the model parameters used in the computations. Y_{pi} is the initial particle mass fraction. Figure 42 shows the evolution of the particle volume fraction profile within the droplet. As discussed in Chapter 3, for evaporation of a spherically symmetric droplet, the minimum solid concentration happens at the droplet center. While for a droplet with internal recirculation, the minimum solid concentration occurs at the vortex center ($r = r_s/\sqrt{2}$), where ϕ equals zero (as shown in Figure 42). The particle volume fraction increases as evaporation proceeds. The particle concentration profile evolution history shows that particles diffuse toward the vortex center. Initially the particles are evenly distributed within the droplet. At 5.7 s, the particle concentration at the droplet center and surface increases. As evaporation proceeds, the particles diffuse toward the vortex center. At the end of the first stage, the particle concentration is high at the locations with strong internal circulation. For locations with weak convection ($\phi = 0.4 \sim 0.8$), the particle volume fraction remains the same as the initial value, demonstrating that the particle diffusion is slower compared to the convection. Figure 43 also shows that the maximum solid concentration occurs at the maximum streamline ($\phi = 1$), which includes the surface and the droplet center. This result agrees with that of the model which is applied in the spray pyrolysis (Eslamian et al., 2006).

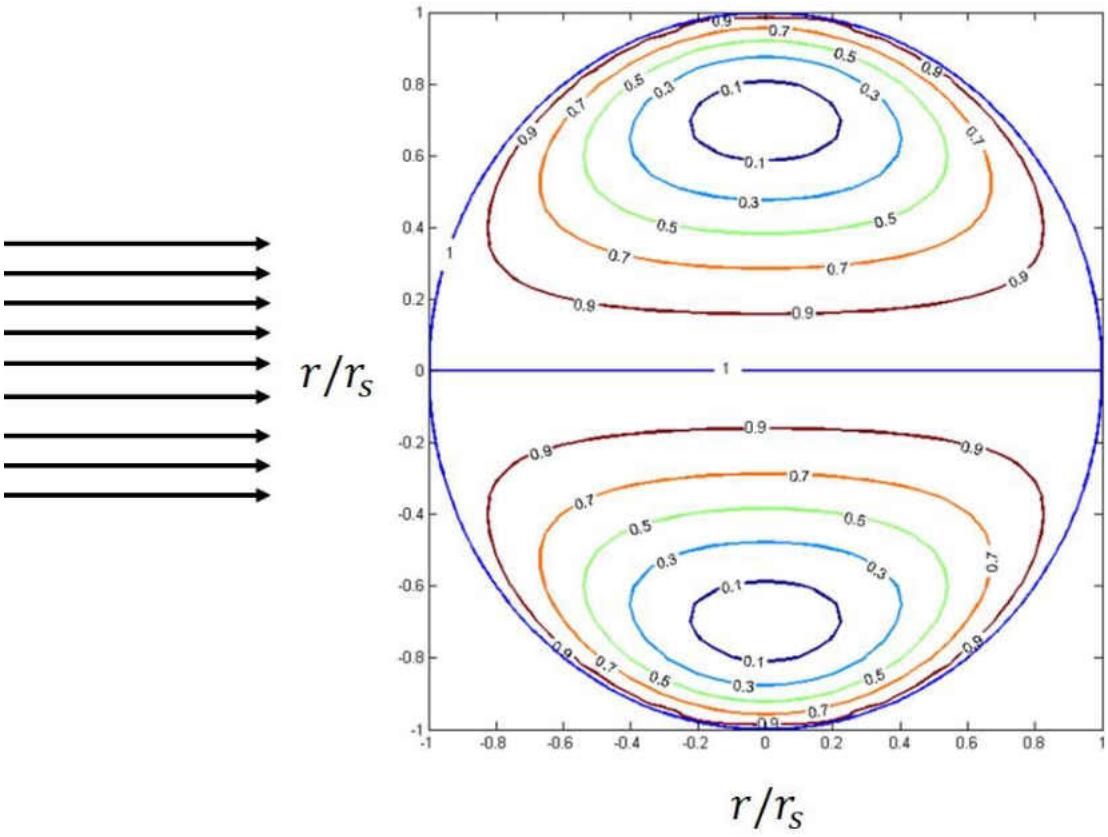

Figure 42 Stream function contour within the droplet with internal circulation

Table 5 Initial values for parameters in the computations

d_0 (mm)	K (m^2/s)	Y_{pi} (%)	ρ_p (g/cm^3)	α_l (m^2/s)	D_{pl} (m^2/s)	Le
1	10^{-9}	30	2.09	1.43×10^{-7}	1.43×10^{-11}	10,000

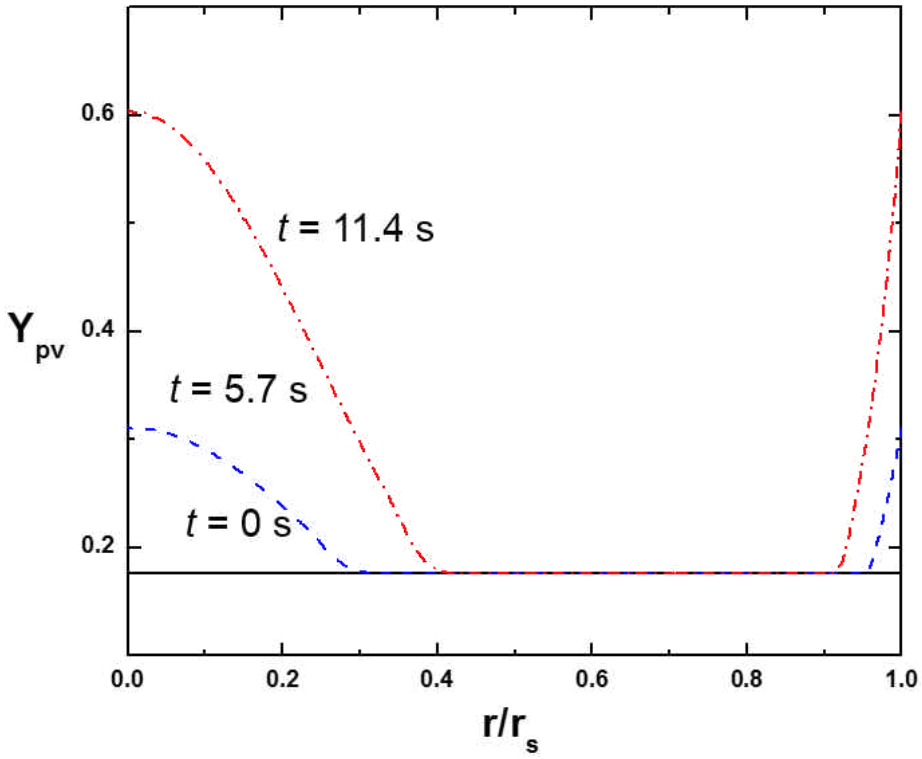

Figure 43 Variation of the particle volume fraction

4.4.1 Effect of particle mobility on the evaporation of the first evaporation stage

As discussed in Chapter 3, the evaporation mechanism of a liquid suspension is controlled by three competing transport processes: the particle mass diffusion, internal convective flow and droplet surface regression. In the case of slow evaporation and vigorous internal convective flow, the first stage is controlled by the particles' mobility, which is characterized by particle mass diffusivity. In the model, the effect of particle mobility on the evaporation process can be characterized by a dimensionless parameter, the Lewis number. Since particle mass diffusivity in the liquid is usually far much smaller than thermal diffusivity, *Le* is a large number. For a water droplet containing 100 nm nano silica particles, the liquid phase thermal

diffusivity is 1.43×10^{-7} m^2/s. The particle mass diffusivity is calculated from the Einstein-Stokes equation,

$$D_{pl} = \mu k_B T = \frac{k_B T}{6\pi\eta r_p} \tag{30}$$

Where k_B is the Boltzmann's constant, μ is the mobility, T is the temperature, η is the dynamic viscosity and r_p is the particle radius. The particle mass diffusivity is 10^{-12} m^2/s. Therefore, the Lewis number is around 10^5 for the liquid suspension, which is far larger than the gas phase and liquid phase. For the gas phase, Le is around 1. For the liquid phase, the Lewis number is relatively larger, which is around 30 (Makino and Law, 1988).

In this section, we will discuss the effect of Lewis number on the evaporation of water droplets containing 5 wt.% nano silica particles. The droplet has the initial size of 1 mm. The density of the silica particles is 2.09 g/cm^3. The evaporation rate is 10^{-9} m^2/s. Figure 44 shows the evolution of surface particle volume fraction under various Lewis numbers. It is seen that as evaporation proceeds, the droplet surface becomes more concentrated with particles. The first evaporation stage terminates when a shell of particles is formed, at which the volume fraction of the silica particles reaches 0.6. It can also be seen from the figure that for small *Le* (*Le*=1), the surface particle concentration reaches the saturation value within a very short time. The time that is needed for the formation of the first layer of the shell gradually increases as *Le* increases, until *Le* reaches 1000. As *Le* further increases, the surface particle concentration history does not change for *Le*>1000 as can be seen in Figure 43, and the duration of the first stage remains the same. Figure 45 shows the variation of duration of the first evaporation stage (t^*) under different Lewis numbers. Initially

t^* shows great increase as Lewis number increases with a large slope and then the slope becomes smaller until it finally becomes flat at Le=1000.

For a given evaporation rate, the evaporation process is controlled by the two competing transport processes, the particle diffusion and internal vortex. For particles with high mobility, the particle diffusion is strong and the particles near the droplet surface would be driven inward by the flow. As Le number increases, the mobility of the particles decreases and the effect of the flow recirculation on the particles becomes stronger. Once the particle mobility reduces to a limit that the particles at the droplet surface are only controlled by the internal flow, the surface particle concentration evolution becomes independent of Le. Figures 44 and 45 show that the particles at the droplet surface are only controlled by the flow at Le =1000.

Figure 46 shows the dry particle size under various Le numbers. As Le number increases, the effect of the internal circulation becomes stronger and the evaporation time of the first stage is longer, leading to smaller droplet size. The dry particle size becomes stable once the transport of particles is only controlled by the internal flow.

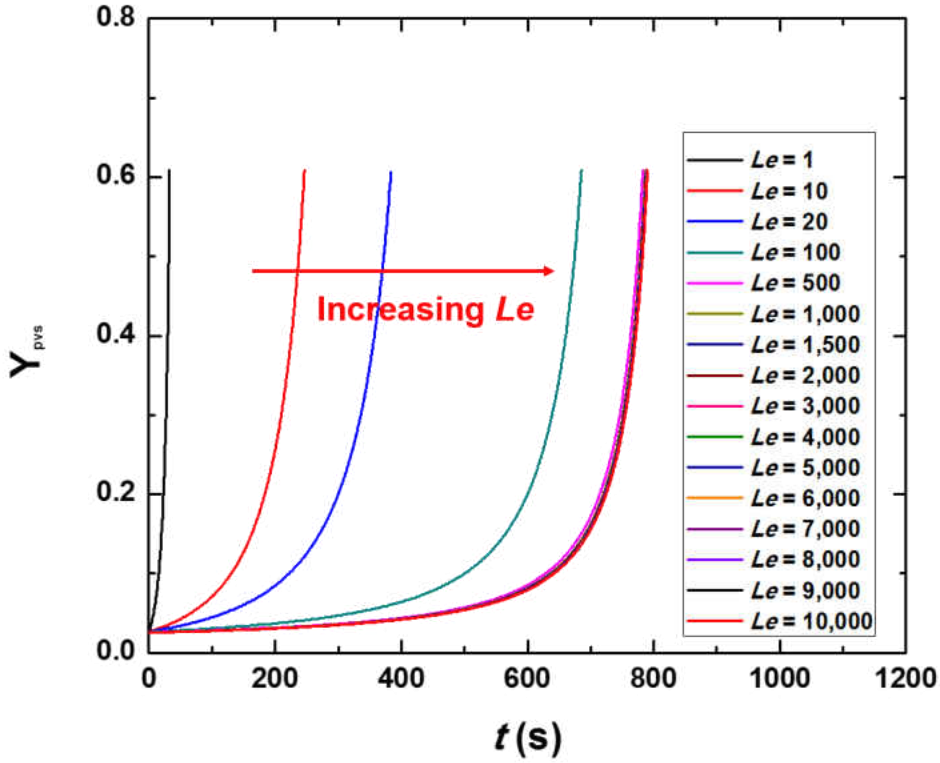

Figure 44 The surface particles concentration evolution under various Le numbers

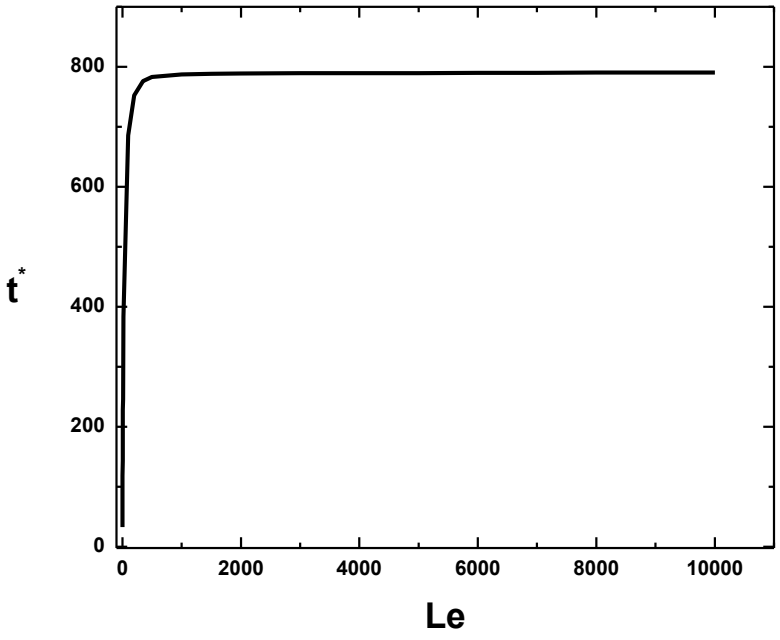

Figure 45 The duration time of first evaporation stage as a function of *Le*

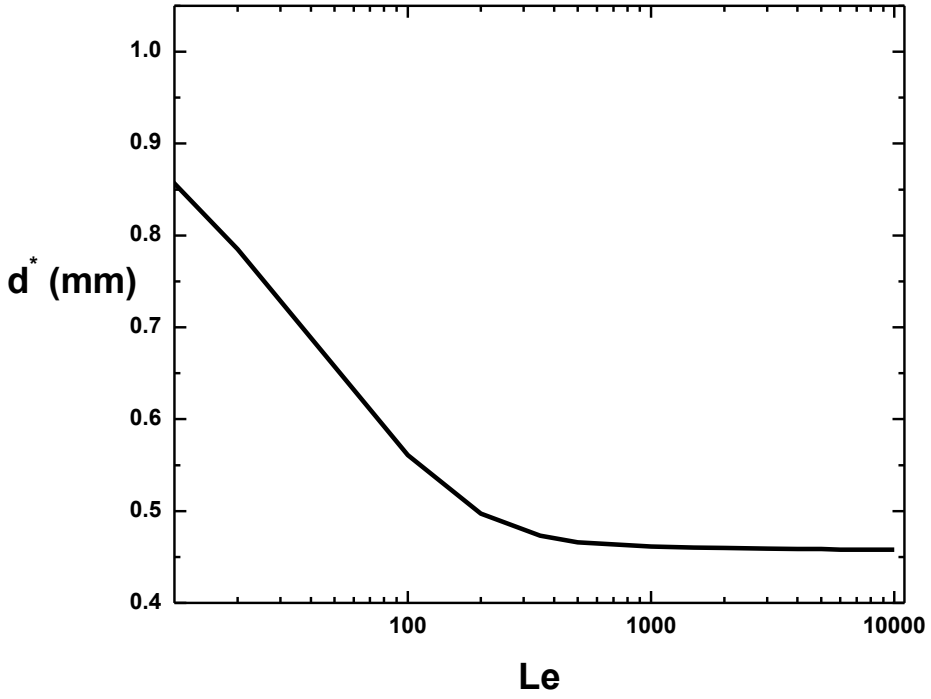

Figure 46 Droplet size at the end of the first evaporation stage under various *Le* numbers

The effect of Lewis number on the particle concentration distribution within the droplet is shown in Figure 47, which shows the particle concentration profile at the end of the first evaporation stage under various Lewis numbers. The normalized stream function is the stream function at $\theta = 90°$ divided by the critical solid volume fraction at the droplet surface at the end of the first stage, which is 0.758 for the nano silica particles. The solid volume fraction distributions under different Lewis numbers are similar with their minimum and maximum concentrations happening at the same points. The maximum particle concentration happens at the location with the strongest convective flow (droplet surface and the). The minimum particle concentration occurs at $r/r_s = \sqrt{2}/2$, which is consistent with the minimum stream

function. This implies that the particle transport within the droplet is controlled by the internal flow and the particles diffuse toward the vortex center, which is different from the particle transport mechanism in the absence of internal circulation. For the droplet evaporation process lacking internal circulation, the particle transport is driven by the particle concentration gradient and the particles diffuse toward the droplet center, at which the minimum particle concentration occurs. The particle concentration distribution under various Lewis numbers shows the combined and competing effect of the two transport processes, particle diffusion and internal convective flow. At small *Le* numbers, the particle concentration profile is smooth. While as *Le* increases, the change of concentration becomes much sharper and the concentration gradient within the droplet becomes larger. At small *Le* numbers, the particles have higher mobility, leading to smaller diffusion time. As the droplet surface recesses, the particles within the droplet always have enough time to redistribute within the droplet. The particle concentration is smoother. As *Le* increases, the particle mobility decreases. The effect of the internal convective flow becomes more dominant. It is seen from Figure 46 that the concentration profile moves toward the stream function line as *Le* increases.

Figure 48 shows the particle concentration distribution in the stream function field. It is seen that the concentration profile is consistent at locations where there is stronger internal flow ($\phi \sim 0.8 - 1$). For the locations with weak flow, the particle mobility affects the concentration profile. At smaller *Le*, the particles have higher mobility. The particles can always redistribute within the droplet. However, compared to the particle transport at which the concentration gradient is the only

driven force, the convective flow affects the particle redistribution. In the case of high mobility particles, for the location with strong internal flow, the concentration is larger. While for the location with weak internal flow, the concentration is smaller due to the particles diffusing. As a result, the concentration profile is linear in the stream function field at smaller *Le*. As *Le* increases, the effect of the particle diffusion becomes weaker due to the reduced mobility of the particles. The concentration gradient becomes larger near the vortex center. As *Le* increases, the concentration profile gradually deviates from the linear distribution at smaller stream function.

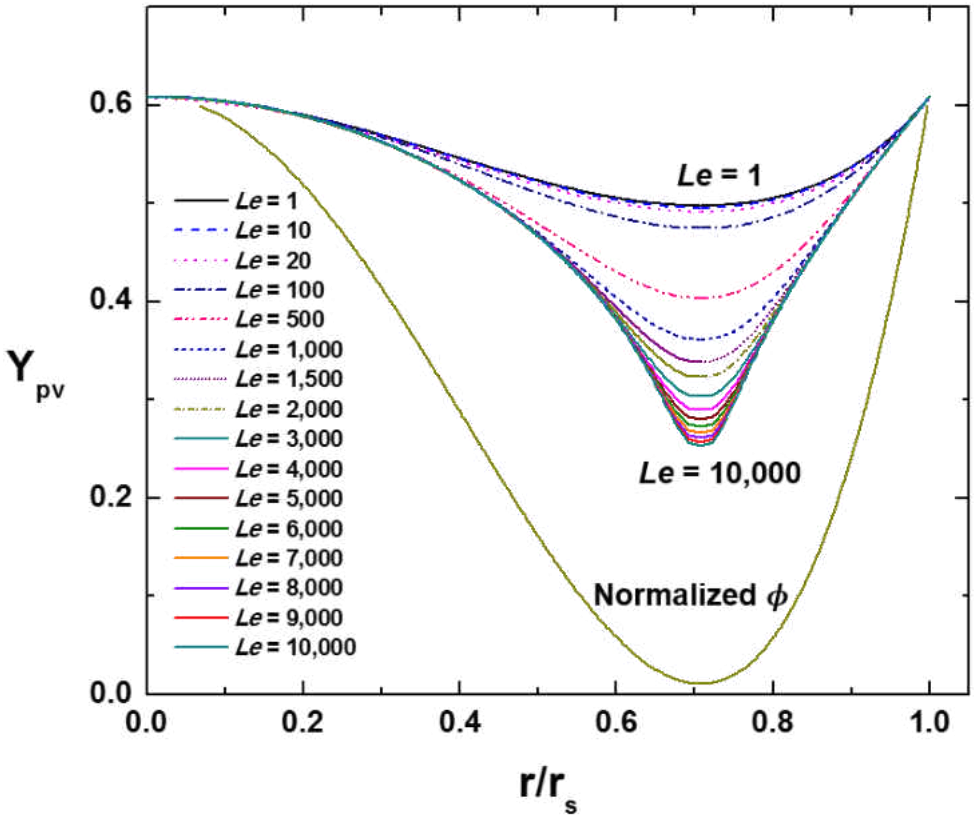

Figure 47 The particle concentration profile at the end of the first evaporation stage under various Le numbers

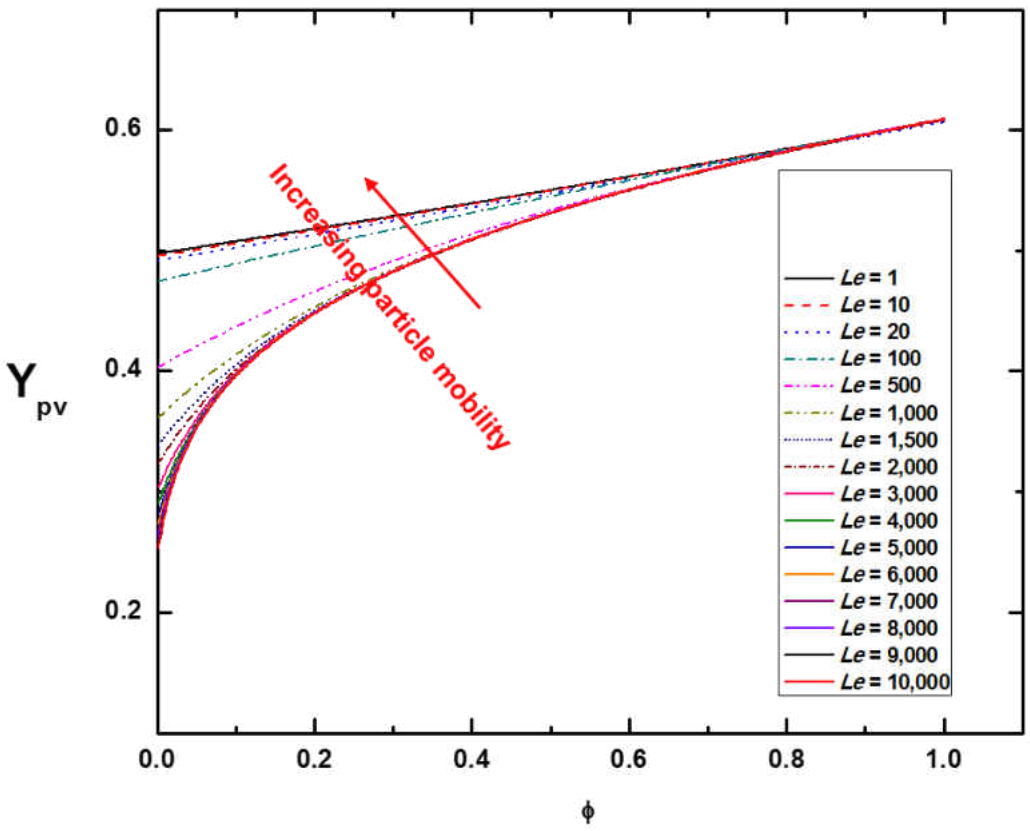

Figure 48 The particle concentration profile as a function of ϕ at the end of the first evaporation stage under various Le numbers

4.4.2 Effect of initial particle concentration on the evaporation of the first evaporation stage

As discussed in Chapter 3, the initial particle concentration affects the evaporation rate in the first stage of evaporation of droplets lacking internal circulation. For the evaporation of droplets with vigorous internal circulation, the particles at the droplet surface will be driven by the recirculating flow, leading to the evaporation in the first stage behaving as that of the pure liquid. Next, we will discuss the effect of the initial particle concentration on the particle concentration profile and duration of the first stage.

Figure 49 shows the particle distribution in the flow field at the end of the first stage under various initial particle concentrations. It is seen that the concentration profile is the same for all the conditions. The particle concentration profile at the end of the first stage is independent of the initial particle concentration. It is reasonable because the particle concentration profile is controlled by the particle diffusion and internal convective flow. For all the concentrations studied in Figure 48, the internal flow and the particle mobility are the same, leading to the same particle profile at the end of the first stage. Figure 50 shows the effect of initial concentration on the concentration profile at different Lewis numbers. It is noted that the concentration profile is determined by the particle mobility and is independent of the initial particle concentration.

The effect of the initial particle concentration is reflected by the duration of the first evaporation stage. Figure51 shows the duration of the first evaporation stage (t^*) at various initial particle concentrations. It is seen that for a given Le number, t^* decreases as initial particle concentration increases. Figure 50 also shows that the duration of the first evaporation stage becomes stable after $Le = 1000$, at which the particles at the droplet surface are only controlled by flow recirculation, due to the small mobility of the particles. Once the transport properties are chosen, the particle distribution at the end of the first stage is determined. The time that is needed to reach the desired particle distribution depends on the initial particle concentration. For smaller initial particle concentrations, the duration time is longer, which is an important factor in controlling the dry particle size. Figure 52 shows the dry particle size under various concentrations. For $Le \leq 1000$, the dry particle size is determined

by initial particle concentration as well as transport properties, *Le*. For a given evaporation rate and a specific particle mobility, the dry particle size can also be controlled by the initial particle concentration. The higher initial particle concentration leads to larger particle size and vice versa. For *Le* >1000, the dry particle size is independent of initial particle concentration.

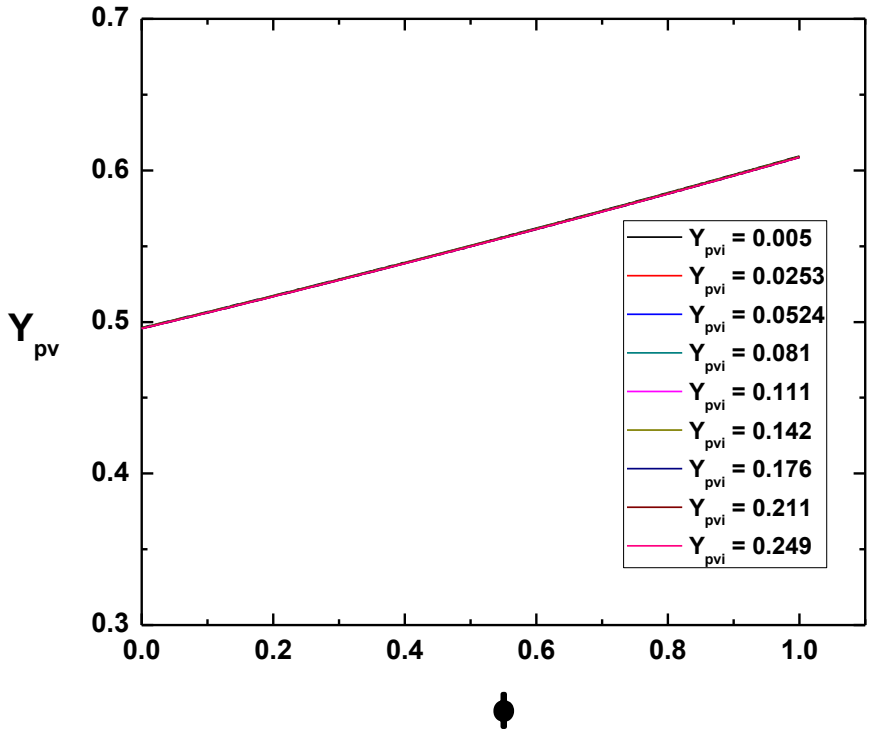

Figure 49 The particle concentration profile as a function of ϕat the end of the first evaporation stage at *Le* =10 under various initial particle concentrations

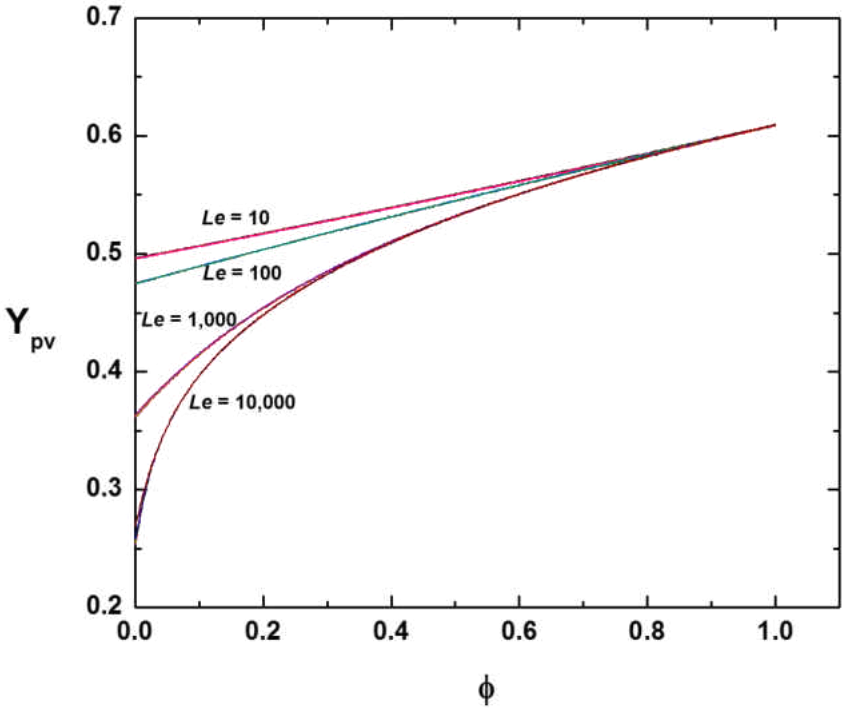

Figure 50 The particle concentration profile as a function of phi at the end of the first evaporation stage

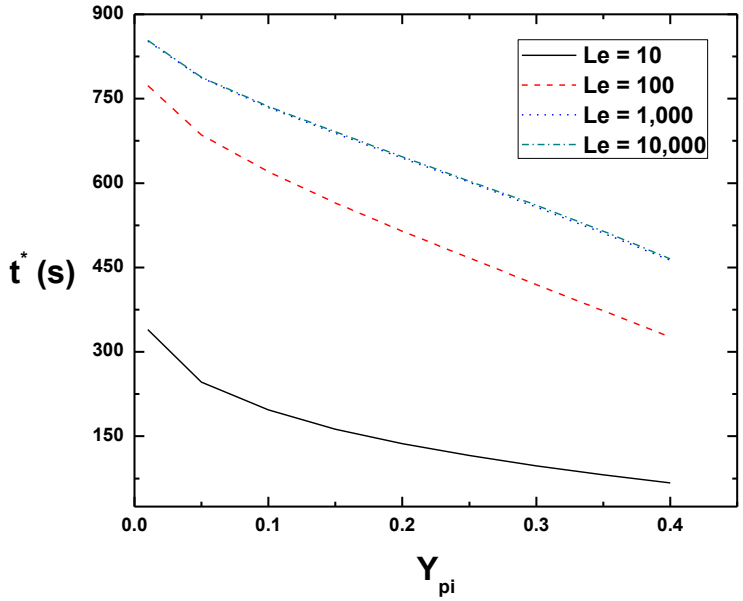

Figure 51 The duration time of the first evaporation stage under various initial particles mass fraction

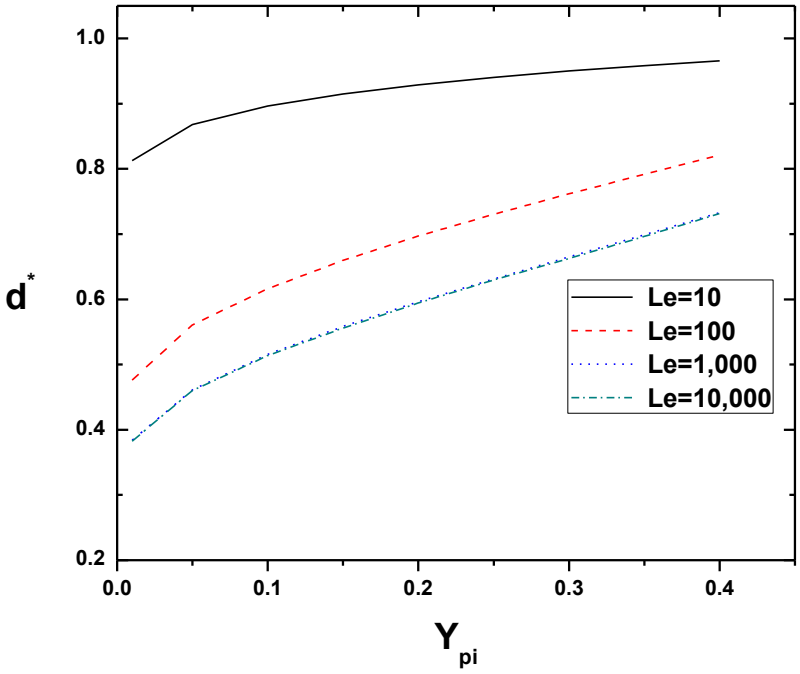

Figure 52 The droplet size at the end of the first stage under various initial particle mass fraction

4.4.3 Effect of evaporation rate on the evaporation of the first evaporation stage

The discussion of the effect of the particle mobility and the particle initial concentration are based on a given evaporation rate, at which, droplet surface recession rate is fixed. In this section we will discuss the droplet shrinking process. Since the studies of the droplet recession and the internal particle diffusion were discussed in Chapter 3, we will focus on the competing effects of internal particle diffusion and droplet recession on the evaporation of droplets containing particles. For all the study cases, the Lewis number is 1000, at which, the particles at the droplet surface are only controlled by the internal flow. Consider a 100 μm water droplet evaporating under various evaporation rates. The mass diffusivity of the nanoparticles is 10^{-10} m^2/s. The initial particle mass fraction is 5 wt.%. In the model,

the evaporation rate is involved in a dimensionless factor, C, (defined as $C = 3\mathrm{K}/2\alpha_l$), which is the ratio of evaporation rate and the liquid phase thermal diffusivity, as described in equation 4.29. The correlation between the evaporation rate and the constant C is listed in table 6.

Table 6 The parameters used in the model

d_0	Le	K(m^2/s)	C
100 μm	1000	10^{-9}	0.01
		5×10^{-9}	0.05
		10^{-8}	0.1
		5×10^{-8}	0.5
		10^{-7}	1

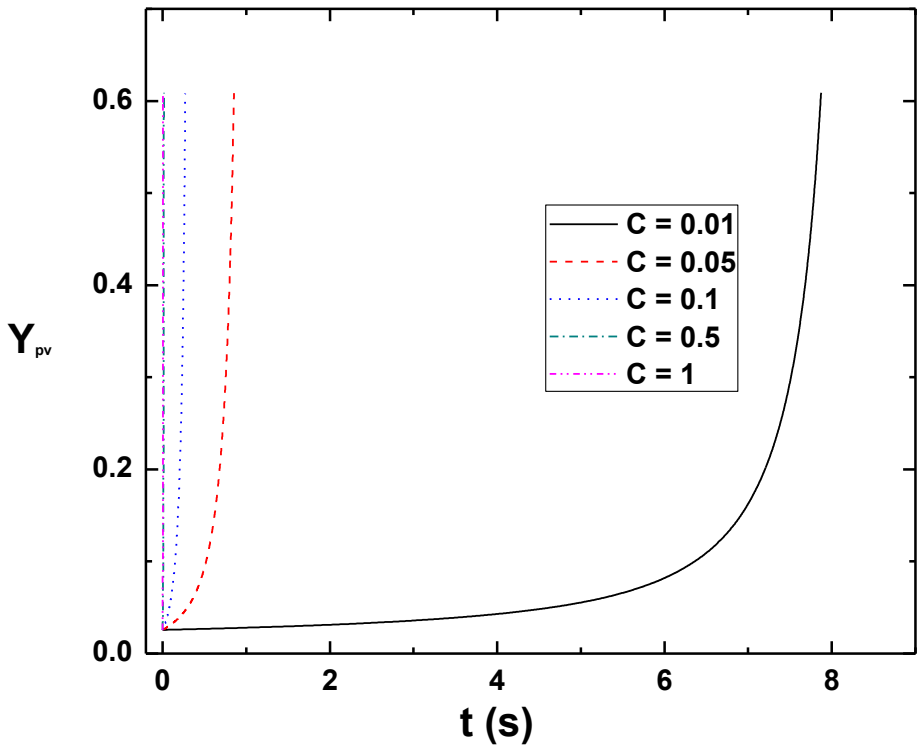

Figure 53 The surface particles concentration history under various values of C

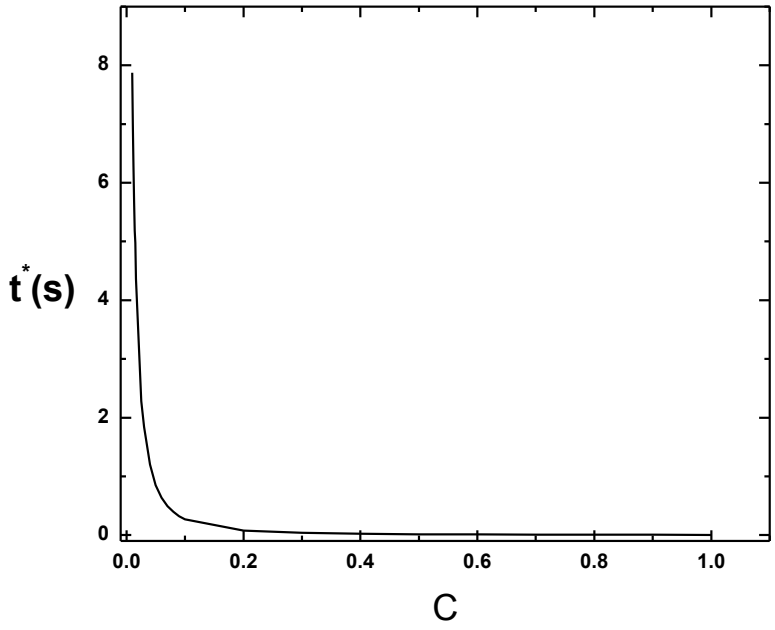

Figure 54 The duration time of the first evaporation stage as a function of C

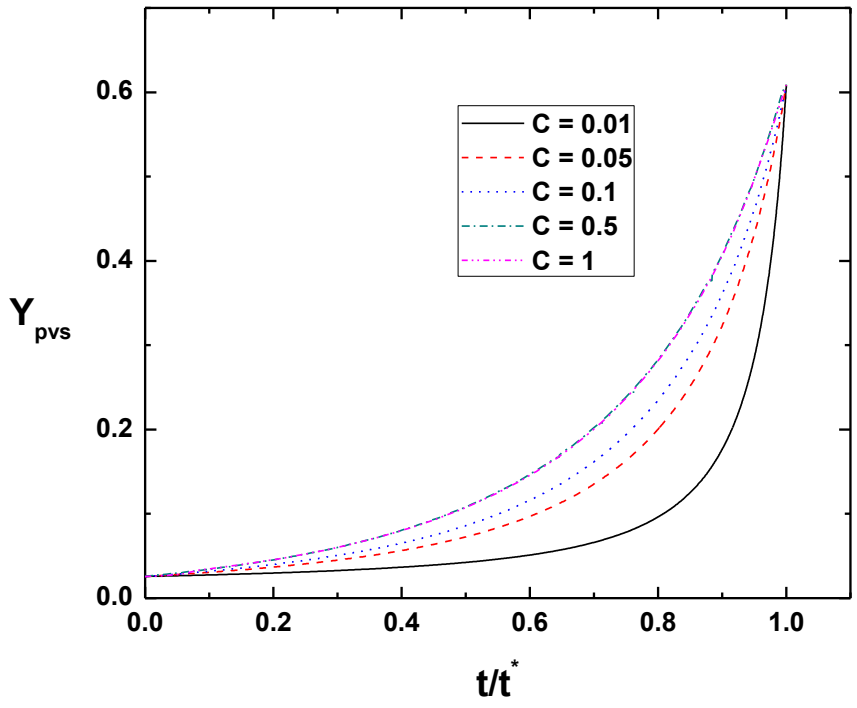

Figure 55 The evolution of surface particle volume fraction under various values of C

Figure 53 shows the surface concentration histories under various C numbers. The particle concentration gradually increases during the evaporation process, until a layer of particles is formed at the surface. It is seen that the concentration evolution profile is much sharper, due to the enhanced evaporation rate. With higher evaporation rate, the droplet recession rate is larger and the surface particles can be easily trapped by the surface. The duration of the first stage (Figure 53) initially shows a dramatic decrease as C increases, then gradually becomes stable.

Figure 55 shows the particle mass fraction history in the dimensionless time field. The horizontal axis is the dimensionless time, the time divided by the duration of the first stage (t^*). It is seen that at a specific dimensionless time, the particle concentration at the droplet surface is higher for higher evaporation rates. As evaporation rate increases, the droplet recession rate is enhanced, leading to smaller droplet recession time. For a specific internal flow and particle mobility, the smaller droplet recession time allows more particles to be trapped on the surface, resulting in higher surface particle concentration.

Figure 56 shows the particle concentration distributions at different C numbers. Due to the existence of strong internal flow, the particle profiles show that the particles diffuse toward the vortex center. As the evaporation rate increases, the effect of droplet recession becomes more dominant. It is shown that for C=0.05, the vortex center at the end of the first e stage is close to the initial particle concentration. As evaporation rate is further increased, the particle concentration near the droplet surface is sharper. The particle concentration at the vortex center remains at the

initial values, which implies that the characteristic time of droplet shrinking is shorter than that of internal flow.

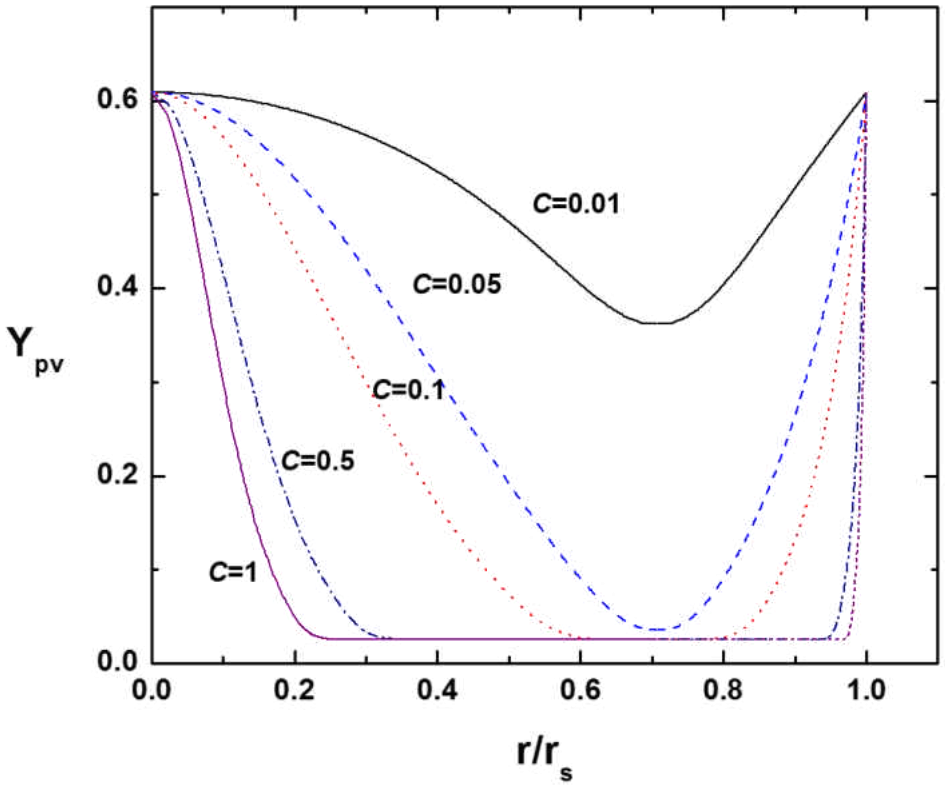

Figure 56 The particle concentration profile at the end of the first evaporation stage under various values of C

Figure 57 shows the particle concentration in the stream function field. For smaller C, the characteristic time of the internal flow is smaller than that of the droplet shrinking. The particle distribution is driven by the internal flow. As C increases, the particles distribution profile is changed due to the decrease of characteristic time of droplet shrinking. The slope at the higher stream function becomes sharper. When the C is increased to 0.1, the profile is changed with the concentration at the vortex center being the initial value. As C is further increased, the droplet evaporation time

is shorter. The first evaporation stage terminates earlier, leaving less time for the particles to diffuse.

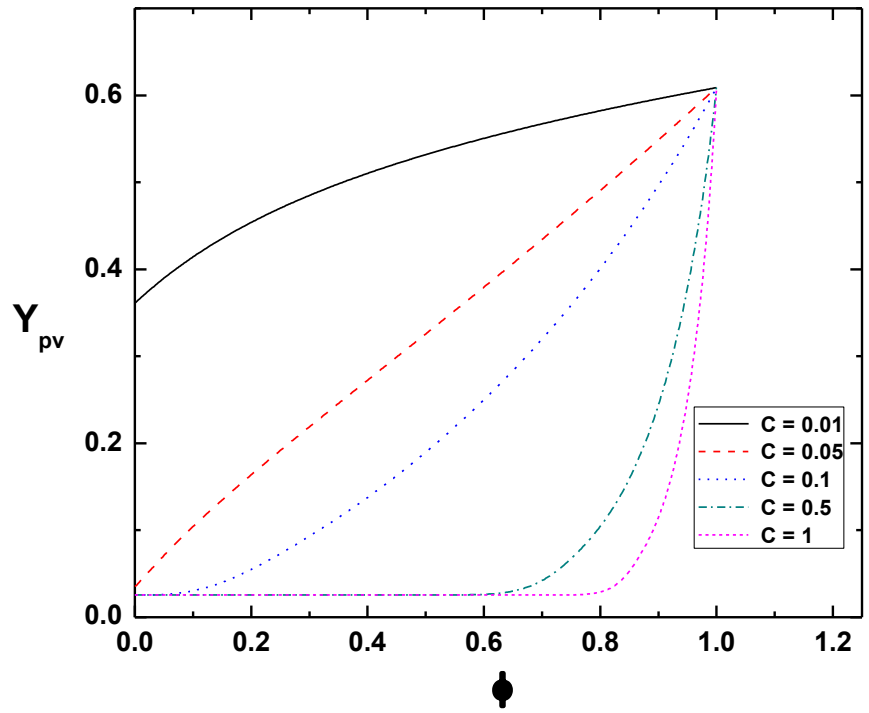

Figure 57 The particle concentration profile as a function of phi at the end of the first evaporation stage under various C

4.5 Conclusion

The evaporation model that accounts for the internal vortex circulation is applied to describe the effects of particles on the evaporation of droplet containing particles in the first evaporation stage. The transport processes involved in the evaporation process, droplet shrinking, particles diffusion and internal flow recirculation are described by diffusion equation in the dimensionless stream function field. In the case of internal circulation, the evaporation rate in the first stage is expected to follow that

of pure liquid, which obeys the classic d^2-law. The effect of particles mobility, initial particles concentration and droplet recession rate on the particles distribution, the duration of the first stage and the final dry particle size are discussed.

For a given droplet recession rate and a specific internal flow, the evaporation process in the first stage is controlled by the particles mobility. Compared to the evaporation of droplet lack of internal flow, the particles distribution within the droplet is affected by the internal flow transport with the maximum particle concentration happening at the droplet surface and its center. The minimum particle concentration occurs at the vortex center. For particles with high mobility, the diffusion time is short. The particles have enough time to redistribute within the droplet. The particles concentration can remain smoother. As the particles mobility decreases, the effect of the internal convective flow becomes more dominant. The concentration profile moves toward the stream function line. It is found that the duration of the first evaporation stage and the final dry particle size is controlled by the surface particles accumulation. For particles with high mobility, the particles at the droplet surface has time to move inward, leading to shorter duration time. While as particles mobility decreases, the particles diffusion time increases. The particles are more easily be trapped on the surface. When the particles mobility is decreased to a limit at which the transport of particles is only controlled by the internal flow, the surface particles concentration evolution becomes stable. After then the duration time and the final dry particle size are independent of the particles mobility.

The particles distribution at the end of the first evaporation stage is independent of the initial particle concentration. The effect of the initial particle

concentration lies in the duration of the first evaporation stage. For smaller initial particle concentration, the duration time is longer and the final dry particle size is smaller.

Droplet evaporation rate is an important transport parameter in controlling the particles distribution and duration time of the first stage. With higher evaporation rate, the droplet recession rate is larger and the surface particles can be easily trapped by the surface. The concentration evolution profile is much sharper near the droplet center and the droplet surface. Further enhancement of evaporation can delay the particles diffusion toward the vortex center.

CHAPTER 5. CONCLUSIONS

This dissertation investigated the mechanism of the evaporation behavior of droplet containing the insoluble particles. The most commonly used experimental approaches studying the evaporation process are reviewed, pendant droplet, aerodynamic and acoustic levitation and free falling method. The experiments involved either interaction between the droplets and the surrounding gas, leading to internal circulation within the droplet in the aerodynamic and acoustic levitation and free falling approaches or intrusive fiber in the pendant droplet approach. The droplet sizes are also limited to the millimeter size range. For the aim of investigation of transport processes in the isolated small droplets, an experimental setup based on electrodynamic balance (EDB) was built. The experimental systems consist of charged droplet generation apparatus through electrospray (ES), electrodynamic balance levitation system and droplet visualization system. The system allows observation of full evaporation process of 100 μm liquid suspension droplet.

Besides experimental design, a novel theoretical model has been developed to describe the morphological evolution process in the absence of internal convection. The analytical model accounts for the effect of the particles at the droplet surface on the diffusion of liquid vapor. The gradually increasing particle number at the droplet surface reduces the area for evaporation, leading to reduction of evaporation rate in the first evaporation stage, contrary to previous assumptions. The evaporation rate change depends on the Peclet number, initial concentration and particles contact angle at the liquid surface. It is found that

For large values of *Pe*, the particles concentration is high near the droplet surface, leading to the change of evaporation rate. For small values of *Pe*, the effect of particles on the evaporation rate of droplet in the first evaporation stage is small because particles are allowed sufficient time to redistribute within the droplet.

The duration of first evaporation stage is also controlled by the particle concentration. For small concentration coupled with small Peclet numbers, the time for particles to get saturated on the surface is shorter.

There exists a criteria for the evaporation of liquid suspension under different initial particles concentration and Peclet numbers, The evaporation can proceed only when the product of initial particles volume fraction and Pe is smaller than 1.95. Otherwise the model is not valid and the first stage terminates at the beginning of the first evaporation stage.

The model analysis also reveals that particle wettability is an important factor affecting the first evaporation stage. For hydrophilic particles, the contact angle of the particles at the droplet surface is small, leading to small change of evaporation in the first stage. For the hydrophobic particles that have large contact angles, the change of evaporation rate in the first evaporation stage is significant.

The evaporation model that accounts for the internal convection is also used to describe the evaporation process. In this model, the evaporation behavior during the first stage is controlled by the particle mobility, initial particle concentration, and droplet recession/evaporation rate. In the case of internal circulation, the evaporation rate in the first stage is expected to follow that of pure liquid, which

obeys the classic d^2-law. While the evaporation behavior in the first stage is controlled by the particles mobility, initial particles concentration and droplet recession.

For the evaporation with vigorous internal circulation, the particles distribution is controlled by the internal flow with the maximum particle concentration happening at the droplet surface and its center. The minimum particle concentration occurs at the vortex center.

For particles with high mobility, the particle distribution within the droplet tends to be smooth. The effect of convection flow on the particles distribution becomes stronger as particle mobility decreases. Once the particles mobility is decreased to a limit at which the surface particle density is only controlled by the internal flow and the evaporation process is independent of the particles mobility. For a given internal flow field and a specific particles mobility, the duration of the first stage and the final dry particle size are both controlled by the initial particles concentration. A smaller/larger initial particle concentration results in a longer/shorter first stage and smaller/larger dry particle.

Droplet evaporation rate is an important transport parameter in controlling the particles distribution and duration time of the first stage. With higher evaporation rate, the concentration evolution profile is much sharper near the droplet center and the droplet surface. Further enhancement of evaporation can delay the particles diffusion toward the vortex center.

APPENDIX A: ESTIMATION OF EVAPORATION RATE OF PURE LIQUID DROPLET IN STAGNATANT AIR

Consider the evaporation rate of a single fuel droplet in a non-convective atmosphere. The evaporation process is assumed to be quasi steady. So the temperature throughout the droplet can be taken as constant and equal to the surface temperature of the droplet. The conservation of energy and mass can be written as

$$4\pi r^2(\rho v)(\frac{dm_A}{dr}) = \frac{d}{dr}\left[4\pi r^2 \rho D(\frac{dm_A}{dr})\right] \tag{A.1}$$

$$4\pi r^2(\rho v)(\frac{dc_pT}{dr}) = \frac{d}{dr}\left[(\frac{\lambda 4\pi r^2}{c_p})(\frac{dc_pT}{dr})\right] \tag{A.2}$$

where λ is heat conductivity, c_p is specific heat capacity, v is the velocity of the gas, m is the mass fraction of species A, D is the mass diffusivity. Based on the gas kinetic theory, Dρ is constant for a given temperature and pressure ($D\rho=D_s\rho_s$), where the subscript s means the condition at the surface of the droplet.

The boundary condition for equation (A.1) is

$$\rho_l \dot{r} = \rho_s v_s = \rho_s m_{As} v_s - \rho D\left(\frac{dm_A}{dr}\right)_s \tag{A.3}$$

where ρ_l is liquid density, $\dot{r}$ is the liquid radius change rate. $\rho_s v_s$ is the bulk mass movement of gas and can be expressed as the amount of A that is being evaporated minus the amount of gaseous A that diffuses to or from the surface. From equation (A.3) gaseous velocity v_s can be expressed as

$$v_s = \frac{D_s(\frac{dm_A}{dr})_s}{(m_{As}-1)} \tag{A.4}$$

The boundary condition at $r=\infty$, $m_A = m_{A\infty}$

From continuity equation, we have

$$r^2\rho v = r_s^2 \rho_s v_s \tag{A.5}$$

Now we can solve equation (A.1) with Equations (A.3), (A.4) and (A.5)

$$\frac{r_s^2 v_s}{rD_s} = \ln\frac{m_{A\infty}-1}{m_{As}-1} \tag{A.6}$$

Evaluating equation (A.6) at $r = r_s$ results in

$$\frac{r_s v_s}{D_s} = \ln\frac{m_{A\infty}-1}{m_{As}-1} \tag{A.7}$$

Gas velocity at the surface can be related to r_s in the following way

$$v_s = -\frac{\rho_l}{\rho_s}\dot{r} \tag{A.8}$$

From equations (A.7) and (A.8), we have

$$\frac{dr_s^2}{dt} = -\frac{2D_s\rho_s}{\rho_l}\ln\frac{m_{A\infty}-1}{m_{As}-1} \tag{A.9}$$

Converting to droplet diameter, eq. (A.8) becomes

$$\frac{dd^2}{dt} = -\frac{8D_s\rho_s}{\rho_l}\ln\frac{m_{A\infty}-1}{m_{As}-1} = -\frac{8D_s\rho_s}{\rho_l}\ln(1+B_M) \tag{A.10}$$

where $B_M = (m_{As} - m_{A\infty})/(1-m_{As})$

Using the same way, we can solve equation (2) and get

$$\frac{dd^2}{dt} = -\frac{8\alpha_s\rho_s}{\rho_l}\ln(1+B_T) = -K \tag{A.11}$$

where $B_T = \frac{c_p(T_\infty - T_s)}{L_v}$, α_s is the thermal diffusivity of gas at the surface and L_v is the latent heat of vaporization at the surface temperature T_s. Compare equations (A.10) and (A.11)

$$\alpha_s \ln(1+B_T) = D_s \ln(1+B_M) \tag{A.12}$$

Since $\alpha = D$,

$$B_T = B_M \tag{A.13}$$

And

$$\frac{c_p(T_\infty - T_s)}{L_v} = \frac{m_{As} - m_{A\infty}}{1-m_{As}} \tag{A.14}$$

$$m_{As} = (\frac{P_A}{P})(\frac{MW_A}{MW}) = \frac{(\frac{P_A}{P})MW_A}{(\frac{P_A}{P})MW_A + (1-\frac{P_A}{P})MW_B} \tag{A.15}$$

MW_A, MW_B and MW are the molecular weight of A, B and the mixture. P_A and P are the vapor pressure of A and the total pressure.

With equation (A.14) and (A.15) we can get T_s and the value of B_M . Then the evaporation rate can be calculated. The difference between T_∞ and T_s is small, so to simplify the calculation T_s is assumed to be the same as the environmental temperature (T_∞) and the evaporation rate can be obtained from equation (A.11).

APPENDIX B: SOLUTION TO MATHIEU'S EQUATION

The Mathieu's equation is defined by:

$$\frac{d^2x}{d\xi^2} + (a - 2q\cos 2\xi)x = 0 \tag{B.1}$$

The solution to Mathieu's equation is written as:

$$x = \alpha' e^{\mu\xi} \sum_{n=-\infty}^{+\infty} C_{2n} e^{2in\xi} + \alpha'' e^{-\mu\xi} \sum_{n=-\infty}^{+\infty} C_{2n} e^{-2in\xi} \tag{B.2}$$

where α' , α'' are integration constants, whichdepends on the initial conditions, C_{2n} and μ depend on the values of a and q. Stable solutions are those where x remains finite as $\xi \to \infty$. Whether a solution is stable or not depends on the value of μ, as μ is only dependent on the values of a and q, the stability region of Mathieu's Equation on depends on these two values but not on the initial conditions.

There are four possibilities for μ:

(1) μ is real and non-zero. Instability arises from the $e^{\mu\xi}$ or $e^{-\mu\xi}$ factor.

(2) $\mu = i\beta$ is purely imaginary and beta is not an integer. These solutions are stable.

(3) μ is a complex number, the solutions are unstable.

(4) $\mu = im$ is purely imaginary and m is an integer. The solutions are periodic but unstable. $\mu = im$ corresponds to a curve in the (a,q) space when m is an integer, the curves forms the boundaries between the stable and unstable regions .

If we plug solution (A.2) in to Mathieu Equation (A.1), we get the recurrence

$$[a + (\mu + 2in)^2]C_{2n} - qC_{2n-2} - qC_{2n+2} = 0 \tag{B.3}$$

Let $\rho_n = (\mu + 2in)^2 + a$, equation (B.3) becomes:

$$\frac{-q}{\rho_n}C_{2n-2} + C_{2n} - \frac{q}{\rho_n}C_{2n+2} = 0 \tag{B.4}$$

To get a nontrivial solution, the determinant of the above simultaneous equations (shown below) must be zero:

$$\Delta(\mu) = \begin{vmatrix} \cdots & \cdots & \cdots & \cdots & \cdots & \cdots & \cdots & \cdots & \cdots \\ 0 & \frac{-q}{\rho_{-2}} & 1 & \frac{-q}{\rho_{-2}} & 0 & \cdots & \cdots & \cdots & \cdots \\ \cdots & 0 & \frac{+q}{\rho_{-1}} & 1 & \frac{-q}{\rho_{-1}} & 0 & \cdots & \cdots & \cdots \\ \cdots & \cdots & 0 & \frac{+q}{\rho_0} & 1 & \frac{-q}{\rho_0} & 0 & \cdots & \cdots \\ \cdots & \cdots & \cdots & 0 & \frac{-q}{\rho_1} & 1 & \frac{+q}{\rho_1} & 0 & \cdots \\ \cdots & \cdots & \cdots & \cdots & 0 & \frac{-q}{\rho_2} & 1 & \frac{-q}{\rho_2} & 0 \\ \cdots & \cdots & \cdots & \cdots & \cdots & \cdots & \cdots & \cdots & \cdots \end{vmatrix} \tag{B.5}$$

Set $\Delta(\mu) = 0$, which is equivalent to:

$$\sin^2[(\pi i\mu)/2] = \Delta(0)\sin^2[(\pi\sqrt{a})/2] \tag{B.6}$$

Let $\mu = \gamma + in, n \in N$, we have:

$$\sin[i\frac{\pi}{2}(\gamma + in)] = i\sinh(\frac{\pi}{2}\gamma)\cos(\frac{\pi}{2}n) - \cosh(\frac{\pi}{2}\gamma)\sin(\frac{\pi}{2}n) \tag{B.7}$$

There are two cases for *n*:

(1) *n=2m*, we have:

$$\cos(\frac{\pi}{2}n) = (-1)^m, \sin(\frac{\pi}{2}n) = 0 \tag{B.8}$$

Thus

$$\Delta(0)\sin^2(\frac{\pi}{2}\sqrt{a}) = -\sinh^2(\frac{\pi}{2}\gamma) \tag{B.9}$$

(2) *n=2m+1*, we have:

$$\Delta(0)\sin^2(\frac{\pi}{2}\sqrt{a}) = \cosh^2(\frac{\pi}{2}\gamma) \tag{B.10}$$

To get the expanded stability region of the problem discussed in Chapter 4.3.1, we set $\gamma = K$, and then equation (B.9) (B.10) forms the boundaries between stable and unstable regions. To get the stability region to the classical Mathieu's equation,

we set $\gamma = 0$ and equation (B.9) (B.10) forms the boundaries between stable and unstable regions. These regions can only be determined numerically as we are dealing with an infinitely large determinant. The stability region of the Mathieu's equation is shown in Figure 50.

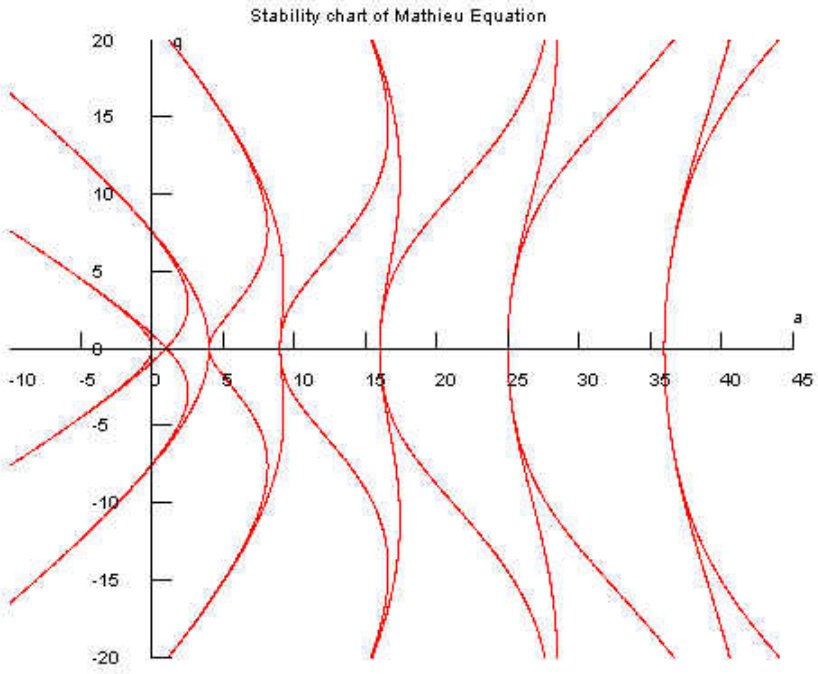

Figure 58 Stability of Mathieu's equation

As can be observed from the stability region of Mathieu's equation, $(a,q)=(n^2,0)$ is the separation point of adjacent stable regions, which can be verified by plugging in the value of $(a,q)=(n^2,0)$ to equation(B.5) and setting $\mu = in$.

For our problem discussed in Chapter 4.2,1 $a = -K^2 = -(\frac{3\pi\eta d}{mw})^2 < 0$, therefore only the left half plane of the stability region can be used.

Approximate analytical solutions can be obtained by truncating the infinite determinant (B.5) to 3×3, 5×5, 7×7 orders. The dashed lines in equation (B.5) show the 3×3 and 5×5 determinant. The first three of these determinants are shown below:

$$\Delta_1(0) = 1 + \frac{2q^2}{(4-a)a} \tag{B.11}$$

$$\Delta_2(0) = \frac{2q^2(1-\frac{q^2}{(4-a)(16-a)})}{(4-a)a} + (1-\frac{q^2}{(4-a)(16-a)})^2 \tag{B.12}$$

$$\Delta_3(0) = 2q^2(1-\frac{q^2}{(16-a)(35-a)})[\frac{(1-\frac{q^2}{(4-a)(16-a)}-\frac{q^2}{(16-a)(36-a)})}{(4-a)a}] \tag{B.13}$$
$$+(1-\frac{q^2}{(4-a)(16-a)}-\frac{q^2}{(16-a)(36-a)})^2$$

REFERENCES

Abuaf N, Staub FW. 1985. Drying of liquid-solid slurry droplets. General Electric, Corporate Research and Development

Acrivos A, Taylor TD. 1962. Heat and Mass Transfer from single spheres in stokes flows. *Physics of Fluids*. 5(4): 387-94

Adhikari B, Howes T, Bhandari BR, Troung, V. 2003. Surface stickiness of drops of carbohydrate and organic acid solutions during convective drying: experiments and modeling. *Drying Technology*. 21(5): 839-73.

Aggarwal SK, Sirignano WA, Tong AY. 1984. A comparison of vaporization models in spray calculations. *AIAA Journal*. 22(10): 1448-1457.

Alexis F, Pridgen E, Molnar LK, Farokhzad OC. 2008. Factors Affecting the clearance and Biodistribution of Polymeric Nanoparticles. *Molecular Pharmaceutics*. 5(4):505-15

Almeria B, Gomez A. 2014. Electrospray synthesis of monodisperse polymer particles in a broad (60 nm – 2 μm) diameter range: guiding principles and formulation recipes. *J. Colloid Interface Sci*.417: 121-30

Bazyn T, Krier H, Glumac N. 2007. Evidence for the transition from the diffusion-limit in aluminum particle combustion. *Proceedings of the Combustion Institute*. 31(2): 2021-28.

Beckstead MW. 2004 A Summary of Aluminum Combustion. BRIGHAM YOUNG UNIV PROVO UT.

Bogan MJ, Agnes GR. 2002. MALDI-TOF-MS analysis of droplets prepared in an electrodynamic balance:“Wall-less” sample preparation." *Analytical chemistry*. 74(3): 489-96.

Brannon-Peppas L. 1995. Recent Advances on the Use of Biodegradable Microparticles and Nanoparticles in Controlled Drug-Delivery. *International Journal of Pharmaceutics*. 116(1): 1-9.

Bulian CJ, Kerr TT, Puzynski JA. 2004. Ignition studies of aluminum and metal oxide nanopowders. *Proceedings of the 31st International Pyrotechnics Seminar*, *FT. Collins, CO*. 327-38

Castro D, Nieto C, Ribeiro AP, Hardacre C, Santos FV, Franca JM, Lourenco MJ, Goodrich P, Vieira SI, Murshed SM. 2013. Synthesis, Properties and Physical Applications of IoNanofluids. INTECH Open Access Publisher.

Chan HK, Chew NY. 2003. Novel alternative methods for the delivery of drugs for the treatment of asthma. *Adv. Drug Deliv. Rev*. 55: 793-805

Charlesworth DH, Marshall WR. 1960. Evaporation from drops containing dissolved solids. *AIChE Journal*. 6(1): 9-23

Chen RH, Phuoc TX, Martello D. 2010. Effects of nanoparticles on nanofluid droplet evaporation. *International Journal of Heat and Mass Transfer*. 53: 3677-82

Cheong HW, Jeffreys GV, Mumford, CJ. 1986. A receding interface model for the drying of slurry droplets. *AIChE Journal.* 32(8), 1334-46

Chow A, Tong H, Chattopadhyay, P, Shekunov BY. 2007. Particle engineering for pulmonary drug delivery. *Pharm. Res.* 24: 411-37

Dalmaz N, Ozbelge N, Eraslan HO, Uludag Y. 2007. Heat and Mass Transfer Mechanisms in Drying of a Suspension Droplet: A New Computational *Model. Drying Technology*. 25(2): 391-400

Das SK, Choi SU, Yu W, Pradeep T. 2007. Nanofluids. Science and Technology. John Wiley & Sons

Davis EJ, Buehler MF, Ward TL. 1990. The double-ring electrodynamic balance for microparticle characterization. *Review of Scientific Instruments*. 61(4): 1281-88.

Derkachov G, Kolwas K, Jakubczyk D, Zientara M, Kolwas M. 2008. Drying of a microdroplet of water suspension of nanoparticles: from surface aggregates to microcrystal. *The Journal of Physical Chemistry C. 112(43):* 16919-16923.

Ding Y, Alias H, Wen H, Williams RA. 2006). Heat transfer of aqueous suspensions of carbon nanotubes. *Int. J. Heat Mass Transfer*. 49(1): 240-50

Duff D., Achtzehn T, Muller R, Huber BA, Leisner T. 2003. Coulomb fission: Rayleigh jets from levitated microdroplets. *Nature*. 421(6919): 128-128

Eastman JA, Choi JA, Li S, Yu W, Thompson LJ. 2001. Anomalously increased effective thermal conductivities of ethylene glycol based nanofluids containing copper nanoparticles. *Applied Physics Letters*, 78(6): 718-20

Elperin T, Krasovitov B. 1995. Evaporation of liquid droplets containing small solid particles. *International Journal of Heat and Mass Transfer. 38(12): 2259-67*

Faulkner DJ. Rector DR, Davidson JJ, Shekarriz R. 2004. Enhanced heat transfer through the use of nanofluids in forced convection. *In ASME 2004 International Mechanical Engineering Congress and Exposition*. American Society of Mechanical Engineers. 219-224.

Fenn JB, Mann M, Meng C, Wong S, Whitehouse C. 1989. Electrospray Ionization for mass spectrometry of large biomolecules. . *Science*. 246(4926): 64-71

Fu N, Woo M, Chen X. 2012. Single droplet *drying* technique to study drying kinetics measurement and particle functionality: a review. *Drying Technology*. 30(15): 1771-85

Fuchs NA. 1959. Evaporation and Droplet Growth in Gaseous Media. The Pergamon Press, Oxford.

Gan Y, Qiao L. 2011. Combustion characteristics of fuel droplets with addition of nano micro-sized aluminum particles. *Combustion and Flame*. 158(2): 354-68

Gan Y, Qiao L. 2011. Evaporation characteristics of fuel droplets with the addition of nanoparticles under natural and forced convections. *International Journal of Heat and Mass Transfer*. 54(23): 4913-22

Ganan-Calvo AM. 1997. Cone- Jet analytical extension of Taylor's electrostatic solution and the asymptotic universal scaling laws in electrospray. *Physical review letters*. 79(2): 217

Garner FH, Keey RB. 1958. Mass transfer from single solid spheres - I: Transfer at low Reynolds numbers*. Chemical Engineering Science*. 9(2): 119-29

Garner FH, Lane JJ. 1959. Mass transfer to drops of liquid suspended in a gas stream. Trans. Inst. Chem. Eng., 37:167-172

Hadamard J.S.C.R. 1911. Mouvement permanent lent d'une sphere liquid et visqueuse dans un liquid visqueux. CR Acad. Sci., 152(25): 1735-1738

Handscomb CS, Kraft M, Bayly AE. 2009. A new model for the drying of droplets containing suspended solids. *Chemical Engineering Science. 64(4): 628-637.*

Hartman RP, Brunner DJ, Camelot DM, Marijnissen JC, Scarlett B. 2000. Jet break-up in electrohydrodynamic atomization in the cone-jet mode*. Journal of aerosol science*. 31(1): 65-95

Hill M.J.M.1894. On a spherical vortex. Proceedings of the Royal Society of London. 55(331-335):219-224

Holland PM, Eaton BE, Hanley HJ. 1983. A correlation of the viscosity and thermal conductivity data of gaseous and liquid ethylene. *Journal of physical and chemical reference data.* 12(4): 917-932.

House W. 2000. National nano technology initiative: Leading to the next industrial revolution. The White House, Office of the Press Secretary, Washington, DC.

Hsieh DS, Rhine WD, Lauger R. 1983. Zero-order controlled release polymer matrices for micromolecules and macromolecules. *Journal of Pharmaceutical Sciences.* 72(1): 17-22

Huang Y, Risha GA, Yang V, Yetter RA. 2007. Combustion of bimodal nano/micron-sized aluminum particle dust in air. *Proceedings of the Combustion Institute*. 31(2): 2001-2009

Huang Y. Risha GA, Yang V, Yetter RA. 2009. Effect of particle size on combustion of aluminum particle dust in air. *Combustion and Flame*. 156(1): 5-13

Imanura T, Imanura C, Iwamoto Y, Sandell LJ. Transcriptional Co-activators CREB-binding protein/p300 increase chondrocyte Cd-rap gene expression by multiple mechanisms including sequestration of the repressor CCAAT/ehancer-binding protein. *Journal of Biological Chemistry*. 280(17): 16625-16634

Johnstone HF, Kleinschmidt RV. 1938. Absorption of gases in wet cyclone scrubbers. [Using water treated with soda ash]. *Trans. AIChE*. 34

Kandlikar SC, Hayner CN. 2009. Liquid Cooled Cold Plates for Industrial High-Power Electronic Devices-Thermal Design and Manufacturing Considerations. *Heat Transfer Engineering.* 30(12): 918-30

Kao M, Ting CC, Lin EB, Tsung TT. 2008. Aqueous aluminum nanofluid combustion in diesel fuel. *Journal of testing and evaluation*. 36(2): 503

Kinzer GD, Gunn R. 1951. The evaporation, temperature and thermal relaxation-time of freely falling waterdrops. *Journal of Meteorology*. 8(2): 71-83

Krong R, Bruijsten J. 1951. On the theory of the heat and mass transfer from a sphere in a flowing medium at low values of Reynolds' number. *Applied Scientific Research.* 2(1): 439-46

Kumar M. Nano and microparticles as controlled drug delivery devices. 2000. *J. Pham. Pharm. Sci.* 3(2): 234-258

Lar-Urbaneja P, Sirignano WA. 1981. Theory of transient multicomponent droplet vaporization in a convective field. *Symposium (International) on Combustion.* 18(1): 1365-1374.

Lee A, Law CK. 1991. Gasification and shell characteristics in slurry droplet burning. *Combustion and Flame.* 85(1): 77-93

Leong KH. 1987. Morphological control of particles generated from the evaporation of solution droplets: theoretical considerations. *Journal of Aerosol Science*. 18(5): 511-24.

Levi-Hevroni D, Levy A, Borde I. 1995. Mathematical modeling of drying of liquid or solid slurries in steady state one-dimensional flow. *Drying Technology. 13(5-7): 1187-1201*

Levich VG, Technica S. 1962. Physicochemical hydrodynamics. 689. Englewood Cliffs, NJ: Prentice-hall

Macek A. 1973. Combustion of Boron Particles: Experiment and Theory. In Symposium (International) on Combustion. 14(1): 1401-1411. Elsevier

Mainardes RM, Silva, LP. 2004. Drug Delivery Systems: Past, Present, and Future. Current drug targets. 5(5): 449-55

Makino A, Law, C. 1988. On the controlling parameter in the gasification behavior of multicomponent droplets. Combustion and Flame. 73(3): 331-336).

Maloney DC, Gary AL. 1995. Rapid decomposition of summer-input leaves in a northern Michigan stream. *American Midland Naturalist. 184-195.*

Maxwell JC. 1881. A Treatise on Electricity and Magnetism. Clarendon Press

Mezhericher M, Levy A, Borde I. 2007. Theoretical Drying Model of Single Droplets Containing Insoluble or Dissolved Solids. *Drying Technology. 25(6): 1025-32.*

Mezhericher,M. Levy A, Borde I. 2010. Thoretical Models of Single Droplet Drying Kinetics: A Review. *Drying Technology*. 28(2): 278-93.

Mezhericher M, Levy A, Borde I. 2010. Theoretical Models of Single Droplet Drying Kinetics: A Review. *Drying Technology. 28(2): 278-93.*

Mezhericher M, Levy A, Borde I. 2011. Modelling the morphological evolution of nanosuspension droplet in constant-rate drying stage. *Chemical Engineering Science. 66(5): 884-96.*

Mezhericher M, Naumann M, Peglow M, Levy A, Tsotsas E, Borde I. 2012. Continuous species transport and population balance models for first drying stage of nanosuspension droplets. *Chemical Engineering Journal. 210: 120-35*

Minoshima H, Matsushima K, Liang H, Shinohara K. 2001. Basic Model of Spray Drying Granulation. *Journal of chemical engineering of Japan*. 34(4): 472-78.

Miura K, Miura T, Ohtani S. 1977. Heat and mass transfer to and from droplets. In AIChE Symposium Series. 73(163): 95-102.

Neeves KB, Sawyer AJ, Foley CP, Saltzman WM, Olbricht WL. 2007. Dilation and Degradation of the Brain Extracellular Matrix Enhances Penetration of Infused Polymer Nanoparticles. Brain Research. 1180. 121-32.

Nesic S, Vodnik J. 1991. Kinetics of droplet evaporation. *Chemical Engineering Science*. 46(2): 527-37.

Park J, Fahmy TM. 2010. Biodegradable Nanoparticles for Drug Delivery. Handbook of Nanophysics: Nanomedicine and Nanorobotics. Taylor and Francis Group, New York, 1-14.

Paul W, Steinwedel H. 1953. *German Patent No. 944 900*; *US. Patent 2939958*.

Prakash S, Sirignano WA. 1980. Theory of convective droplet vaporization with unsteady heat transfer in the circulating liquid phase. International Journal of Heat and Mass Transfer. 23(3): 253-268

Ranz WE, Marshall WR. 1952. Evaporation from drops. Chemical Engineering Progress. 48(3): 141-46.

Ray AK, Johnson RD, Souyri A. Dynamic behavior of single glycerol droplets in humid air streams. *Langmuir* . 5(1): 133-40

Rayleigh L. XX. 1882. On the equilibrium of liquid conducting masses charged with electricity. *The London, Edinburgh, and Dublin Philosophical Magazine and Journal of Science. 14(87): 184-86.*

Renksizbulut M, Haywood RJ. 1988. Transient droplet evaporation with variable properties and internal circulation at intermediated Reynolds numbers. International Journal of Multiphase Flow. 14(2): 189-202.

Saha A, Basu S, Kumar R. 2012, a. Particle image velocimetry and infrared thermography in a levitated droplet with nanosilica suspensions. *Experiments in fluids*. 52(3): 795-807.

Saha A, Basu S, Kumar R. 2012, b. Effects of acoustic-streaming-induced flow in evaporating nanofluid droplets. Journal of Fluid Mechanics. *Journal of Fluid Mechanics*. 692: 207-219.

Saltzman WM. 2001. Drug Delivery: engineering principles for drug therapy. Oxford University Press, USA.

Schafer J. Mondia JP, Lu Z, Susha AS, Rogach AL, Wang L. 2008. Quantum Dot Microdrop Laser. *Nano letters*. 8(6): 1709-12

Schiffter H, Geoffrey L.2007. Single-droplet evaporation kinetics and particle formation in an acoustic levitator, Part 1: Evaporaiton of water microdroplets assessed using boundary-layer and acoustic levitation theories. *Journal of Pharmaceutical Sciences*. 96(9): 2274-83.

Selvan VA, Anand RB, Udayakumar M. 2009. Effects of cerium oxide nanoparticle addition in diesel and diesel-biodiesel-ethanol blends on the performance and emission characteristics of a CI engine. *J. Eng. Appl. Sci*. 4(7): 1819-6608

Sen D, Mazumder S, Melo JS, Khan A, Bhattyacharya S, D'Souza SF. 2009. Evaporation driven self-assembly of a colloidal dispersion during spray drying: volume fraction dependent morphological transition. *Langmuir. 25(12): 6690-95.*

Seydel P, Blömer J, Bertling J. 2006. Modeling Particle Formation at Spray Drying Using Population Balances. *Drying Technology. 24(2):* 137-46

Shaw RA, Lamb D, Moyle AM. 2000. An Electrodynamic levitation system for studying individual cloud particles under upper-tropospheric Conditions. *Journal of Atmospheric and Oceanic Technology*. 17(0: 940-48.

Sirignano WA. 1978. Theory of multicomponent fuel droplet vaporization. *Archives of Thermodynamics and Combustion.* 9(2): 231-47.

Soppimath KS, Aminabhavi TM, Kulkarni AR, Rudzinski WE. 2001. Biodegradable polymeric nanoparticles as drug delivery devices. *Journal of controlled release*. 70(1): 1-20.

Straubel H. 1959. Rate of evaporation and changes in the electrical charge of drops. *Dechema Monograph*. 32: 153-59.

Taylor G. 1964. Disintegration of water drops in an electric field. Proceedings of the Royal Society of London A: Mathematical, *Physical and Engineering Sciences*. 280(1382): 383-97.

Tong AY, Sirignano WA. Multicomponent droplet vaporization in a high temperature gas. *Combustion and Flame*. 66(3): 221-35

Vehring R, Foss WR, Lechuga-Ballesteros D. 2007. Particle formation in spray drying. *Aerosol Science*. 38(7): 728-46.

Vehring R. 2008. Pharmaceutical Particle Engineering via Spray Drying. *Pharmaceutical Research.* 25(5): 999-1022

Wallack DA, El-Sayed, TM, King CJ. 1990. Changes in particle morphology during drying of drops of carbohydrate solutions and food liquids. 2: Effects on drying rate. *Industry and Engineering Chemistry Research*. 29(12): 2354-57

Weiss-Wrana K. 1983. Optical properties of interplanetary dust-Comparison with light scattering by larger meteoritic and terrestrial grains. *Astronomy and Astrophysics* . 126: 240-50.

Wen D, Ding Y. 2004. Experimental investigation into convective heat transfer of nanofluids at the entrance region under laminar flow conditions. *International journal of heat and mass transfer*. 47(24): 5185-88.

Wilhelm O. 2004. *Electrohydrodynamic spraying-Transport, mass and heat transfer of charged droplets and their application to the deposition of thin functional films*. (Doctoral dissertation, Diss., Eidgenössische Technische Hochschule ETH Zürich, Nr. 15406)

Wong SC, Lin AC. 1992. Internal temperature distributions of droplets vaporizing in high-temperature convective flows. Journal of Fluid Mechanics. 237:671-687

Wuerker RF, Shelton H, Langmuir RV. 1959. Electrodynamic containment of charged particles. *Journal of Applied Physics*. 30(3): 342-49.

Xuan Y, Li Q. 2000. Heat transfer enhancement of nanofluids. *International Journal of heat and fluid flow.* 21(1): 58-64.

Yang W, Lojewski B, Wei Y., Deng W. 2012. Interactions and deposition patterns of multiplexed electrosprays. *Journal of Aerosol Science*. 46: 20-33.

Yarin AL, Brenn G, Kastner O, Rensink D, Tropea C. 1999. Evaporation of acoustically levitated droplets. *Journal of Fluid Mechanics.* 399: 151-204.

Yarin AL, Brenn G, Kastner O, Tropea C. 2002. Drying of acoustically levitated droplets of liquid-solid suspensions: Evaporation and crust formation. *Physics of Fluids.* 14(7): 2289-98

Yetter RA, Dryer FL, Ross HD. 2001. Microgravity Combustion: Fire in Free Fall. 419-78.

Zeng C, Brau F, Davidovitch B, Dinsmore AD. 2012. Capillary interactions among spherical particles at curved liquid interfaces. *Soft Matter. 8(33): 8582-94*

Glassman I. Yetter RA, Glumac NG. 2008. Combustion. Academic press.

Zhang SH, Davis EJ. 1987. Mass Transfer from a single micro-droplet to a gas flowing at low Reynolds number. *Chemical Engineering Communications*. 50(1-6): 51-67

Zheng F, Qu X, Davis EJ. 2001. An octopole electrodynamic balance for three-dimensional microparticle control. *Review of Scientific Instruments*. 72(8): 3380-85